Characterization of Modified Mesophase Pitch-Based Carbon Fibers

---

A
Dissertation
Presented to
the faculty of the School of Engineering and Applied Science
University of Virginia

---

in partial fulfillment of the requirements for the degree

Doctor of Philosophy

by

Alexander Scherschel

May 2025

APPROVAL SHEET

This
Dissertation
is submitted in partial fulfillment of the requirements for the degree of
Doctor of Philosophy

Author: Alexander J Scherschel

This dissertation has been read and approved by the examining committee:

Advisor: Xiaodong Li

Committee Chair: Baoxing Xu

Committee Member: David Green

Committee Member: Liheng Cai

Committee Member: Frederic Vautard

Accepted for the School of Engineering and Applied Science:

Jennifer L. West, School of Engineering and Applied Science
May 2025

Abstract

Carbon fiber (CF) is the premier building material in multiple, important industries and continues to grow in both its usage and demand. However, the cost of the premier CF, produced from polyacrylonitrile (PAN), has limited the CF market. Therefore, alternative CF precursor research remains an important topic with the goal of driving down cost while limiting environmental impacts.

The aim of this dissertation is to explore the capabilities of one possible alternative precursor material: mesophase pitch. The benefit of mesophase pitch lies in the production of the feedstock and precursor fibers. Since mesophase pitch is a byproduct produced from petroleum distillation and coal cracking, large cost saving opportunities exist. Additionally, it can be melt-spun, a more cost-effective extrusion method which removes the need for any environmentally harmful solvents required with PAN wet spinning. While the achievable strengths of mesophase pitch-based CF (MPCF) cannot compete with PAN-CF, MPCF has found uses in industries which are more concerned with stiffness-to-weight ratio, electrical and thermal conductivity, and low thermal expansion. For MPCF to enter additional markets, such as general car manufacturing, the cost must be further reduced while maintaining quality properties. This is possible through a better understanding of CF structure-property-relationship.

Prior to extrusion, mesophase pitch can be modified through the introduction of waste polymers. The addition of such polymers provides two benefits: 1) cost reductions and 2) environmental sustainability. Such hybrid fibers have been previously produced, but these fibers could not be converted into CF leaving the need for such exploration. By blending with linear low-density polyethylene and polyethylene terephthalate, these experiments revealed that such

fibers could be produced successfully, but special considerations of the polymer and its effect on the fiber's microstructure must be taken into account.

The focus on the fiber's microstructure provided the basis for the remainder of this dissertation. The production of MPCF involves extrusion, oxidation, and carbonization, with all three steps playing a significant role in the CF development. Changes in the extrusion procedure create different texture shapes, each with unique properties. However, the microstructure of these different fibers has yet to be explored in detail and represents an opportunity to gain additional understanding. The fibers must be thermally stabilized in oxygen, such that the fibers can survive the final heat treatment process. A successful oxidation involves an even diffusion of oxygen throughout the fiber. If heated to quickly in an effort to reduce cost, a core-shell structure is developed resulting in depreciated tensile properties. However, if held at temperature for too long to ensure complete diffusion, over-oxidation as a result of the removal of carbon atoms sets in. Finding the balance of temperature and time for oxidation is vital and must be explored in more depth. Finally, carbonization, or high temperature heat treatment, is the process of removing noncarbon atoms resulting in carbon crystallite growth which are responsible for the desired CF properties. Given the complicated reactions, relevant rates for industrial production (> 50 °C/min) were examined, and a rate of 23.3 °C/min was found to produce the strongest fiber.

The work presented in this dissertation contributes to the understanding of the affects each production step has on the structure and properties of MPCF. Each alteration offers an opportunity to provide cost-reductions, decrease environmental impact, and control the CF

macro-properties through the microstructure. Additionally, recommendations for future work are offered in the final chapter of this dissertation.

Acknowledgements

This work reflects my family's continued support and effort. Most notably, I would not have reached this point in my career without the love and support of my wife, Jennifer Scherschel. Without her, I would not have considered attending graduate school and certainly would not have achieved the success I have found. I will forever be grateful for her comfort, steadfast belief, and the patience she has shown me through my many late nights in the lab and the countless hours spent locked in the home office writing.

To the rest of my family, you have all had a profound impact on my life over the past five years. My mother has made sure I continue to live life outside of work and maintain some semblance of balance, while my father has provided a guiding hand whenever I have needed it. To my in-laws, we will forever be grateful for the kindness and support you showed us while we lived in Charlottesville. Without you, life would have looked very different.

Thank you, Dr. Xiaodong "Chris" Li, for your unwavering support and leadership throughout my graduate career. From our first meetings over Zoom during the pandemic, you have always maintained a positive, future-focused outlook and optimism, which has instilled in me a sense of confidence that made this journey possible. I would also like to thank Dr. Tim Harrell. You were the first member of the lab I met, worked with, and published with. Your mentorship in all aspects, both professional and personal, has made me a better scientist and a better person.

To my colleagues, while this work reflects individual accomplishments, let it be known that none of this would have been possible without your efforts. To Andre Sushchenko and Dr. Cole Love-Baker, our late-night tensile testing sessions and discussions, bouncing between studies and imaging, will forever be some of my favorite memories. To the rest of my lab mates—Dr. Kenneth Brown, Eli Knight, Ryan Cordier, Tyler Daspit, Hans Hudyncia, Luke Skrzypczak, and ZhiJing Xue—I have truly enjoyed the opportunity to work and publish with each of you. Thank you.

Finally, this work would not have been possible without funding from the U.S. Department of Energy's Hydrogen and Fuel Cell Technologies Office (DE-EE0009239) and Vehicle Technologies Office (DE-EE0008195 and DE-EE0010602), as well as additional support from staff and collaborators. The University of Virginia Nanoscale Materials Characterization Facility and their research staff provided invaluable assistance and access to a number of essential pieces of equipment. Thank you to Joseph Thompson and Richard White for your help with the Raman spectrometer, SEM, and countless sample preparation and polishing tools. A special thank you to Dr. Helge Heinrich for your efforts with TEM sample prep and analysis using the Themis. Additionally, I would like to thank the ORNL staff for their efforts surrounding Chapter 4 of this dissertation. Specifically, thank you, Dr. Frederic Vautard, for your coordination within ORNL that allowed the Raman mapping and XRD to be completed. I would also like to thank you for your reviews of my manuscript as we went back and forth many times, with each round resulting in clear improvements to both the science and the writing.

All of this support from UVA, NMCF, and ORNL mean more to me now than ever given the current state of research funding and the view of science in America as a whole.

Table of Contents

List of Figures

List of Tables

Common Abbreviations and Acronyms

CF	Carbon fiber
COV	Coefficient of variance
CTP	Coal tar pitch
DSC	Differential scanning calorimetry
DTG	Derivative thermogravimetry
EDS	Energy dispersive x-ray spectroscopy
EELS	Electron energy loss spectroscopy
FFT	Fast Fourier transform
FTIR	Fourier-transform infrared spectroscopy
FWHM	Full-width half-max
HAADF	High angle annular dark-field
LLDPE	Linear low-density polyethylene
MPCF	Mesophase pitch-based carbon fiber
PAN	Polyacrylonitrile
PET	Polyethylene terephthalate
PS	Polystyrene
SAED	Selected area electron diffraction
SAXS	Small-angle x-ray scattering
SEM	Scanning electron microscopy
TEM	Transmission electron microscopy
TGA	Thermo-gravimetric analysis
TK	Tuinstra-Koenig
WAXD	Wide-angle x-ray diffraction
XRD	X-ray diffraction

Chapter 1: Introduction

1. Carbon Fiber Production and Market

Carbon fiber (CF) is a critical engineering material due to its high strength-to-weight ratio, stiffness-to-weight ratio, electrical conductivity, and thermal conductivity. The invention of CF is credited to Thomas Edison from his work in 1879 on incandescent light bulbs, which he later patented in 1880 [1]. These carbon filaments were produced from cotton and bamboo (cellulose), and while Edison replaced the carbon filaments for tungsten soon after, CF found usage in other industries [2]. Later work in the 1960s by the Union Carbide Corporation resulted in the fabrication of CF from polyacrylonitrile (PAN) and rayon, which were used as reinforcements due to their structural benefits [3]. PAN-based CF was found to possess the highest tensile strength, making it the ideal candidate for CF production. To this day, PAN-CF constitutes around 92% of the global CF market, a $6 billion industry, with Toray being the leading manufacturer of PAN-CF [4,5].

Depending on the heat treatment and spinning processes used, various types of CF can be produced, including: standard modulus (200-280 GPa), intermediate modulus (280-350 GPa), and high modulus (>350 GPa) [6]. Given the range of achievable mechanical properties, PAN-CF has found use in a number of industries including hydrogen storage tanks [7], lightweight vehicles [8], electric vehicles (EVs) [9], batteries and supercapacitors [10,11], aerospace [12], sporting goods [13], and others where the material properties importance outweighs the cost. However, there are larger markets that would adopt CF but cannot afford the cost of PAN-CF. Since the production of the PAN precursor accounts for at least 50% of the total CF expense, many studies have focused on finding alternative precursor materials [14].

Pitch is the name given to the viscoelastic, carbonaceous byproduct created during the distillation of crude oil, coal, and organic materials [15]. As a byproduct material, pitch is significantly less expensive than PAN and is mostly composed of aromatic hydrocarbons, making it an ideal candidate for CF production [16]. However, mesophase pitch-based CF (MPCF) initially struggled to compete with PAN-CF in terms of tensile strength, with the strongest MPCF reaching values of 3.7 GPa [17], compared to 8 GPa for the Toray T1200 PAN-CF [18]. Additionally, while the cost to produce mesophase pitch-based precursor fibers is significantly lower than that of PAN-derived fibers, the stabilization times and temperatures negated any initial cost savings, leading most researchers to move away from mesophase pitch in the 1990s [19]. However, some researchers continued working with mesophase pitch, and recent advancements, coupled with new industry needs, have led to a revival of MPCF.

Depending on the heat treatment, MPCF can achieve a tensile modulus as high as 1000 GPa [20]. When combined with a tensile strength of 3-3.5 GPa, superior thermal and electrical conductivity, and a low thermal coefficient of expansion, MPCF has gained interest in space applications [21–23] and as dampeners [24] where stiffness and transport properties are more important than strength. Producing such fibers remains challenging, and doing so in a cost-effective manner further complicates the process.

This dissertation reviews the current state of MPCF and its production techniques, exploring alternative methods at each processing step. The production of CF is broken down into four stages, as outlined in **Figure 1**, to better understand the role each stage plays in the final fiber's characteristics. Throughout this work, new insights into the role of each stage will be developed, ultimately advancing the understanding of the material and the CF production process as a whole.

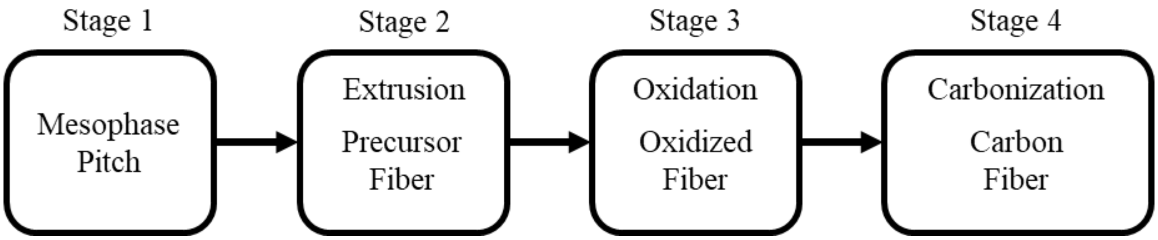

Figure 1. Breakdown of the four main CF production stages. The name of the stage is given as well as the commonly used name for the fiber/filament produced at each step which will be used throughout this work. Modified from [25]

2. Precursor

Pitch can be produced and modified in several ways, all of which affect its rheological properties and the properties of the resulting CF. Therefore, a further breakdown of the different pitch variations as a result of mesophase production, feedstock choice, and alterations made through the addition of catalysts and polymers will be provided.

2.1. Isotropic and Mesophase Pitch Production

When first produced, byproduct pitch is an isotropic material composed of aromatic hydrocarbons, sulfur, oxygen, and other non-organic compounds. Simple distillation steps are used to remove larger impurities. The byproduct pitch is then heated for a week at 70 °C, allowing it to become homogeneous [26]. The now-refined byproduct pitch is known as intermediate or isotropic pitch. Isotropic pitch can be spun into fiber and used to produce CF; however, it must be thermally or chemically treated to create spinnable isotropic pitch, defined as having a softening point below 300 °C [27]. The production of mesophase pitch requires additional costly steps, and for this reason, many studies on isotropic pitch-based CF have been conducted.

Due to its ease of production, spinning, and subsequent low cost, many researchers have focused on producing isotropic pitch CF capable of reaching tensile strengths of 1.7 GPa while keeping the cost below 10 USD/kg—the threshold set by the U.S. Department of Energy for low-cost automobile commercial use [28]. Kim et al. were able to produce an isotropic pitch-based CF with a tensile strength of 2.05 GPa through a combination of naphtha-cracked oil and coal tar pitch [29]. However, this process involved bromination and dehydrobromination, leading to a significant increase in cost and environmental impact, thereby negating the benefits of isotropic pitch-based fibers. Outside of this work, most isotropic pitch CF possess a tensile strength of around 1 GPa and a modulus ranging from 40–80 GPa [30–33]. Therefore, isotropic pitch CF is mainly used for high-temperature insulation and other applications that take advantage of their thermal and electrical properties, but do not require high mechanical properties [34]. To reach the desired properties, conversion from isotropic to mesophase pitch is required.

The final step in converting isotropic pitch into mesophase pitch involves thermal polycondensation or catalytic polymerization when using a synthetic feedstock [35]. Researchers as early as 1928 showed that carbonized cokes exhibited optical anisotropy when viewed under polarized light [36]. It was not until 1965 that Brooks and Taylor conducted experiments on a wide range of carbonaceous materials, including some petroleum-derived samples, and described the production of anisotropic carbons in an isotropic matrix [37]. They showed that with increasing heat treatment temperatures, small fractions of anisotropic carbon formed into spheres, which were reactive under polarized light. These spheres are now known as Brooks-Taylor spheres. As the temperature increased, the percentage of material converting from isotropic to anisotropic also increased, and the spheres began to coalesce, eventually spreading and losing their spherical shape developing into the 'mosaic' phase, as shown in **Figure 2**. Eventually, the anisotropic material solidified and formed semi-coke. This is why the anisotropic material was named mesophase by

Gray, as “*mesos*” translates to “intermediate,” and the mosaic phase represents the step between isotropic pitch and semi-coke when fully heat-treated [38].

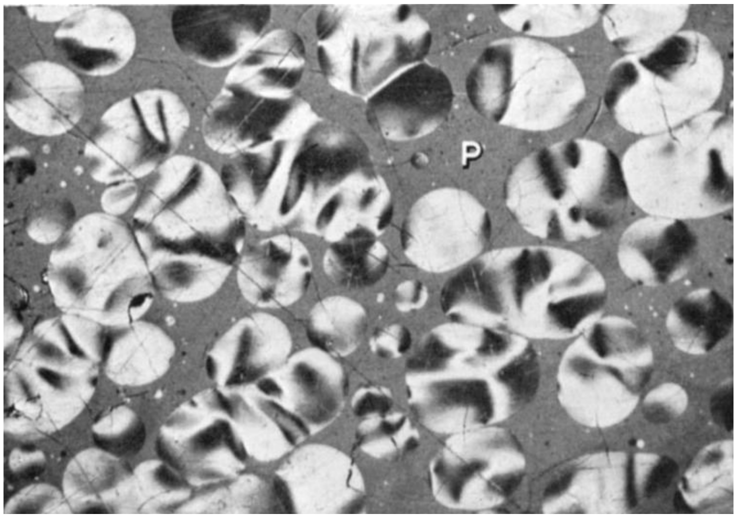

Figure 2. A polarized light image of pitch at an intermediate step in the mesophase production process. The “P” in the nonreactive material shows the isotropic pitch while the spheres are the mesophase, or liquid crystalline, material [37]

It is important to note that the term "mesophase pitch" is commonly used as a catch-all in the literature and refers to pitch blends of anisotropic and isotropic pitch. The production of mesophase pitch remains costly and difficult, requiring additional steps, such as nitrogen-bubbling treatment, to achieve an 80% mesophase volume fraction [39]. To obtain 100% mesophase pitch, various separation methods such as solvent extraction, supercritical solvent extraction, or high-temperature centrifugation must be employed [16]. However, these methods are expensive, so most researchers focus on a mixture of the two phases, although this can lead to phase separation during the spinning process. Yuan et al. showed that a mixture with less than a 75/25 anisotropic/isotropic ratio would result in a less spinnable material, leading to decreased spinnability [40]. Pitch with at least 75 vol.% anisotropic material is as spinnable as isotropic pitch, with the isotropic phases acting as plasticizers that allow for consistent extrusion. Coupled with the fact that due to its higher crystallinity and alignment, CF produced with a higher anisotropic content will have a higher tensile strength and modulus, a pitch of at least 75 vol% anisotropic is recommended for CF production.

2.2. Feedstock Impact

The most common feedstocks for byproduct pitch include coal, petroleum, and organic matter, while synthetic pitch has been produced from naphthalene [41]. Synthetic pitch has been extensively explored by Mitsubishi Gas Company, and their results have shown some promise [42]. However, any cost benefits are negated due to the higher price of the precursor material compared to using a byproduct. Additionally, pitch produced from organic matter, known as rosin, has not shown promise as a CF precursor material and has only been used as a catalyst to stimulate mesophase growth in other pitch materials [43]. The two remaining pitch feedstock materials to be discussed are petroleum and coal. CF produced from both feedstocks has been shown to be of high quality and possess unique characteristics.

Coal tar pitch (CTP), as the name implies, is produced from the distillation of coal and is the cheaper of the two main feedstock options. Compared to petroleum pitch, CTP possesses a higher carbon yield due to the higher percentage of aromatic compounds present in the material (**Figure 3**a). However, it also contains a higher amount of impurities that must be filtered out, requiring a more complicated refinement process [44]. The higher percentage of aromatic compounds also leads to the production of more oriented fibers with a higher carbon-to-hydrogen (C/H) ratio. A higher degree of orientation will lead to stiffer CF but also makes spinning precursor fibers more difficult. With a higher C/H ratio and greater orientation, the softening point of the material is higher, and CTP exhibits higher viscosity, meaning that melt-extrusion must be performed at a higher temperature and pressure [27]. These factors ultimately result in a more complicated spinning procedure, leading to larger-diameter fibers on average.

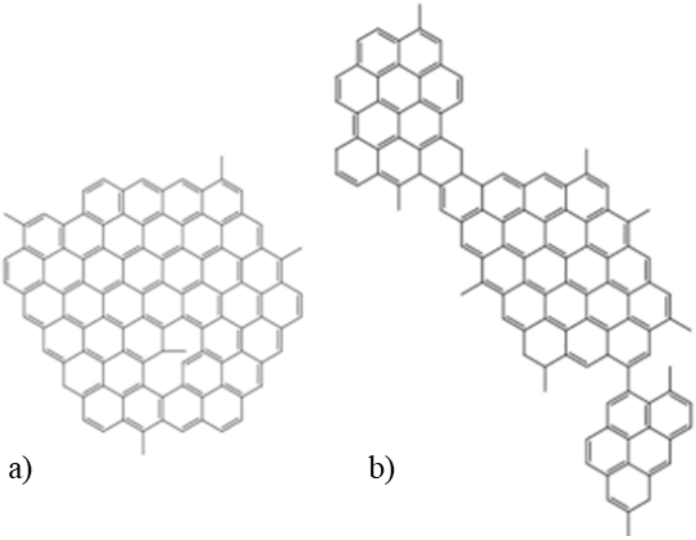

Figure 3. Schematic of the molecular representation of the a) CTP chemical structure and b) the petroleum-based mesophase pitch structure. Modified from [45]

While slightly more expensive than CTP, petroleum-derived mesophase pitch possesses a number of properties that make it a more ideal candidate for CF production. Most notably, the precursor fibers can be drawn to a finer diameter at lower temperatures and pressures, making the spinning process simpler and more repeatable [46]. Additionally, petroleum-derived pitch has a lower percentage of nitrogen and sulfur and a higher percentage of aliphatic compounds (**Figure 3**b). T This results in a decreased C/H ratio, which leads to a lower char yield but better spinning and stabilization characteristics. Lastly, the initial structure lends itself to better CF formation, as the liquid crystals can reorganize more efficiently, leading to fewer voids and a stronger CF.

2.3. Mesophase Pitch Conversion via Blending

The lower tensile strength of MPCF compared to PAN-CF is due to the large grain size formed by the planar aromatic molecules and the resultant liquid crystalline structure of the mesophase pitch [37,47–49]. Various strategies have been explored to increase the tensile strength of MPCF. These include disrupting the liquid crystalline structure through manipulation of the material flow [50,51], doping with heteroatoms and graphitic structure enhancers [52,53], and adding carbon-based materials such as carbon black, graphene, and graphene oxide [54–58]. Each of these methods has shown varying degrees of success, mostly focusing on alterations to the graphitic structure of the CF. By disrupting crystalline growth, one can hope to increase the tensile strength of the fiber, albeit at the expense of the tensile modulus. Based on these conclusions, another approach was proposed.

Researchers set out to determine the effects of mixing polymer additives with mesophase pitch during the refining of the feedstock and CF production. A number of polymers, including polystyrene (PS), polyvinyl chloride (PVC), and polyphenylene oxide (PPO), have been explored [59–64]. In some experiments, the polymer was added to the isotropic pitch before mesophase production, and these studies showed several promising results. Most notably, mesophase production was faster and occurred at lower temperatures as the polymeric material acted as a seed for mesophase formation. Kim et al. found that the oxygen-containing groups in polyethylene terephthalate (PET) enhanced mesophase production in pitch, indicating the compatibility between the two materials [65]. They noted that the blends showed an increase in softening point and a decrease in coking value as the weight percent of PET increased. Other researchers found that PET would agglomerate in the CTP matrix if the PET weight percentage exceeded 25 wt.%, providing a limit for creating uniform fibers from a pitch-PET blend [66].

More recently, multiple studies have focused on blending mesophase pitch with linear low-density polyethylene (LLDPE) as a technique to increase the overall strain and strength of fibers while maintaining the graphitic structure and ideal modulus of pitch CF [67–69]. LLDPE has previously been converted into CF with a reported strength of 1.65 GPa and a modulus of 110 GPa, making it an ideal polymer to blend with mesophase pitch [70]. Additionally, the ability to blend a low-cost waste plastic such as LLDPE could further reduce the cost of pitch CFs, thereby creating a more competitive fiber capable of challenging PAN as the main feedstock for global CF production. However, limited research has been conducted on pitch blends with commodity plastics to produce CF [68,69]. Precursor fibers in these studies have diameters ranging from 100 to 200 microns [68,69] which greatly exceeds the maximum size for successful oxidation and carbonization [71].

3. Extrusion

In the second CF production step, the mesophase pitch is extruded into precursor/green fibers, which are wound onto a take-up winder and stored before further processing. For CF production, melt-extrusion is the ideal method for producing fibers with optimal diameters (<10 microns) in a continuous process. Several factors must be considered during melt-extrusion, as they can alter the CF properties. The most important factors are the pressure system, the nozzle and reservoir design, and the extrusion temperature.

3.1. Extrusion System

There are two extrusion systems predominantly used in mesophase pitch precursor fiber production. Batch-scale extruders are used for lab-scale and experimental runs, while single-screw extruders are well-suited for scaled-up, continuous production lines. Batch-scale extruders, also commonly referred to as single-shot extruders, operate by loading a certain amount of material into a closed, inert atmosphere and heating it beyond its softening point so it can be driven through a nozzle (**Figure 4**) [72]. The pressure mechanism is driven by a piston or by increasing the gas flow from a high-pressure tank. These systems have many advantages, including simple operation, low upfront costs, minimal material quantities, fast changeover between runs, and easy adaptability to new parts. For these reasons, this system is used for all the fiber production completed in this dissertation.

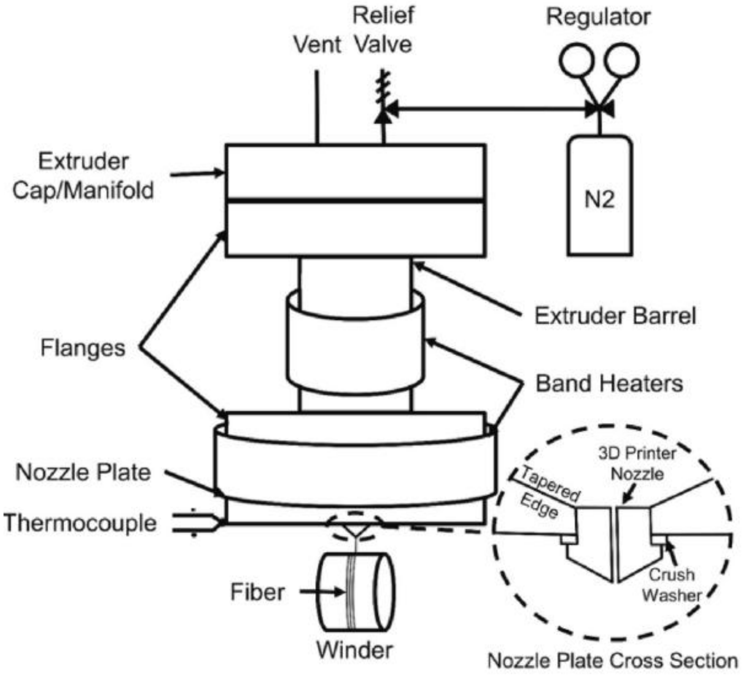

Figure 4. An example of a lab-scale pressure driven extruder used for the production of precursor fibers [73]

For all the advantages of a pressure-driven extruder, large-scale, continuous spinning requires a screw extruder for a constant material feed and high-volume production. Screw extruders have existed for decades and are used in a number of industries and materials; however, screw extrusion of mesophase pitch has not been widely reported, as the precursor fibers are brittle and fracture easily, making the process difficult. Therefore, industry specialists tend to keep information private, citing its proprietary nature. One group, Lim et al., presented a novel method of continuous pelletizing and extrusion for mesophase pitch (**Figure 5**) and found that this process resulted in increased tensile strength of the CF, highlighting the potential for scale-up required for MPCF to compete with PAN-CF [32].

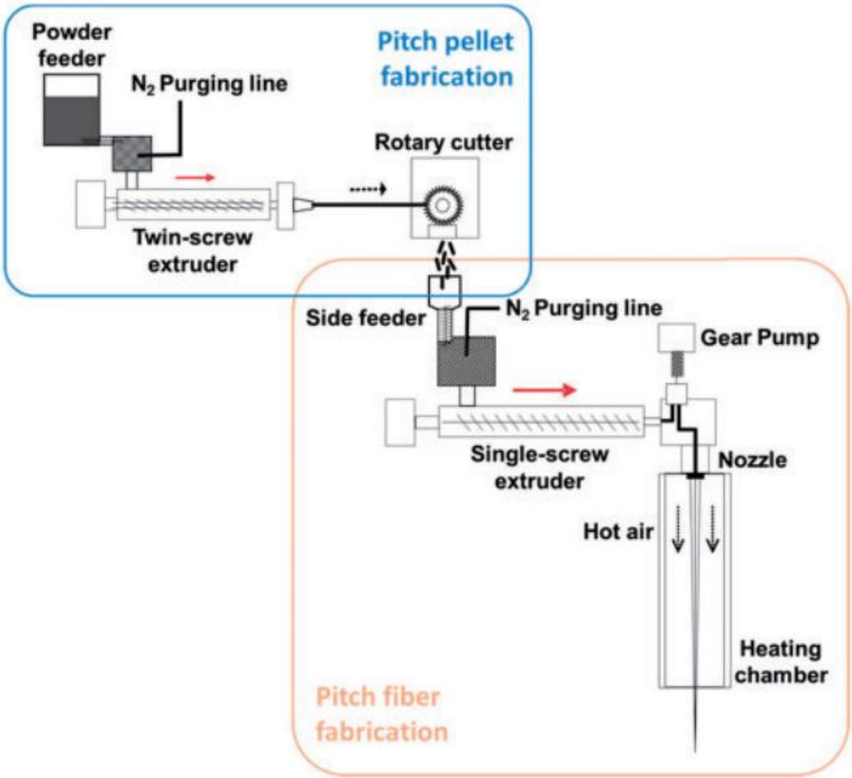

Figure 5. A schematic of the pelletizing of pitch via a twin extruder and fiber extrusion via a single screw extruder. This represents a cost and time effective, large-scale production method for mesophase pitch precursor fibers [32]

3.2. Spinneret Design and Mesostructure Formation

In fiber production, the spinneret refers to the system of nozzles and reservoirs, as illustrated in **Figure 6** [74]. The simplest systems consist of a single circular nozzle and a cylindrical reservoir with no edge tapering, located in the center of the spinneret plate [75]. Depending on the extrusion system being utilized and the feedstock material chosen, each factor in the spinneret must be considered. For MPCF, it has been shown that simple 3D printer nozzles can be used to create quality fibers with off-the-shelf parts [73]. For higher-end fibers, more specialized nozzles fabricated by machining equipment, such as wire sinker EDM, must be used to ensure tight tolerances and a smooth surface to avoid the formation of defects during fiber spinning. Additionally, other factors, including the draw-down ratio (the ratio of the nozzle diameter to the as-spun fiber diameter) greatly impact the CF properties, with a smaller ratio leading to a higher-strength fiber [76]. Any changes made to the spinning procedure must be carefully considered, as they will impact the structure of the CF microstructure.

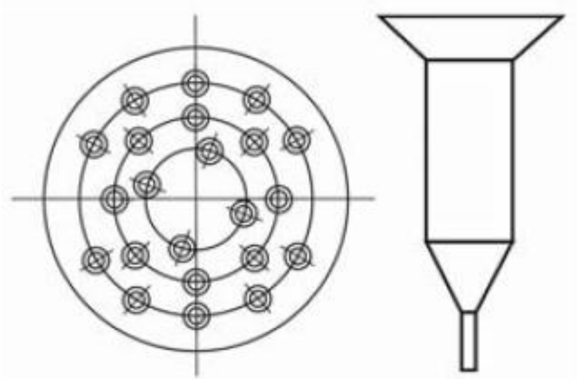

Figure 6. A top-down diagram of a spinneret (left) with multiple nozzles. A vertical cross-section of a typical nozzle (right) is shown highlighting the entry angles, reservoir, and exit [77]

The shear forces created during the spinning process deform the anisotropic spheres within the mesophase pitch, aligning them along the fiber axis and laying the groundwork for the CF structure [49]. The non-carbon atoms are removed through subsequent high-temperature heat treatment (carbonization), and the crystallites grow, leading to a more observable transverse cross-section texture. This texture is formed from the orientation of the mesostructure, which consists of ordered crystallite aggregates [78]. Depending on the orientation of the mesostructure, the texture of the fiber appears in cross-sectional patterns, which are used as naming conventions.

The properties of the CF are tied to their mesostructure. Early studies found that mesophase pitch could exhibit several different cross-sectional textures, such as “radial,” “random,” and “onion-skin,” all named for their visual appearances in electron micrographs (**Figure 7**) [79]. MPCF produced using a high shear stress-inducing spinning method will produce a “radial” texture because the mesostructure is radially symmetric to a point in the center of the fiber. In cases where the shear stress exceeds a certain threshold, the fibers will fracture and form a wedge-shaped void known as a pac-man split [80]. These CFs with radial textures, especially those with a pac-man split, have notably decreased tensile properties compared to CFs produced with different transverse mesostructure orientations.

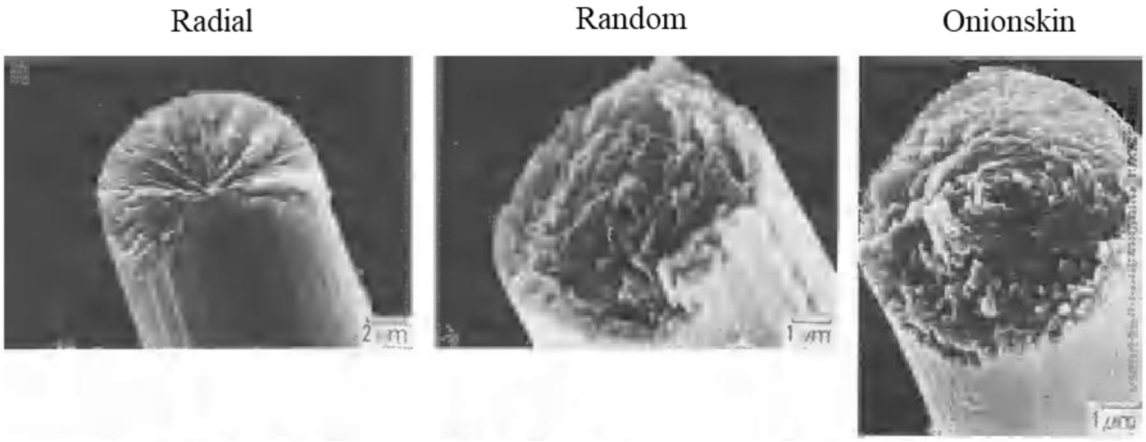

Figure 7. Examples of different textures found that can be found in MPCF [80].

Multiple studies have shown that different nozzle designs, including shape, diameter, length, and reservoir styles, affect the formation of non-radially oriented mesostructures [50,73,74,81,82]. Matsumoto et al. found that a reservoir with a noncircular cross-section, paired with a mesh filter, created “distorted-radial” structures that removed the pac-man split and increased tensile strength [75]. Mochida et al., by utilizing two synthetically produced mesophase pitches, naphthalene and methylnaphthalene, and varying extrusion temperatures, were able to achieve four unique transverse cross-section textures, all produced with the same nozzle [83]. Yao et al. produced radial CF with no pac-man split, despite using a high-shear nozzle style, by introducing and increasing the number of filters stacked together directly preceding the nozzle reservoir [51]. They also found that the CF produced with an increased number of filters had smaller microdomains, crystallites, and higher misorientation of the transverse mesostructure, though they did not report the corresponding mechanical properties.

4. Oxidation

Commercial-scale CF precursor materials, such as PAN, pitch, and cellulose/rayon, require thermal stabilization prior to carbonization [20]. Thermal stabilization, sometimes referred to as thermosetting, oxidation, or crosslinking, is performed on precursor fibers to enable the fibers to maintain their shape during carbonization and mitigating undesirable/premature decomposition stages that are inherently present in the precursor material [84]. Without thermal stabilization, the as-spun polymeric precursor fibers either melt, decompose, and/or fuse together upon heating to high temperatures during carbonization. Generally, thermal stabilization consists of polymer chain crosslinking and/or attachment of oxygen-containing functional groups onto the polymeric structure. Thermal stabilization of CF precursor fibers is a coupled diffusion-reaction process – the oxygen diffuses into the precursor fiber and then reacts with the polymeric material. Thermal stabilization is generally performed at moderate temperatures (200-300°C, below the polymer melting temperature) in an oxygen-containing environment with the process ranging from 0.25-24 hours depending on factors such as temperature, diameter, precursor type, and oxygen partial pressure [48,84–88]. On the commercial scale, thermal stabilization is usually kept relatively short (<1 hours) in the interest of cost. However, the effects of long-term oxidation (>48 hours) on the final CF properties have been noted by researchers [71,76,89,90]. The diffusion process is one of the many reasons that precursor fibers are usually spun to extremely small diameters of ≤10 μm.

Atmospheric pressure and composition are usually employed in the interest of keeping costs low, but the oxygen partial pressure can be altered to accelerate this process [91]. A wide variety of alternative stabilization techniques have been employed to improve the oxidation process such as plasma stabilization, sulfuric acid stabilization, nitric acid stabilization, and $KMNO_4$ stabilization of PAN [32,92–95]. The goal of these investigations is either to increase CF mechanical properties, reduce production cost, or investigate scientific phenomena. In 2010, Xu et al [96] investigated the use of gamma radiation to stabilize the fiber precursor structure. The use of gamma radiation was found to provide limited benefits in terms of CF mechanical properties. Coupled with the drastic increase in processing costs, the use of gamma radiation for the stabilization of CF precursors has not been pursued, at least in the literature. However, electron irradiation, a technique similar to gamma irradiation, was found to be very useful for the stabilization of polycarbosilane precursors to produce silicon carbide fibers, and silicon carbide fibers are currently still manufactured with this methodology [97].

Oxygen plasma assisted thermal stabilization of PAN precursor fibers has been explored [98–100]. The theory is that oxygen radicals present in the plasma have significantly higher rates of diffusion and reaction with the polymeric precursor fibers than standard O_2 molecules. Plasma stabilization has been extensively researched by 4M Carbon Fiber Corp. [101] and is currently being further developed for commercial-scale production lines. One of the benefits of plasma-assisted thermal stabilization is the potential utilization of large diameter polymeric precursors (>10 μm), owing to the increased rate of oxygen diffusion into the fiber microstructure [102].

Oxygen-assisted thermal stabilization of polymeric fibers is a finicky process. CF producers rely on sufficient diffusion of oxygen into the fiber microstructure, followed by the subsequent oxygen reaction with the polymeric chains/molecules. This coupled diffusion-reaction process depends on numerous factors, such as fiber diameter, fiber density, precursor material, and the stabilization parameters (temperature, time, and environment). An imbalance of either the diffusion or reaction processes can have dramatic impacts on the microstructure of the final CFs. As such, the production of high-quality CF requires optimization of these parameters in-tandem, which requires careful tuning on a production line.

Mapping techniques have shown that insufficient stabilization oftentimes yields a so-called core-shell or skin-core microstructure in produced CFs. Mapping with AFM across the fiber cross-sections has shown a large drop-off in mechanical properties in the insufficiently stabilized fiber core. Mapping the stabilized fiber cross-sections with EDS and FTIR has also yielded parabolic oxygen profiles, confirming that the core-shell phenomenon arises during stabilization, and persists into the carbonized fibers as shown in **Figure 8** [103–105]. In extreme cases of insufficient stabilization, the core can "melt out" of the fibers during carbonization, leaving a hollow-core CF [106]. This usually has negative results on the CF mechanical properties. However, it is worth mentioning that hollow-core fibers have been produced purposefully through manipulation of the precursor spinning process [107]. The increase in precursor fiber surface area has the potential to reduce stabilization time by increasing the rate of oxygen diffusion.

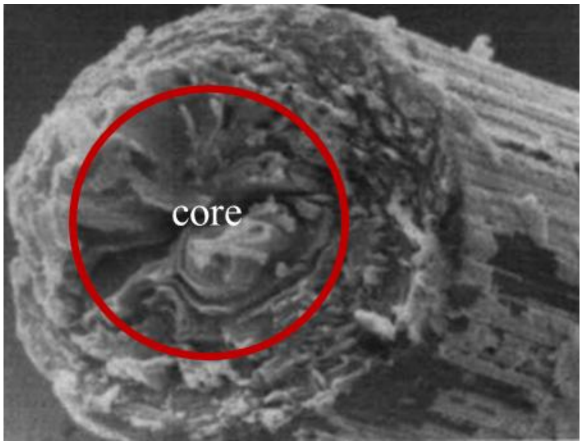

Figure 8. Example of a skin-core structure in a MPCF created from poor oxidation. Modified from [108]

5. High Temperature Heat Treatment

The final step in the production of CF is high-temperature heat treatment, in which the fibers are placed in an inert atmosphere (argon or nitrogen) and heated to at least 800 °C, resulting in fibers that are more than 92 wt.% carbon [109]. This heat treatment is typically divided into two stages, depending on the final temperature the fibers are subjected to. Treatment between 800 and 1800 °C is known as carbonization, resulting in the production of CF, while any heat treatment beyond 1800 °C is referred to as graphitization, with the resulting fibers known as graphitic fibers. Heat treatment of all feedstocks and temperature ranges has been studied for years, with many publications focusing on the effect of the final heat treatment temperature on the CF microstructure and subsequent mechanical properties [110–113]. Ultimately, heat treatment is crucial, as it is the point at which the crystal structure of the fibers develops, leading to their desired properties such as high tensile strength, modulus, and conductivity.

During carbonization, a 2-dimensional turbostratic microstructure in both PAN-CF and MPCF is developed. The lateral crystallite dimension (La) increases with increasing heat treatment in a continuous, expected manner for PAN-CF or any polymer-based fiber Additionally, some growth in the 3-dimensional crystal occurs with increasing heat treatment. For polymer-based fibers, increasing temperature within the carbonization range directly correlates with increases in the crystallite stacking height (Lc) and a decrease in the interlayer spacing (d002). MPCF exhibits a different trend, as the crystallinity of the fiber decreases in the 800–1000 °C range, and La only starts to grow beyond 1000 °C. There is virtually no 3-dimensional growth during carbonization for MPCF, as studies have shown that d002 and Lc remain virtually unchanged [44]. La for MPCF is larger and better oriented on average compared to PAN-CF when treated at the same temperature, as shown in **Figure 9**. As previously discussed, the liquid crystalline behavior of the pitch and large aromatic compounds found in the precursor material allow for larger crystallites at lower heat treatment temperatures and better crystallite orientation, which is formed during the spinning process.

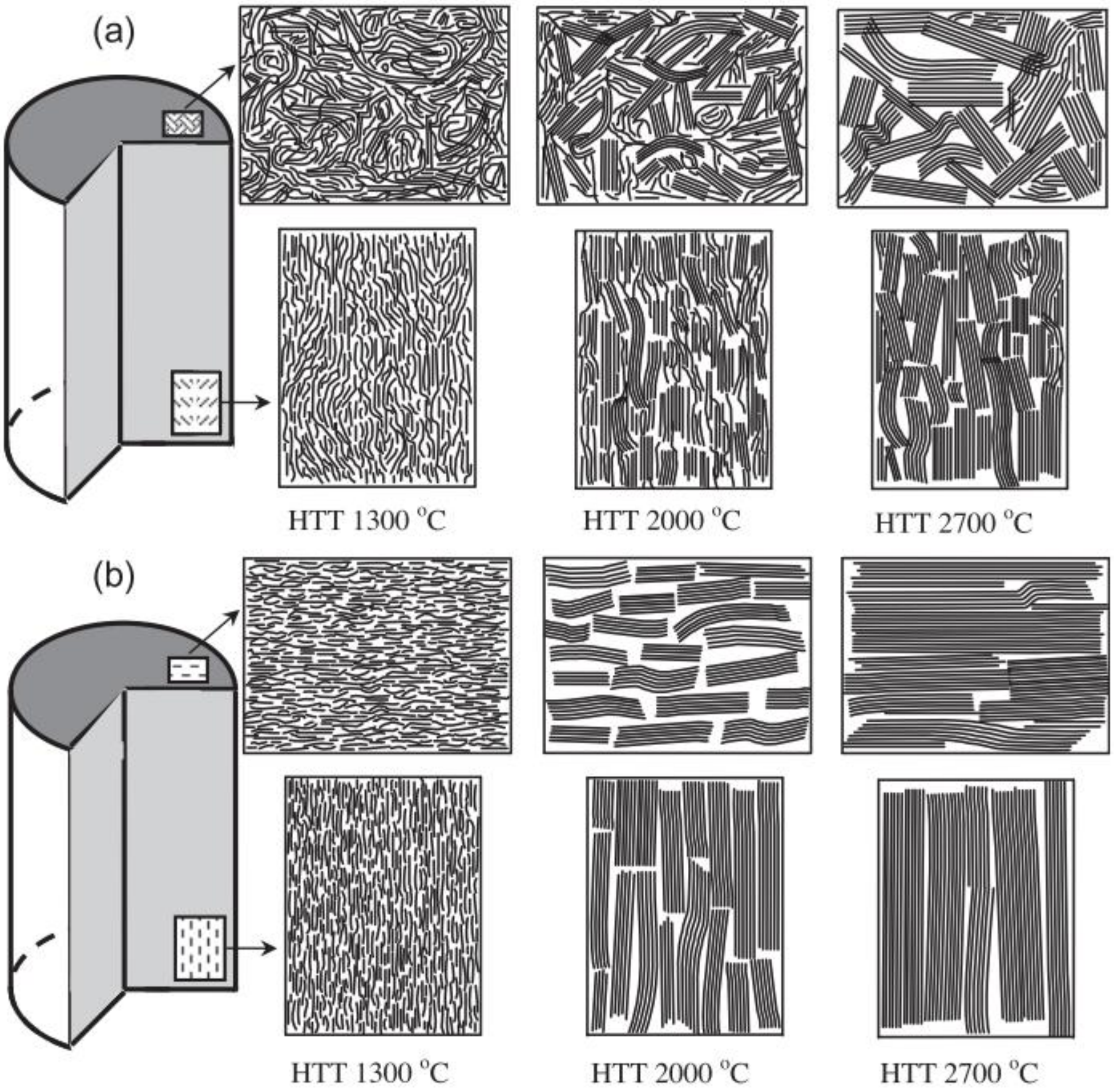

Figure 9. Sketches highlighting the microstructure for a) PAN-CF and b) MPCF. Adapted from [113]

Many studies have been conducted to correlate the microstructure properties with the macro-scale functions of CF in a structure-property relationship [114–117]. Notably, the PAN precursor allows for more cross-linking between layers and increased randomness in the structure formed during heat treatment. These factors contribute to the higher tensile strength of the fiber, as the layers are bonded and the random orientation allows for more relaxation when subjected to tensile force. It has been shown that PAN-CF reaches a maximum tensile strength at a heat treatment temperature of 1700 °C [118]. However, these same conditions make standard PAN-based fibers unsuitable for graphitization. At temperatures above 1800 °C, the tensile modulus of PAN-CF can reach roughly 400 GPa, but the tensile strength of the CF decreases from 5.4 GPa to 4.5 GPa [119]. Researchers believe this is due to the growth of microvoids and pores as the crystallites tighten, leading to increased spaces between the layers. Combined with fewer covalent bonds between the layers, the tensile strength is significantly reduced.

MPCF does not experience the same reduction in tensile strength as the heat treatment temperature approaches and enters the graphitization range. Instead, the tensile strength of the CF continues to increase slightly, while the tensile modulus can reach as high as 1000 GPa [113]. These property increases are due to the graphitic (3-dimensional) crystallite growth that occurs in MPCF at the graphitization level. Crystallites with a stacking height as large as 25 nm and a lateral length of 35 nm have been recorded [48,83]. When combined with the fact that the precursor material has a higher carbon yield and therefore less defect growth at higher temperatures, MPCF is a much better candidate for graphitization.

Besides the final heat treatment temperature, the carbonization ramp rate (the rate of temperature increase over time, °C/min) also plays a role in heat treating pitch [120]. Many believe that using a slower ramp rate and thus holding the fibers at higher temperatures for longer periods allows the crystallites to grow larger, leading to improved tensile and electrical properties. Rani et al. and their group investigated whether ramp rate—the time it takes to reach carbonization temperature—has any effect on CFs, focusing on times ranging from 20 to 80 hours to reach 1000 °C, or ramp rates of 0.81 °C/min and 0.2 °C/min, respectively [31]. They found that slower ramp rates resulted in larger crystallite sizes and a more graphitic structure. However, the ramp rates tested were so slow that they are irrelevant when compared to CFs produced at a commercial scale, leaving a gap in the literature.

6. Summary of Primary Research Questions

The production of MPCF is completed through a process consisting of four distinct steps. Each production step presents an opportunity to modify both the composition and structure of the material, leading to countless macro-property possibilities. However, each step also offers unique challenges that must be addressed and understood in order to produce a fiber with the desired characteristics in a manner that is both cost-effective and environmentally conscious.

For mesophase pitch feedstock production, multiple efforts have been made to improve the conversion of mesophase pitch from isotropic pitch, with the goal of decreasing costs via lower power requirements. Additionally, the mixing of waste polymers and mesophase pitch prior to spinning has been explored with limited success, leaving room for deeper investigation. Meanwhile, mesophase pitch extrusion is the most heavily investigated stage of carbon fiber production. This is because the extrusion of mesophase pitch lays the groundwork for the crystal structure exhibited in the CF and is visually represented in the texture shape of the CF cross-section. Regardless of the exhibited texture, stabilization via oxidation is the next crucial step.

Due to the rate of oxygen diffusion through the fiber, this process is slow and requires large amounts of energy due to the elevated temperatures required. In order to offset the associated costs, the shortest oxidation times are desired, but full oxidation is necessary to produce a quality CF, making the field a complicated give-and-take. Finally, high-temperature heat treatment in the carbonization or graphitization range is performed, depending on the end-use case of the fibers. It is at these high temperatures that the crystallites in the fiber grow, resulting in a stronger, stiffer, and more conductive material. While the effects of different final heat treatment temperatures have been explored in detail, the ramp rate remains an important factor that has not received the same amount of attention.

For all four stages, there are still many questions to be explored regarding their impact on CF structure, properties, and the role they play in the cost and environmental impact of CFs. These areas of focus give rise to four primary research questions.

How does combining mesophase pitch with recycled polymers affect CF properties and cost?

The majority of studies focus on the addition of waste polymers to isotropic pitch before anisotropic conversion, aiming to assist liquid crystal formation by acting as a nucleation site [63,65,121,122]. While important, these studies use a low weight percentage of polymer and do not attempt to leverage any of the polymers' physical properties, as the material is completely charred during treatment. A few publications have attempted to combine mesophase pitch with polymers through various mixing techniques right before extrusion, in order to produce a multi-material precursor fiber [67–69]. The idea stems from the hope that the high tensile strain of the polymers will be maintained through the extrusion and CF production process, leading to fibers with the stiffness of pitch CF but with improved tensile strain and, therefore, tensile strength. However, these efforts have resulted in precursor fibers with diameters greater than 100 μm, making it impossible to fully stabilize and carbonize them with any success. Therefore, the validity of precursor fibers created from a mixture of mesophase pitch and polymers, as well as the polymer's effect on the CF microstructure, cannot be determined without the production of thinner fibers.

How does a radial vs. random microstructure affect the CF properties?

Different cross-sectional patterns in MPCF have been discussed for decades, with studies examining various techniques for producing specific texture shapes and the mechanical differences between them [123]. The most common shape is radial, as it can be produced from a standard nozzle geometry with no alterations in the spinning process. Since the radial structure stems from high shear forces, it also lends itself to pac-man splitting, which greatly depreciates the tensile properties of the CF. To combat this effect, flow disruptions and different nozzle geometries have been utilized to produce a new texture with no specific pattern, known as random [51]. MPCF with a random texture has been shown to have higher tensile strengths and strains, with a slightly lower modulus. However, the microstructure of the random and radial CF has not been heavily investigated. A deeper understanding of the structure-property relationship between the cross-sectional texture shape and tensile properties is needed to explain their importance and role.

What role does oxygen uptake have on MPCF?

Oxygenated stabilization of mesophase pitch-based fibers is required to produce quality CF. For this reason, multiple studies have focused on various factors, including oxidation temperature, exposure time, oxygen concentration, and pressure [90,124]. To measure oxidation, weight gain has been used as one possible method. Weight gain is achieved by simply measuring the increase in sample weight after an oxidation procedure, without considering the amount of oxygen at different locations within the fiber. However, over-oxidation at the surface, with poor diffusion to the core, will lead to a core-shell structure, reducing the CF's tensile properties [87,125]. Therefore, correlating the oxygen uptake with the location of the oxygen within the fiber is essential to confirm successful oxidation.

Can the carbonization ramp rate be optimized for MPCF production?

The final heat treatment temperature used greatly influences crystallite growth, microstructure, and CF tensile properties, as the removal of non-carbon atoms leads to the formation of new carbon-carbon bonds. Studies have shown that the microstructure of MPCF varies greatly depending on the heat treatment temperature. The lateral crystallite dimension increases with temperature immediately, but the crystallite stacking height and interlayer spacing remain steady until temperatures exceed 1400 °C [44] . During the carbonization process, non-carbon atoms are removed, and new carbon-carbon bonds are formed, creating the microstructure that dictates the macroscale properties, highlighting the importance of the carbonization reactions.

While equally important, the ramp rate — which dictates the speed at which the fibers are heat-treated and how quickly the reactions occur — has not been as thoroughly investigated. A study has shown that slower ramp rates lead to larger crystallites, as the fibers are held at the reaction temperature for longer, allowing more bonds to form [31]. However, the fastest ramp rate used in this study was 0.8 °C/min, which is not comparable to those used in a commercial setting, leaving a gap in the understanding of ramp rates and their role in MPCF microstructure and macro-properties.

Each of these questions will be discussed throughout the next five chapters of this dissertation, followed by a summary and recommendations for future work based on the results. The results presented in Chapters 2 & 3 have been published in the *Journal of Polymer Research* [126,127], Chapter 5 has been published in *SMALL* [128], and Chapter 6 has been published in *Advanced Engineering Materials* [25]. As of the time this dissertation was published, Chapter 4 has yet to be published but is expected within the next year.

Chapter 2: Compatibility of mesophase pitch and linear low-density polyethylene for low-cost carbon fiber

1. Introduction

The goal of this study is to produce precursor fibers from blends of varying weight percentages of LLDPE and mesophase pitch that can be carbonized to study the effects on the resulting CFs. The produced blended precursor fibers are stabilized and carbonized using a traditional pitch oxidation/carbonization routine. The produced CFs are then characterized thermally to determine their char yield and mechanically to determine their tensile modulus/strength. In addition, the microstructure of the CFs were evaluated using X-ray diffraction, Raman spectroscopy, and fracture surfaces imaging. This study will evaluate the compatibility of pitch and LLDPE and the ability to produce quality CFs from a dry blend of the two.

2. Experimental Methods

2.1. Materials Preparation

The mesophase pitch used in this study was purchased from MotorCarbon LLC and used as delivered. The softening point was experimentally determined to be near 200 °C with a mesophase content of 75%. The LLDPE used in this study was purchased from Thermo Fisher Scientific and it arrived in powder form with an average flake size of 500 microns and a density of 0.92 g/cm^3 [126].

Select weights of pitch were ground and suspended in a solution of 300 mL of ethanol. LLDPE powder was then added to the solution in differing amounts to create samples with varied weight percentages outlined in Error! Reference source not found.. The total solution was mixed using a Silverson L5M-A shear mixer at 2500 RPM for 1 hour. After shear mixing, the solution was dehydrated for 24 hours at 80 °C to evaporate the ethanol and obtain a dry, dispersed mixture of pitch and LLDPE.

Table 1. Breakdown of different weight percentage blends of pitch and LLDPE

	Pitch weight %	LLDPE weight %
Blend 1	100	0
Blend 2	98	2
Blend 3	95	5
Blend 4	90	10
Blend 5	80	20

The blends of pitch and LLDPE were extruded using a custom lab-batch gas-pressure driven extruder. The mixture melts in a nitrogen atmosphere while the extruder climbs to a target temperature of 300 °C. The inert atmosphere prevents oxidative crosslinking and thus degradation. Once the extrusion temperature is reached, the sample is heat-soaked for 30 minutes to allow the sample to pass through the mesh filter and load the nozzle for extrusion. The filter removes any large particulates that act as impurities in the pitch precursor from the extrudable material to limit defects in the resulting fibers. The blended material was extruded through a 300 micron die. The fibers were wound onto a custom high-speed take-up winder. This method provided precursor fibers with diameters ranging from 15-30 microns.

The precursor fibers were oxidized at 280 °C in air under atmospheric pressure for 4 hours to allow for total oxygen diffusion while avoiding harmful over oxidation [89]. Once oxidation was completed, the fibers were cooled down to room temperature before carbonization was performed. The oxidized fibers were further heat treated at a low carbonization temperature of 1000 °C for 15 minutes in an Argon environment to produce CFs.

2.2. Characterization Methodology

DSC/TGA

Thermal analysis of the precursor fibers was performed simultaneously by differential scanning calorimetry (DSC) and thermo-gravimetric analysis (TGA) using a Netzsch STA 449 F1 Jupiter. The DSC/TGA was heated to 1000 °C with a heating and cooling rate of 10 °C/min under an inert (argon) atmosphere.

Microscopy

Polarized light microscopy was performed using a Hirox digital light microscope. The material was set in epoxy and then polished according to ASTM standard D4616-95 to take accurate images of a smooth surface. The imaged material came from the blended pitch and LLDPE that remained in the extruder after producing an adequate amount of fiber.

Scanning electron microscopy (SEM, FEI Quanta 650) was used to obtain images of fracture surfaces obtained from single-filament tensile testing. All samples were gold sputtered using a Cressington Sputter Coater to avoid charging during imaging.

Single Filament Tensile Testing

Single-fiber tensile tests were performed using a nanoscale tensile tester (MTS Nano Bionix UTM), which has a maximum load capacity of 500 mN and 150 mm of extension. All tests were run according to ASTM standard D3822-014 with the gauge length of 10 mm.

Microstructure Analysis

Raman scans of the CF were completed using a Renishaw InVia Confocal Raman microscope. Multiple scans extending from 200 cm^{-1} to 3200 cm^{-1} were run on the surface of multiple filaments.

The raw data was first corrected using an asymmetric least square smoothing method and then multipeak fit using a mixture of Lorentzian and Gaussian curves.

The crystal structures of the produced CFs were characterized by X-ray diffraction (XRD) using Cu K-α radiation ($\lambda = 0.15406$ nm) in the range of $10° < 2\theta < 70°$ (Malvern-Panalytical, Empyrean X-ray diffractometer). Bundles of filaments were aligned perpendicular to the X-ray direction to acquire equatorial scans for determination of d_{002} and L_c. Correction for instrumental broadening was not conducted, as the scans were performed for comparison reasons in this study.

3. Results and Discussion

3.1. Precursor Fibers

Figure 10 shows the melt puck of the blended pitch and LLDPE under polarized light. The isotropic pitch is identified by Brooks and Taylor spheres present in the mosaic structures known as anisotropic pitch [37]. The anisotropic pitch forms the liquid crystalline structure known as mesophase pitch [40]. This blend of isotropic and anisotropic material creates a pitch that is easier to extrude while still maintaining strong CF properties derived from a high anisotropic content. Introducing LLDPE does not alter the pitch structure. However, as can be seen in **Figure 10**b, the LLDPE agglomerates in the isotropic spheres and does not appear in the mosaic anisotropic phase. This agglomeration behavior was the first indication that pitch and LLDPE are not compatible as these materials were imaged post-extrusion leading to the conclusion that the LLDPE was most likely agglomerated in the same phases within the spun precursor fibers rather than being uniformly dispersed.

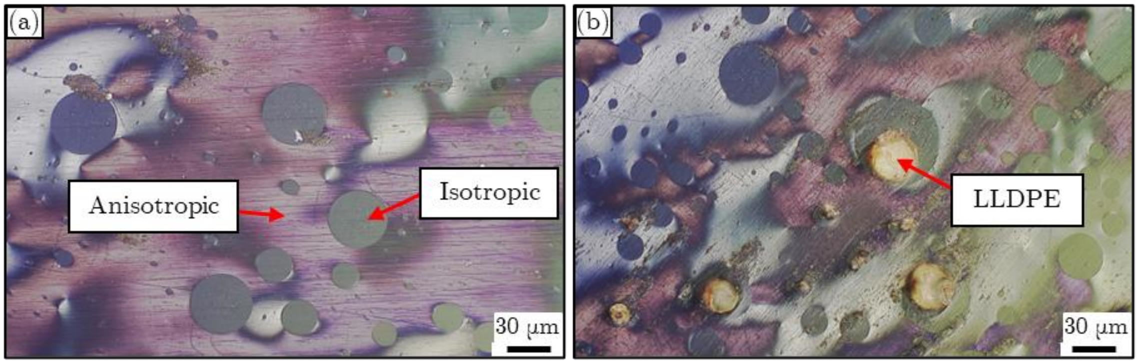

Figure 10. Optical images taken using a polarized light microscope in the transverse flow direction on a section of pitch: a) without LLDPE, b) with 20% LLDPE

Figure 11 presents DSC curves of the precursor fibers based on the weight percentage of LLDPE. All samples have an exothermic reaction near 270 °C, which is the crystallization temperature for the mesophase pitch. This peak is easily identifiable due to the high weight percentage of pitch in all samples. While all blends have a clear crystallization point, the glass transition temperature (T_g) is not clear for blends with 5% LLDPE or more. Pure pitch and 2% LLDPE show a transition temperature near 200 °C and although the softening point of pitch and T_g are not identical, studies have shown that they are related [127]. For blends containing 5% LLDPE or more, the melting temperature for LLDPE can be located between 125-128 °C. As the weight percentage of LLDPE increases, the melting peak becomes steeper and more prevalent while the crystallization peak widens making the T_g difficult to distinguish. These shifts in the curves between blends provide insight into the rheology of the materials and the need for different extruding parameters during melt spinning for further refinement. While all blends were spun at 300 °C, blends with higher weight percentages of LLDPE could have been extruded at lower temperatures, resulting in the ability to produce thinner precursors.

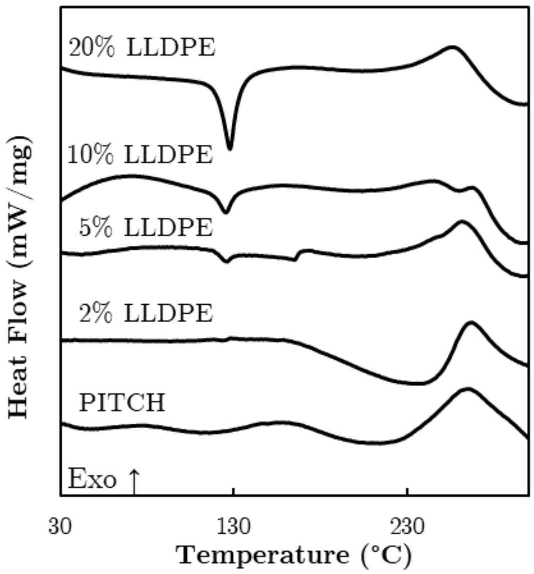

Figure 11. DSC of mesophase pitch precursor fibers with varying LLDPE weight percentages

Figure 12 shows the TGA and derivative thermogravimetry (DTG) curves of the different blends. As expected, changing the weight percentages affects the char yield of the blended material. TGA of the precursor fibers show a char yield of 86% for pure pitch which decreases to 76% at 20wt% LLDPE (**Figure 12**a**)**. The TGA curves also indicate larger slopes at the reaction onset temperature (200 °C) as the percentage of LLDPE increases. **Figure 12**b presents the associated DTG curves to quantify this increase in slope. This is due to the volatilization of non-stabilized LLDPE resulting in a larger loss of material when compared to the pure mesophase pitch.

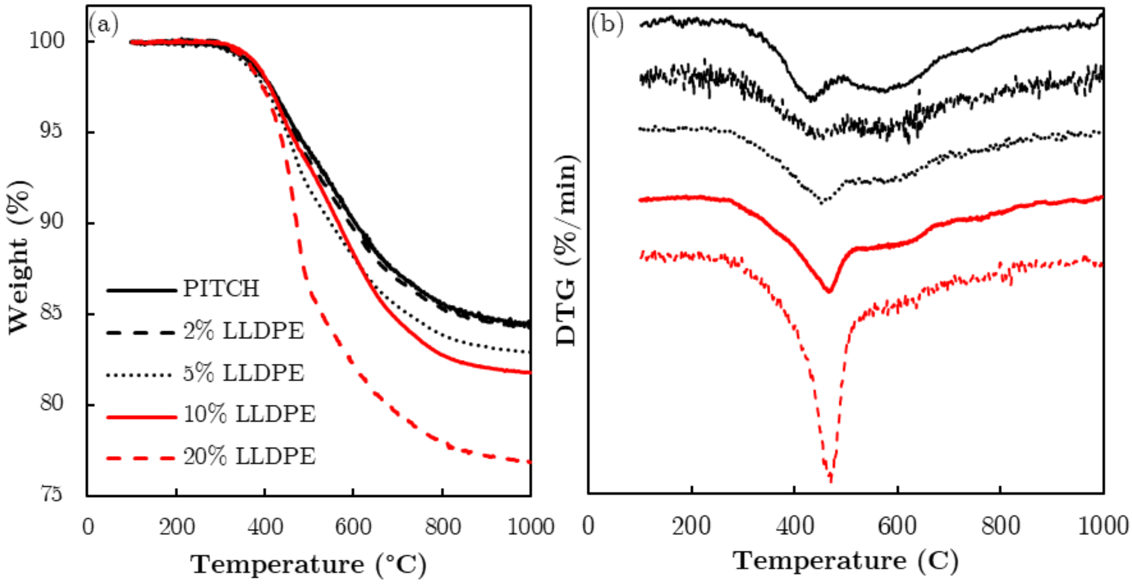

Figure 12. (a) TGA data and (b) DTG data for precursor fibers with varying weight percentages of LLDPE

The results of the single-filament tensile testing are shown in **Figure 13**a. The mechanical response of the samples varies greatly with increasing LLDPE content as found in previous work [31], [33]. At LLDPE contents less than 5 wt.%, the stress-strain curves are virtually linear and exhibit the brittle material behavior characteristic of pitch. At higher levels of LLDPE, the mechanical response changes dramatically to that of a two-phase material. This more complex behavior is graphically represented in **Figure 14**.

The first region (I) illustrates the initial loading on the precursor fiber. This region is dominated by the pitch component and is therefore linear in nature. Upon fracture of the pitch (region II), the load is transferred to the embedded LLDPE as previously seen in **Figure 13**b. The LLDPE then deforms elastically until it yields (region III) and begins plastic deformation (region IV) until ultimate failure. Precursor fibers blended with 20% LLDPE have an ultimate strain of 18.1% on average. For comparison, the average strain of pitch precursor fibers is 0.67%, 27 times smaller.

The increased ductility is a result of the plastic nature of LLDPE and is the desired tensile property to carry over to CF. It is important to note that precursor fibers containing 10% LLDPE were the weakest because there was enough polymer to disrupt the pitch matrix acting as large defects. However, the volume of LLDPE fibrils were then not able to handle the load transferred from the pitch matrix and immediately began to plasticly deform before ultimately failing at 2.9%.

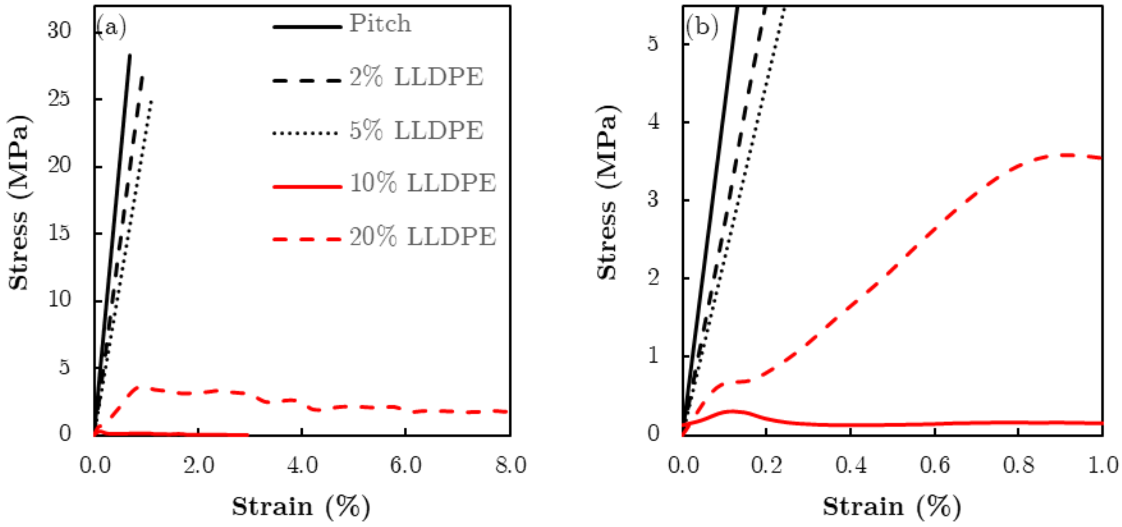

Figure 13. Tensile stress-strain curves for precursor fibers with varying percentages of LLDPE by weight: a) ultimate strength and b) transition region

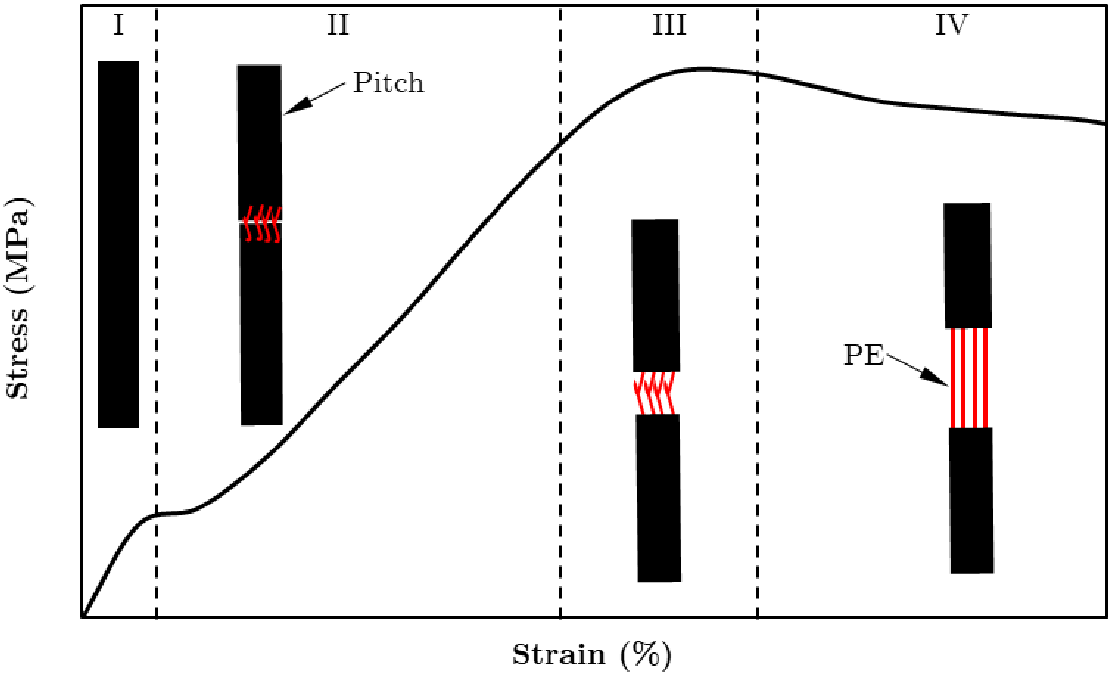

Figure 14. Graphical abstract of the two-phase behavior seen in pitch-LLDPE precursor fibers with a weight percentage of LLDPE 10 and higher

To further understand the tensile data, SEM inspection was performed on the fractured precursor fibers (**Figure 15**). The pitch portion of the precursor fibers (**Figure 15**a) shows smooth cleavage-like fracture surfaces indicating a brittle fracture. However, fibers from blends composed of 5% LLDPE and more (**Figure 15**cde) contain elongated, sub-micron diameter, circular fibrils comprised of LLDPE, which clearly indicates the plastic deformation of the LLDPE after the brittle fracture of the pitch. At LLDPE concentrations at and below 5%, the precursor fibers exhibit little to no plastic deformation. Therefore, the amount of LLDPE present was unable to withstand loading after the pitch fracture which explains the transition from a fully linear stress-strain curve to a two-phase behavior.

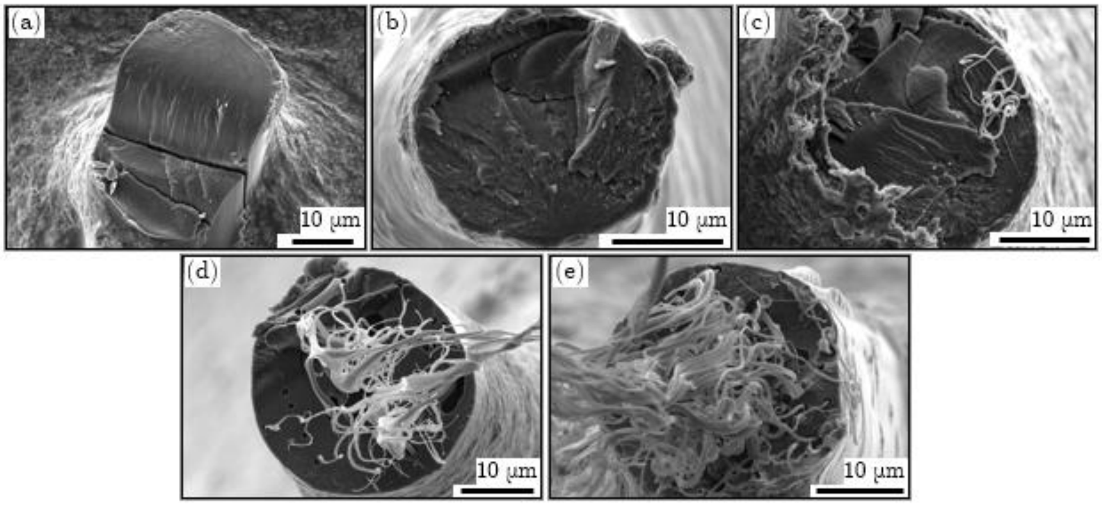

Figure 15. SEM images of fracture surfaces from precursor fibers with varying LLDPE weight percentages: a) 0% LLDPE, b) 2% LLDPE, c) 5% LLDPE, d) 10% LLDPE, e) 20% LLDPE

3.2. Carbon Fiber

All precursor fibers were successfully carbonized at 1000 °C. **Figure 16** presents the stress-strain curves for each CF produced from the different blends. Regardless of the weight percentages present in the precursor fibers, all CFs share the same linear-shaped stress-strain curves with no two-phase behavior present. The carbonization process removed the elastic nature present in the precursor fibers with higher LLDPE weight percentages which is representative of a uniform material. The uniformity of the materials occurs because of complexing between the pitch and LLDPE or the removal of one of the components. While LLDPE can be carbonized, it must first be sulfonated to be stabilized before further heat treatment [70]. However, sulfuric acid breaks down pitch, and so the precursor fibers were only oxidized in air for this study. Therefore, the LLDPE in the precursor fibers did not survive carbonization and was burnt off during the process, leading to defects in the CFs.

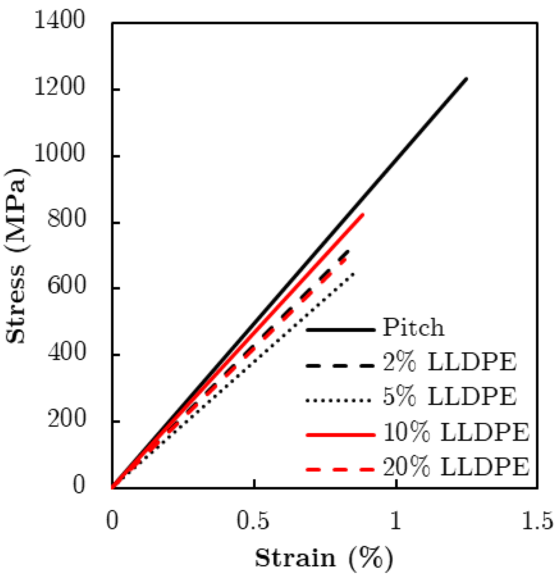

Figure 16. Tensile stress-strain curves for carbon fibers with varying LLDPE weight percentages

Although CFs produced from only pitch possessed strengths similar to other strengths reported for MPCF at low carbonization temperatures [80], CFs produced from blends showed a decrease in all tensile properties listed in **Table 2.** The decrease in mechanical properties is in line with previous work on defects in CFs [128–130]. Due to the LLPDE agglomeration seen in the precursor fibers, the burned off material left internal voids, weakening the CF structure leading to the decrease in tensile strength. However, the LLDPE agglomeration was random in both size and location for all blends, as shown by coefficients of variance (COV) for all tensile properties. An increase in COV percentage shows an increase in variability for a given property. With the introduction of LLDPE, the COV for CF strength increases for all blends showing the randomness of the defects and therefore the LLDPE agglomeration. The COV for modulus and strain also increase with the introduction of LLDPE further proving that the defects are both random in size and location thus leading to larger deviations.

Table 2. CF tensile testing results

	Strength		Modulus		Strain	
LLDPE %	(GPa)	COV (%)	(GPa)	COV (%)	(%)	COV (%)
0	1.23	12.4	99	4	1.24	12.1
2	0.55	22.6	86	19.4	0.86	24.7
5	0.52	23.9	76	19.4	0.85	28.6
10	0.63	27.1	89	11.6	0.88	24.3
20	0.54	24.2	84	14.9	0.82	27.0

The randomness of the voids created by the volatilization of the LLDPE was captured in SEM images (**Figure 17** and **Figure 18**). Voids were found throughout all CFs produced from blended precursors, as expected from the tensile data. **Figure 18** shows the classic striations observed on the surface of CFs with sub-micron voids present in the blended CFs. The size and number of voids were easier seen in the cross-sectional images in **Figure 17** with the largest voids by diameter were found in fibers produced from 5wt% LLDPE (**Figure 17**c) and 20wt% LLDPE (**Figure 17**e) while the CF produced from 10wt% LLDPE (**Figure 17**d) contained the most voids by number. This variation in size and quantity further explains the increase in COV for all tensile properties. Additionally, the fracture surfaces showed that different blend percentages altered the microstructure of the CF. The change from 0% to 2% altered the microstructure from random (**Figure 17**a) to planar polar (**Figure 17**b). Further increasing the LLDPE percentages reverted the microstructure back to random but produced a larger melt within the core of the fiber (**Figure 17**cde). While a shift in microstructure would result in varying tensile properties [47], the voids result in the CFs fracturing before the effect of different microstructures can be observed.

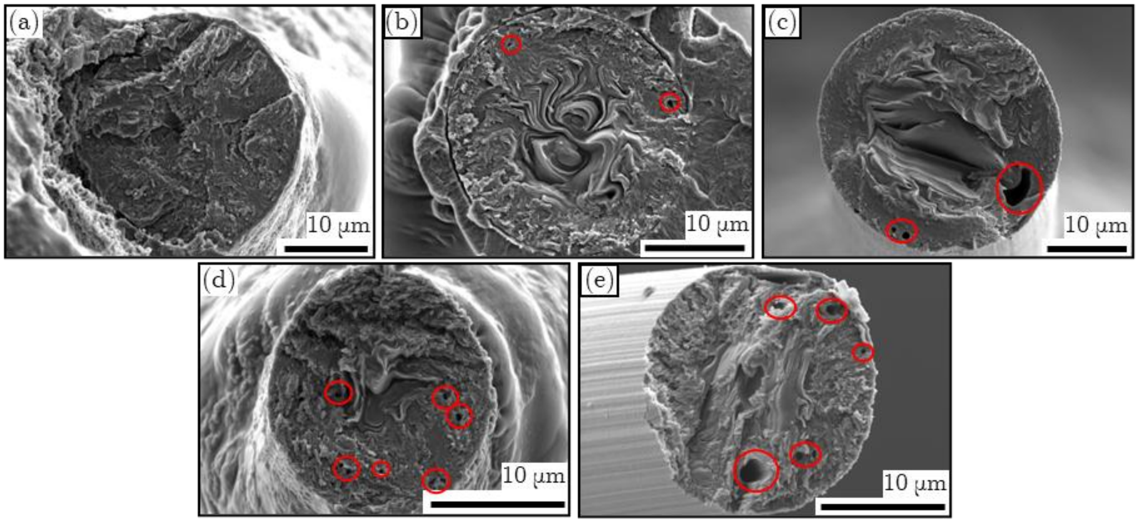

Figure 17. SEM images of fracture surfaces from CFs with varying LLDPE weight percentages: a) 0% LLDPE, b) 2% LLDPE, c) 5% LLDPE, d) 10% LLDPE, e) 20% LLDPE

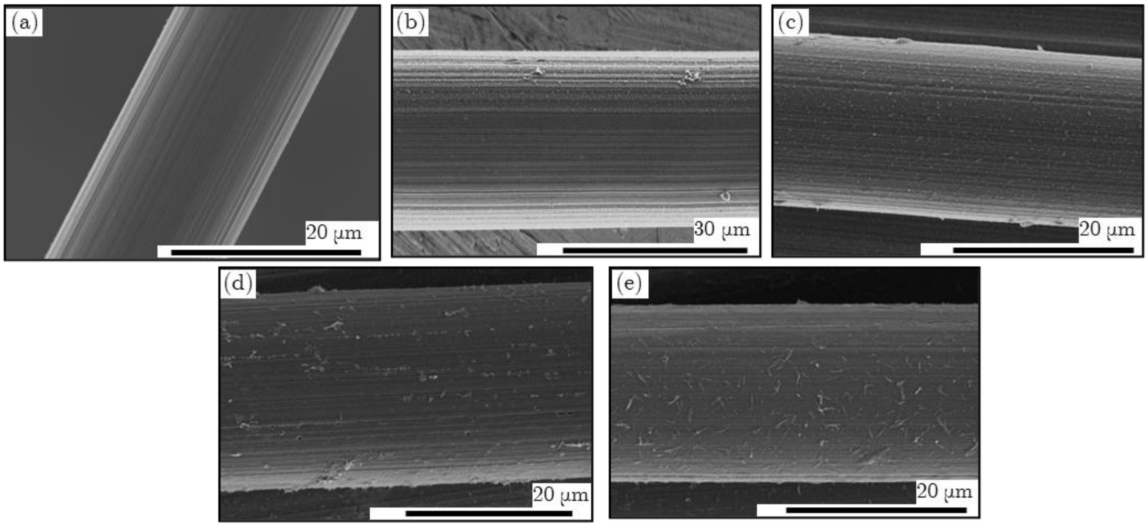

Figure 18. SEM images of fiber surfaces from CFs with varying LLDPE weight percentages: a) 0% LLDPE, b) 2% LLDPE, c) 5% LLDPE, d) 10% LLDPE, e) 20% LLDPE

Due to the shifting of the microstructure with the addition of LLDPE, Raman spectroscopy was utilized to further investigate microstructure differences in the CFs. **Figure 19** presents the raw Raman spectra separated by a constant factor for clarity. The same two peaks occur around 1375 cm^{-1} and 1600 cm^{-1} which have been classified as the D and G bands, respectively [131–134].

Previous studies have identified the D band as a representation of the disordered carbon structures in the fiber which normally presents in the 1330-1350 cm^{-1} region while the G band is related to the graphitic structure and symmetry within the CF and has been recorded ranging between the 1590-1620 cm^{-1}. The exact location of the D and G bands vary based on the curve fitting techniques used, heat treatment temperature, and other identifiable peaks. The ratio of the intensity of these bands, I_D/I_G, has been shown to correlate with changes in mechanical properties and microstructure differences [131]. To strive for consistency, the ratio is calculated using the areas of the curves produced by curve fitting software for the best accuracy [132].

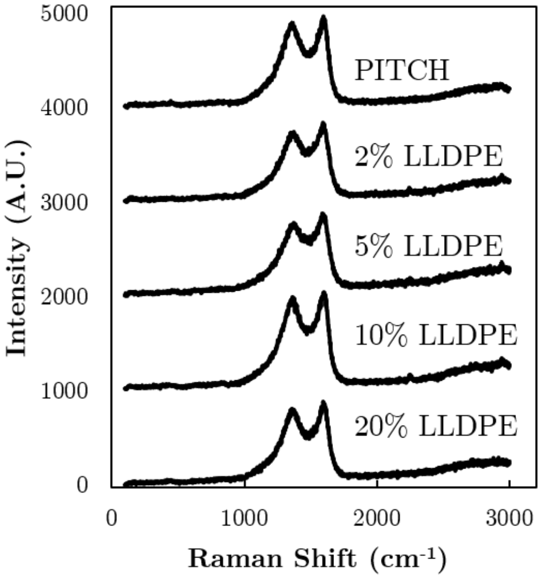

Figure 19. Raman spectra of CFs produced from varying weight percentages of LLDPE

Table 3 presents the data collected from the curve fitting of the raw Raman data. While there are some slight variations in the location and intensity of both the D and G bands, the differences are within one standard deviation thus showing no noticeable shifts. The same trend is found for the I_D/I_G values. When compared with literature, the CFs produced possess the same I_D/I_G as mesophase pitch which exhibits a I_D/I_G value ranging from 0.5-1.5 depending on the feedstock used and the final heat treatment temperature [133]. Due to a lack of noticeable shifting in the I_D/I_G, D, and G band properties, the CFs appear to be composed of one consistent material in line with the mesophase pitch properties, leading to the assumption that any LLDPE volatized leaving behind pure pitch CFs. This coincides with the SEM images shown in **Figure 17** and **Figure 18**, but due to the point scanning nature of Raman spectroscopy, XRD was also performed as a method to analyze the CF microstructure beyond the surface.

Table 3. Breakdown of Raman data from Lorentzian curve fitting for CFs with varying weight percentages of LLDPE. Full-width half-max (FWHM)

	D Band		G Band		
LLDPE weight (%)	Location (cm^{-1})	FWHM (cm^{-1})	Location (cm^{-1})	FWHM (cm^{-1})	I_D/I_G
0	1380.28	163.35	1598.58	102.47	1.15
2	1374.03	144.79	1594.53	116.87	1.09
5	1379.8	151.85	1601.47	99.22	1.19
10	1368.46	140.82	1604.71	86.33	1.08
20	1372.29	147.25	1603.09	92.79	1.17

Figure 20 presents the XRD spectra fitted using a multi-peak Lorentzian curve fit. The first peak found near 25° corresponds to the (002) reflection and the second peak located near 44.5° corresponds to the (10) reflection [135]. Due to the equatorial scan used to collect the XRD data, the (002) plane presents with the largest intensity while the (10) plane is only present due to misorientations of the graphite crystals along the fiber axis [136]. Theoretically, the presence of both bands allows for the estimation of crystallite sizes along both the a and c-directions using Scherrer's equation [112]. However, only L_c was calculated from the fitting of the (002) peak. To increase the signal-to-noise ratio for the peak (10) peak corresponding to L_a, a meridional scan of the fibers must be performed, which was not pursued in this study.

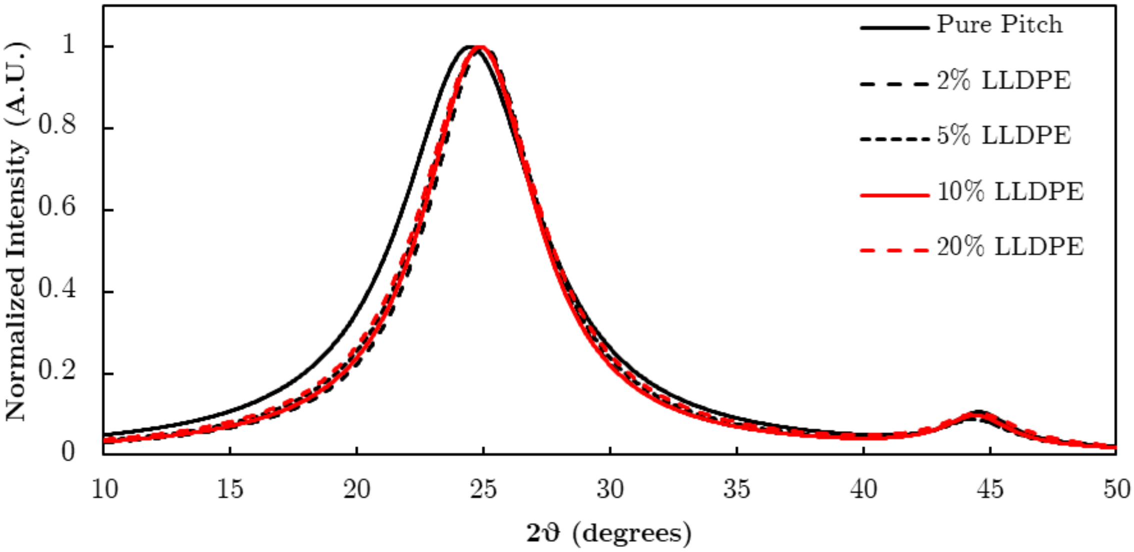

Figure 20. XRD spectra with Lorentzian curve fitting from CFs with varying weight percentages of LLDPE

The results of the curve fitting and subsequent calculations using Scherrer's equation are listed in **Error! Reference source not found.4** as well as the spacing between the basal planes, d_{002}, which was calculated from L_c. The position and FWHM of the (002) peak for all CFs produced from blends were within one standard deviation of each other; however, they were shifted from the CF produced from pure pitch. This shift could have been caused due to differences in the crystals or due to the inclusion of voids present in the CFs from blends. The L_c and d_{002} spacing were found to be within a standard deviation of each other for all CFs. Therefore, there is no difference in the crystallite structure for the different CFs and the shift must be present because of the presence of voids. With this knowledge, one can conclude that the findings from Raman spectroscopy are valid and that the CFs are all of one material, pitch, regardless of the blends from which the precursor fibers were spun.

Table 4. Breakdown of XRD data from Lorentzian curve fitting for CFs with varying weight percentages of LLDPE

LLDPE weight (%)	(002) Peak Position	FWHM (degrees)	L_c (nm)	d_{002} spacing (Å)
0	24.48	6.58	1.23	3.63
2	24.99	5.35	1.50	3.57
5	24.88	5.71	1.41	3.58
10	24.86	5.45	1.48	3.58
20	24.85	5.86	1.37	3.58

4. Conclusion

Precursor fibers were spun from blends with varying weight percentages of LLDPE and mesophase pitch. DSC data prove that increasing the weight percentage of LLDPE affects the thermal properties of the blend. Polarized light microscopy revealed that the LLDPE is incompatible with pitch and agglomerates in the isotropic spheres rather than uniformly dispersing throughout the pitch. Consequently, tensile testing of the precursor fibers showed a two-phase response. The precursor fibers were subjected to a high temperature stabilization before being carbonized to 1000 °C. CFs produced from blends with any weight percentage of LLDPE contain voids resulting in lower strengths compared to CF produced from pure pitch. Raman spectroscopy and X-ray diffraction were used to further investigate the microstructures of the CFs finding that the CFs were a uniform material with no variation between them beyond the presence of voids. This confirms that the agglomerated LLDPE did not stabilize and volatized completely during carbonization, resulting in weaker CFs. In summary, blending LLDPE with the mesophase pitch for low-cost CFs requires both compatibilizers and conversion processes.

Chapter 3: Exploration of fibers produced from petroleum based-mesophase pitch and PET blends for carbon fiber production

1. Introduction

This chapter aims to investigate if petroleum-derived mesophase pitch can be blended with PET to produce a fiber ideal for CF conversion. In this study, different weight percentages of PET were added to petroleum-derived mesophase pitch with the resulting blends spun into precursor fibers. The blends were investigated for changes in the thermal properties and molecular structure as possible insights into the compatibility of the two materials. The fibers were spun using a standard melt-spinning system and tensile tested to compare the mechanical properties of pure petroleum-derived mesophase pitch precursors against PET blended precursor fibers. The mechanical properties are recorded as well as the fracture surfaces and elemental composition of the produced fibers. Afterwards, an ideal precursor blend ratio was determined. A set of fibers from the ideal blend was oxidized and carbonized to be compared to CFs produced from only petroleum-derived mesophase pitch.

2. Experimental Methods

2.1. Material and Preparation

Petroleum-derived mesophase pitch was purchased from MotorCarbon LLC and was used as arrived. PET was purchased from Goodfellow in powder form with a maximum particle size of 300 microns and an average intrinsic viscosity of 0.8 dL/g [137].

Four different blends were created using pitch and PET powder each weighing 30 grams in total. Pitch was ground down and suspended in 500 mL of ethanol. PET was then added to create different solutions which were shear mixed for 2 hours at 2500 RPM using a Silverson L5M-A.

Post mixing, the solutions were immediately dehydrated in a forced air oven at 80 °C for 24 hours resulting in a powdered blend of pitch and PET broken down in **Table 5**.

Table 5. Breakdown of different weight percentage blends of pitch and PET

	Pitch weight %	PET weight %
Blend 1	100	0
Blend 2	95	5
Blend 3	90	10
Blend 4	85	15
Blend 5	80	20

The blends produced were extruded using a lab-scale pressure-driven extruder under an inert N_2 atmosphere to avoid early oxidation. All blends were extruded from a 100-micron diameter nozzle at 310 °C and were wound at 1500 RPMs resulting in a large range of fiber diameters. After examination, the precursor blend which showed the most promise was oxidized at 220 °C and carbonized in an Argon environment at 1000 °C.

2.2. Characterization Methodology

DSC/TGA

Thermal analysis of the precursor fibers was performed simultaneously by DSC and TGA using a Netzsch STA 449 F1 Jupiter machine. The DSC/TGA samples were heated to 500 °C with a heating and cooling rate of 10 °C/min under an inert (argon) atmosphere. Powder samples weighing 10 ± 1 mg were gathered from the material produced for extrusion and precursor samples were produced by cutting fibers into short pieces to fit within the platinum crucible.

Microscopy

Optical and polarized light microscopy was performed using a Hirox digital light microscope. The samples were retrieved from material leftover post-extrusion and were mounted in epoxy and polished according to ASTM standard D4616-95.

A FEI Quanta 650 SEM was used to obtain an energy dispersive x-ray spectroscopy (EDS) map of the fiber cross sections after polishing. SEM images of fracture surfaces were also obtained for both the precursor and carbonized fibers. All precursor fibers were gold sputtered using a Cressington Sputter Coater to avoid charging during imaging.

Fourier-transform infrared spectroscopy (FTIR)

A Bruker Invenio-S FTIR Spectrometer was used to determine the FTIR spectra for the produced blends and mono-materials. To minimize noise, 60 scans were completed with a 1 cm^{-1} resolution. PET was scanned using FTIR as arrived. The blends and mesophase pitch samples were scanned using the polarized microscopy samples.

Single Filament Tensile Testing

Single-fiber tensile tests were performed using a nanoscale tensile tester (MTS Nano Bionix UTM), which has a maximum load capacity of 500 mN and 150 mm of extension. All tests were run according to ASTM standard D3822-014 with a gauge length of 10 mm, a strain rate of 1e-4 s^{-1} for the precursor fibers, and a strain rate of 2e-4 s^{-1} for the CFs. The average strength, modulus, and strain of the precursor fibers were determined by the produced stress-strain curves.

3. Results and Discussion

Figure 21 presents the DSC curves produced from the pre-extrusion blends listed in **Table 5**. All blends show a characteristic exothermic peak around 260 °C known as the crystallization peak for mesophase pitch and can be seen in the sample of pure pitch. The temperature for crystallization of mesophase pitch varies depending on the feedstock material and manufacturing process of the pitch but can also be altered by the introduction of plasticizers and other carbonaceous materials. However, these blends were produced via shear mixing with no thermal or chemical reactions so there is no shift in the crystallization temperature. The blends with larger weight percentages of PET (15 and 20%) do contain an endothermic peak near 235 °C which is consistent with the melting temperature of PET [138]. This melting peak can only be seen in the higher concentration blends due to the noise of the machine, but it can be assumed that 5% PET blends do show similar melting characteristics.

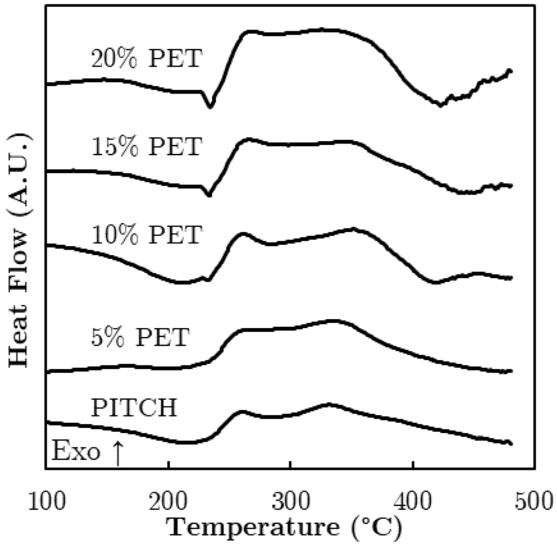

Figure 21. DSC of blended materials pre-extrusion

Since the two materials were mechanically mixed, TGA is used to separate the two materials capitalizing on their different burn-off rates (**Figure 22**a). Pitch possesses a much larger carbon content than PET and therefore has a higher char yield. PET has a char-yield of about 11% and the difference between the two is what makes TGA a valuable tool for studying the consistency of the blends. At 500 °C, the difference between each of the samples ranges from 4-5%. This proves the blends differ by 4-5% PET post drying and shear mixing ensuring no material was lost during blending and that all tests moving forward can work under the assumption that the blends ratios are accurate.

The extruded fibers were also tested using TGA to look for any differences between pre- and post-extrusion (**Figure 22**b). Although the extruder is run in an inert atmosphere, off-gassing occurs from both the pitch and PET and the two materials can be expected to react with each other when at such high temperatures for an extended period. The fibers were run to 1000 °C to search for any changes in the materials thermo-gravimetric profiles and to discern any important characteristics for CF production. At 1000 °C, the fibers produced from the 20% PET blend had the smallest char yield but only differed by 4% from the pure pitch fibers. All the fibers produced from the other blends fall somewhere between the 20% PET blend and the pure pitch, and with such a small difference in char yield it is safe to assume that the fibers do not contain the same weight ratios as the original blends. As already mentioned, this could arise from burn-off during extrusion or reactions occurring between the mesophase pitch and PET to form a more stable composite.

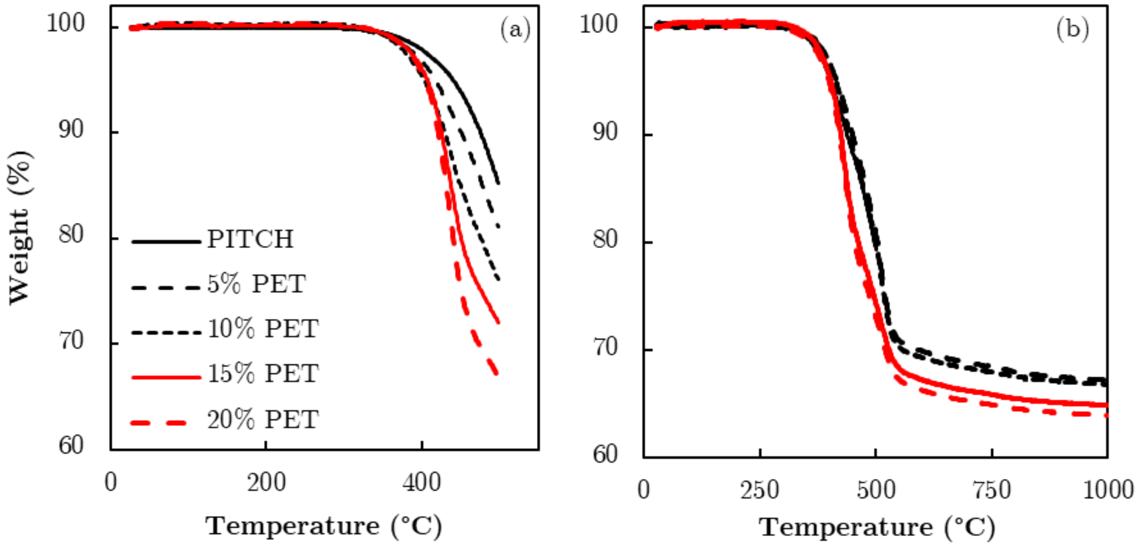

Figure 22. TGA of (a) powdered material pre-extrusion and (b) precursor fibers as spun

The new material created from the extrusion of pitch and PET would possess chemical signatures of both. Using FTIR, it is possible to examine a composite material and compare it to the scans of the two pure substances to determine whether the composite is in fact a mixture of the two materials. **Figure 23** presents the FTIR spectra for all the blended materials, pitch post extrusion, and as delivered PET powder. There are two noticeable differences between pitch and the blends which occur in regions (iii) and (v). The chemical structure for these regions is broken down in **Table 6** [139]. Both regions (iii) and (v) stem from oxygen included bonds which are not present in significant quantities for pitch. However, the FTIR spectra of the PET powder shows large peaks in these regions which is expected given PET's chemical backbone. Therefore, it can be concluded that the samples prepared post-extrusion do contain both pitch and PET and are suitable blends for further testing.

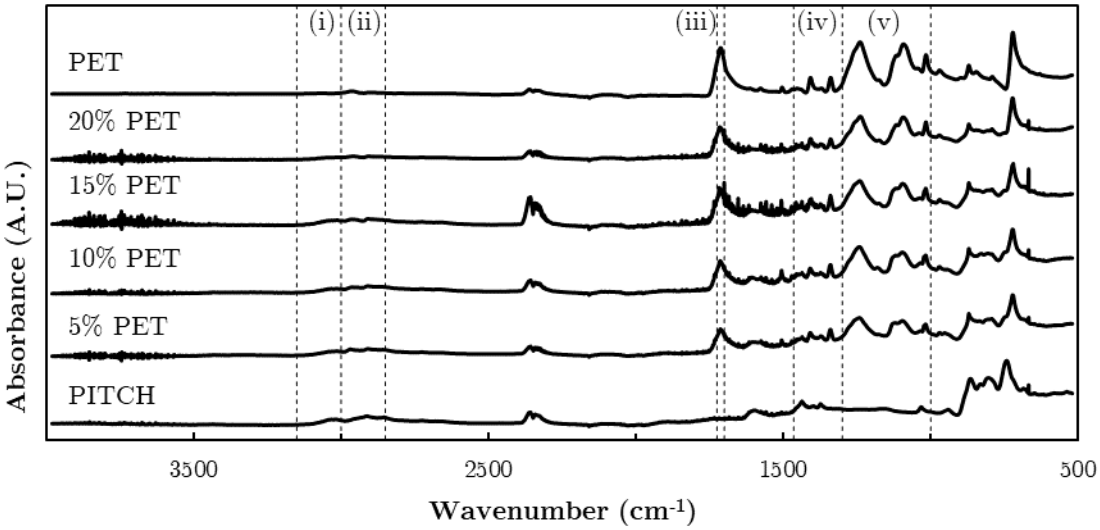

Figure 23. FTIR spectra of materials post-extrusion with varying PET weight %

Table 6. Breakdown of FTIR band assignments and labels

Label	Structure	Wavenumber (cm^{-1})
i	sp^2 C-H	3150-3050
ii	sp^3 C-H	3000-2850
iii	Carboxyl	1725-1700
iv	$CH_2 – CH_3$	1465-1375
v	C-O, OH	1300-1000

Next, the same sample pucks used for FTIR were observed under polarized light (**Figure 24**). The pucks show the standard pattern for pitch produced from a blend of mesophase and isotropic pitch. The anisotropic or mesophase pitch is optically reactive and creates the background with varying shapes and mosaics due to its liquid crystal nature [37]. Meanwhile, the isotropic pitch coalesces into spheres with a slightly darker tint due to a lower reaction to the polarized light. In addition to the mesophase and isotropic pitch, PET can be seen in each sample exhibiting a copper hue. For the blends created from 5 and 10 wt.% PET (**Figure 24**ab), the PET tends to agglomerate and form spheres which settle in the isotropic phase of pitch. This behavior has been noted and seen in blends created from pitch and LLDPE [140]. However, the blends with higher PET weight percentages (**Figure 24**cd) do not show the same agglomeration behavior. Instead, the PET appears to lose its spherical shape and starts to show a more liquid flow similar to mesophase pitch. This change in behavior indicates a critical PET concentration in the blend and that incorporating higher weight percentages of PET could lead to better mixing and compatibility between the two materials as the PET begins to spread out more evenly in the mixture rather than forming small, tight spheres in one region of the pitch.

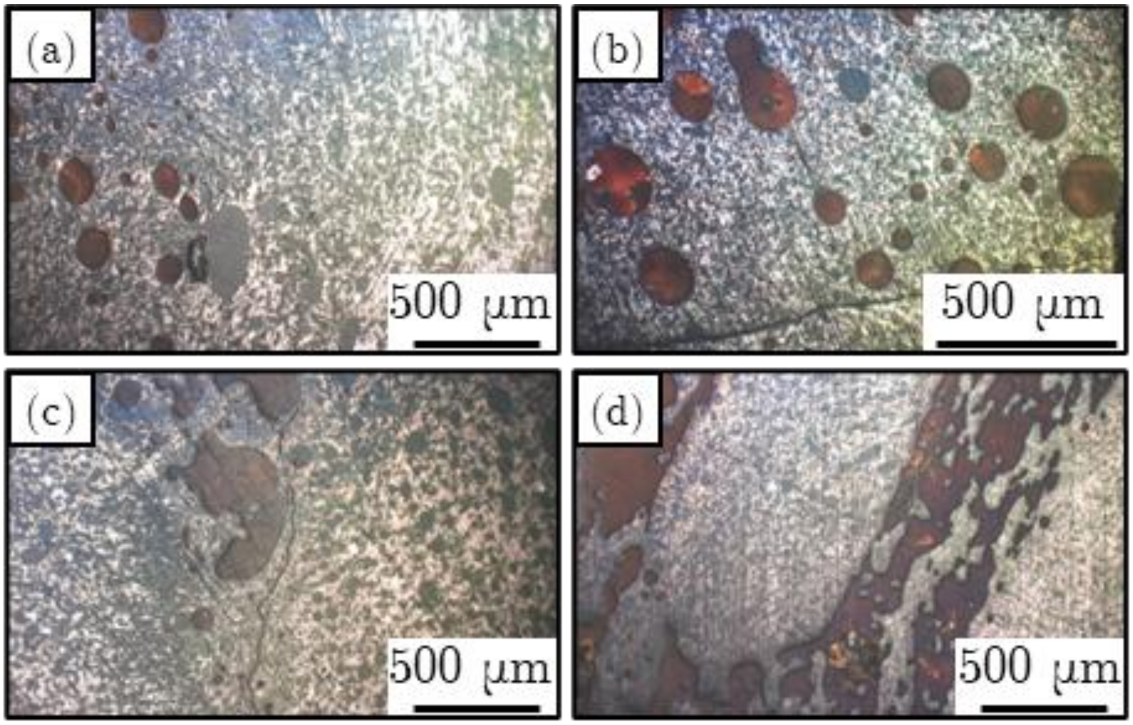

Figure 24. Polarized light images of post-extruded materials with varying PET weight %: (a) 5 wt.% PET, (b) 10 wt.% PET, (c) 15 wt.% PET, and (d) 20 wt.% PET

Seeing the distribution of the PET in the polished pucks, EDS of the extruded precursor fibers was used to probe for differences between the blends (**Figure 25**). An initial map of a pitch precursor fiber was completed to obtain the carbon and oxygen percentages to serve as a baseline (**Figure 25**a). The oxygen content of the pure pitch fiber averaged around 2% with no large variations across the fiber's cross-section. The fibers produced from blends were then scanned in a similar fashion with all of them possessing islands of increased oxygen content significantly above the 2% baseline. The source of these islands is attributed to the PET given it has an atomic oxygen composition of 18.2% as determined from its chemical formula $(C_{10}H_8O_4)_n$ [65]. All the islands contained approximately the same oxygen atomic percentage of 11.7% which is a decrease from the expected value for untreated PET. It should be noted that due to the high softening point of mesophase pitch, these precursor fibers were spun at temperatures above 300 °C. At these high temperatures, the PET decomposed and acetaldehyde was produced through off gassing. [141]. This kind of decomposition would yield a material with a lower oxidation percentage as found by EDS and explains the TGA results for the precursor fibers seen in **Figure 22**b.

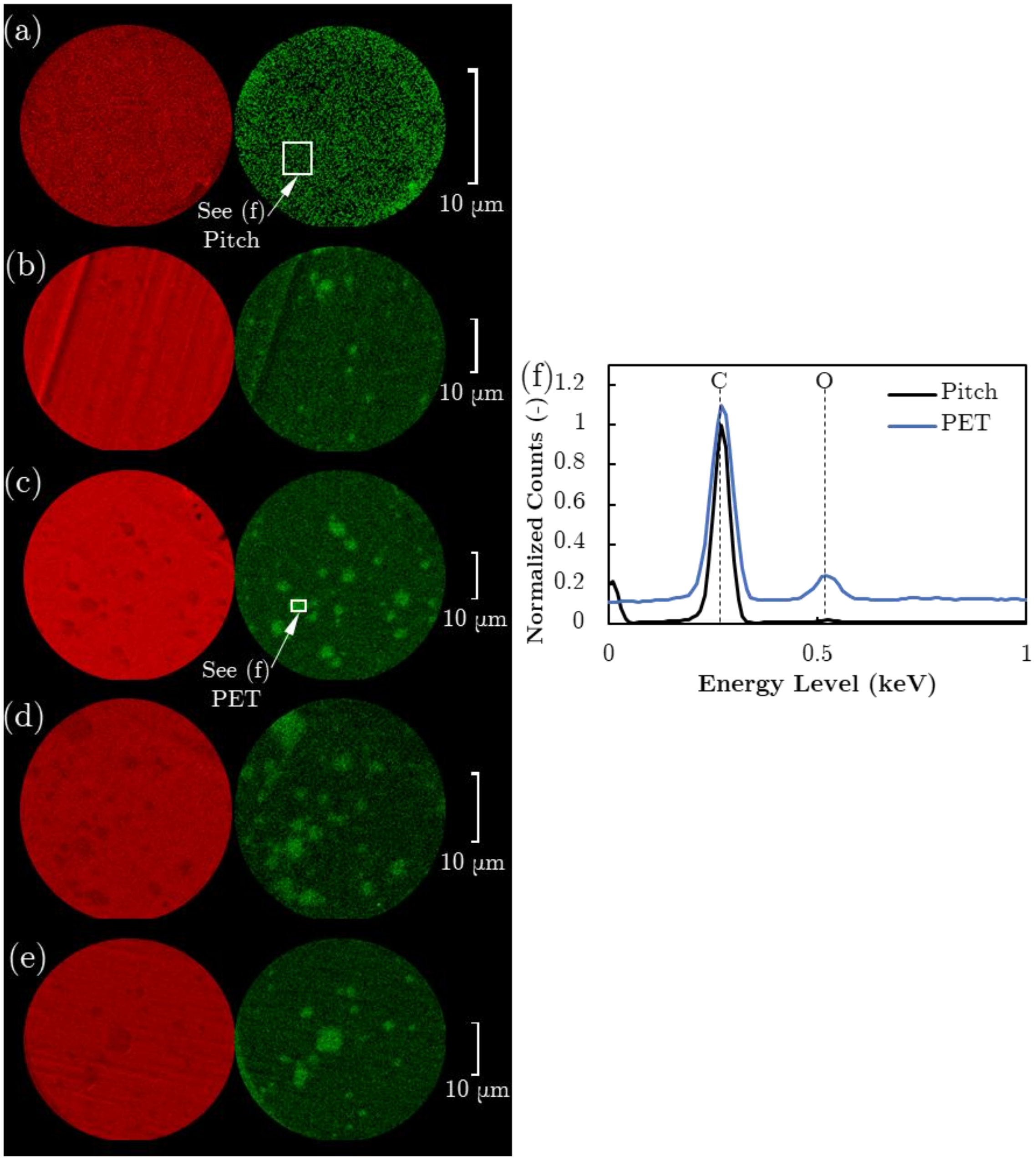

Figure 25. EDS map of the cross sections of precursor fibers with varying PET weight %: (a) 0 wt.% PET, (b) 5 wt.% PET, (c) 10 wt.% PET, (d) 15 wt.% PET, (e) 20 wt.% PET, and (f) spectra of normalized counts for carbon and oxygen of pitch and a PET island

The precursor fibers were tensile tested to discern the impact blending PET with pitch had on the mechanical properties (**Figure 26**). All fibers possessed a linear stress-strain curve characteristic for mesophase pitch due to its brittle nature. However, the blended fibers all showed a different modulus than that of pure pitch independent of the PET. The fibers with the largest ultimate strength were from pure pitch with the next strongest coming from the precursor fibers spun from 5 wt.% PET. The 5 wt.% PET fibers showed a strength decrease of 7.6% while having an improved strain of 219%, which is promising for a low cost, high strain CF should these properties carry through carbonization. It should be noted that while the other blended fibers share the same modulus as the 5 wt.% batch, they all showed decreased strength and strain values.

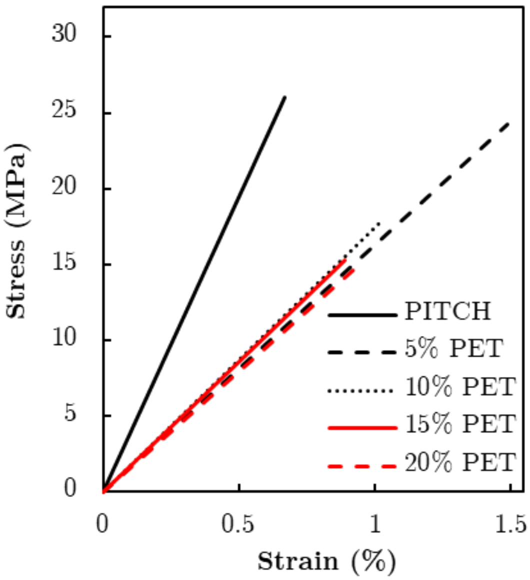

Figure 26. Stress-strain curves for precursor fibers with different PET weight %

Fracture surfaces from the tensile testing were preserved and imaged to probe the effects the PET addition had on the internal structure of the precursor fibers (**Figure 27**). Pure pitch (**Figure 27**a) had a smooth texture across its cross section which is standard for a brittle fracture. The same smooth face fracture can be seen in the 5 wt.% PET precursor fiber (**Figure 27**b) which is to be expected due to their similar mechanical strengths. The precursor fibers produced from 15 and 20 wt.% PET **(Figure 27**de) have significant distributions of macroscale defects and pitting on the cross section due to the decomposition of PET and explains why they have the lowest strengths at failure.

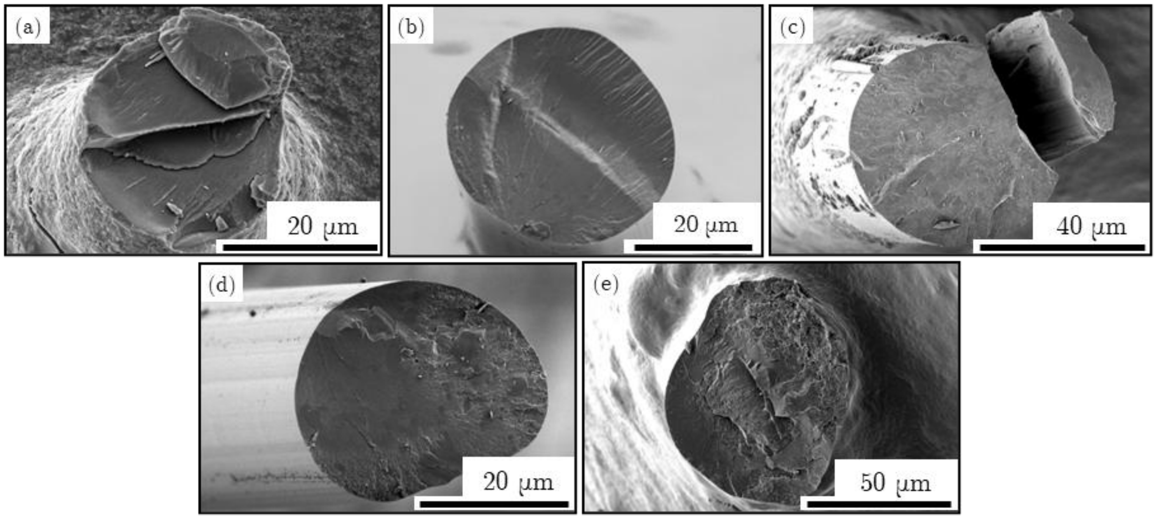

Figure 27. SEM images of precursor fibers post fracture varied by PET weight %: (a) 0 wt.% PET, (b) 5 wt.% PET, (c) 10 wt.% PET, (d) 15 wt.% PET, and (e) 20 wt.% PET

Fibers produced from the blend containing 5 wt.% PET showed the most promise as a CF precursor and were therefore oxidized and carbonized. The carbonized fibers were mechanically tested, and their tensile properties are listed in **Table 7**. Similar to the precursor fibers, pitch CFs have a higher tensile strength as compared to the CFs produced from the blend with 5 wt.% PET. However, the CFs produced from this blend are now stiffer, showing an increase in the modulus and a decrease in strain which is the inverse of the relationship for the precursor fibers and highlighting the effect the PET has on the CF microstructure. The microstructure of the CF, shown in **Figure 28**a, presents a radial structure with a random core. A skin radial-core random CF possesses a large tensile modulus as compared to a random microstructure due to more graphitic sheets being in line with the fiber's axis [83]. PET is a linear polymer with long chains which are pulled in line with the fiber axis due to shearing forces during extrusion. The shear force starts at the edges of the extrusion nozzle and diffuses inward resulting in a radial structure. The long, polymeric chains of PET assist in aligning the more aromatic molecules from the petroleum-derived pitch feedstock which then form graphitic sheets during carbonization. The same tensile results can be seen for the CFs produced from blends of CTP and PET when compared to CFs produced only from CTP [21]. A typical surface of the carbonized fiber is shown in **Figure 28**b.

Table 7. A comparison of pitch and pitch-blend CF mechanical properties

Mechanical Properties	CTP CF [142]	CTP-PET (5 wt.%) CF [142]	Petroleum pitch CF [140]	Petroleum pitch-LLDPE (5 wt.%) CF [140]	Petroleum pitch-PET (5 wt.%) CF
Strength (GPa)	0.525	0.474	1.23	0.52	0.91
Modulus (GPa)	23	26	99	76	109
Strain (%)	2.28	1.82	1.24	0.85	0.92

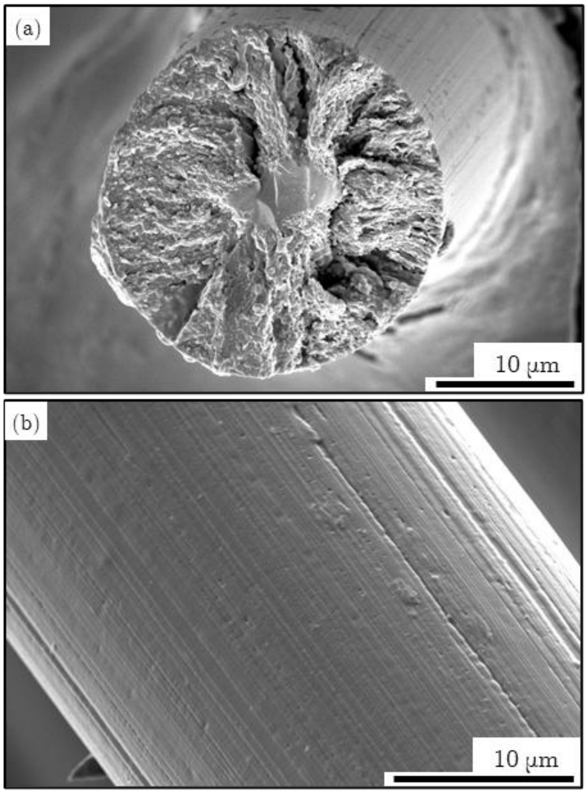

Figure 28. SEM images of the cross-section (a) and the surface (b) of carbonized fibers containing 5 wt.% PET

LLDPE has the same influence due to its linear chains. However, LLDPE is entirely volatilized during carbonization and leaves voids which decrease all CF tensile properties as compared to CFs produced from pure pitch [14]. To this point, blends of petroleum-derived pitch and PET show the most promise for creating a less expensive CF with suitable mechanical properties which can be used outside of laboratory experiments.

4. Conclusion

This study investigated the effects of blending PET with petroleum-derived mesophase pitch to produce precursor fibers and CFs. The introduction of PET into mesophase pitch leads to changes in the thermal properties of the bulk material. As the blends are spun, the PET decomposes and agglomerates leading to small pockets of higher oxygen percentage material within the precursor fibers. These blended fibers have different mechanical properties, the most significant of which being a decreased modulus independent of the amount of PET included in the original blends. However, the ultimate strength of the fibers decreased as the PET weight percentage increased. The most promising precursor fibers were created using a 5 wt.% PET blend and were thus oxidized and carbonized. The resulting CFs continued to show a decrease in tensile strength as compared to the CFs produced from pitch, but now possessed an increased modulus due to a change in transverse microstructure. This provides a framework for modifying the precursor material to achieve different CF mechanical properties which may be more ideal in certain settings while also decreasing the overall cost by blending in far less expensive feedstock.

Chapter 4: Comparative analysis of radial and random microstructures of mesophase pitch carbon fibers

1. Introduction

This study aimed to utilize a specific nozzle design and an established location for a single disruption filter to alter the microstructure of the resulting fiber. One batch was produced with a high-shear nozzle and no disruption filter to produce radial CF. A second set of fibers was extruded using a conical entry nozzle with a single disruption filter under the reservoir to disrupt the flow as late in the spinning process as possible. SEM was used to image the texture of the transverse cross sections. Tensile testing was carried out with fibers to determine their average mechanical properties, and they were then analyzed using Weibull analysis. Wide-angle x-ray diffraction (WAXD), small-angle x-ray scattering (SAXS), Raman microscopy, and transmission electron microscopy (TEM) were used to gather a complete picture of the CF microstructures. Ultimately, this work aims at further developing the understanding of the effects of different mesostructures on CF's micro and macro scale properties.

2. Experimental Methods

2.1. Materials and Preparation

The mesophase pitch used in this study was provided by MotorCarbon LLC and used as received. The mesophase pitch, called Meso-C, was found to have 75 vol.% mesophase content. Proximate analysis and total carbon and sulfur contents were carried out, with the results reported in **Table 8**.

Table 8. Total carbon, total sulfur, and proximate analysis performed on MotorCarbon's Meso-C mesophase pitch

Parameter	Result (%)
Total carbon	94.61
Total sulfur	0.58
Ash content	0.02
Moisture	0.13
Fixed Carbon	80.92
Volatile matter	19.06

Extrusion was completed using a lab-batch gas-pressure driven extruder. 100 grams of pitch was loaded before being sealed and flushed with nitrogen. Once an inert atmosphere was established, heating began until the nozzle extrusion temperature reached 310 °C. Pressure was increased until an even and constant pitch flow was maintained through a 14-micron mesh filter section to remove any solid impurities. Two 100-micron nozzles with different geometries were used to create two fiber types with unique microstructures. Both nozzles had the same length-to-diameter (L/D) ratio of 2, but one had a 1 mm cylindrical pitch reservoir while the other had a conical reservoir. This conical shape allowed a disruption filter to be placed directly above the nozzle so the pitch flow could be altered directly before spinning. The goal of the second nozzle was to break down any structure generated by the shear forces from the nozzle walls and produce a non-radial fiber. Both sets of fibers were wound using a drum with varying rotating speeds to achieve average precursor fiber diameters of 12.2 (±0.9) μm with a filter and 12.7 (±0.7) μm without a filter (**Figure 29**). A t-test was completed, and a p-value of 0.26 was found. Given this p-value, greater than 0.05, it was determined that the difference in the fiber diameters was not statistically significant.

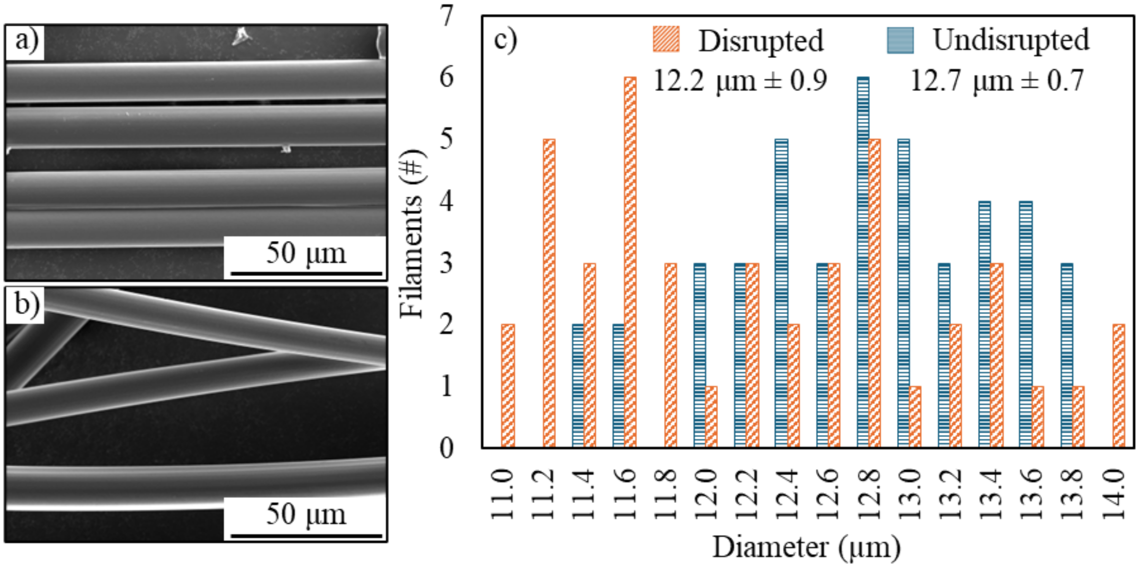

Figure 29. SEM images of precursor fibers produced a) without a disruption filter and b) with a disruption filter. A histogram (c) of the precursor fiber diameters created with disrupted and undisrupted flow is also shown with the calculated average fiber diameters

Both types of fibers were further processed with the same heat treatment. Stabilization was conducted at 210 °C to ensure complete oxygen diffusion while avoiding over-oxidation [87]. To check the quality of the oxidation procedure, EDS was carried out as a scan to measure the oxygen atomic weight percentage through the oxidized fiber cross-section (**Figure 30**) [143]. The fibers spun with and without a filter both had identical, flat oxidation profiles, signifying complete oxidation from the edge to the core of the fibers. Finally, carbonization was carried out in a GSL 1800X tube furnace at 1750 °C.

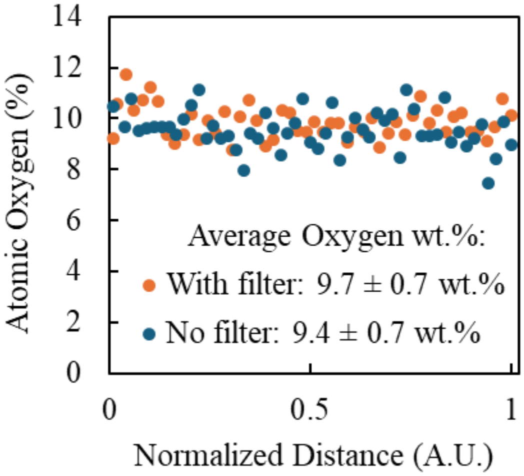

Figure 30. Oxygen wt.% across the fiber cross-section measured by EDS. The near-identical oxygen distribution between the samples indicates that variations in mechanical and structural properties cannot be attributed to different oxygen contents

2.2. Characterization Methodology

Single Filament Tensile Testing

The diameters of all CF monofilaments were measured using an Olympus BX53 optical microscope with a 50x objective lens and custom image analysis script prior to testing. The single-fiber tensile tests were run in accordance with ASTM standard D3822-014 on a nanoscale tensile tester (MTS Nano Bionix UTM). A gauge length of 10 mm and a strain rate of 1mm min^{-1} were used.

Weibull analysis was used to analyze the tensile test results further. Tensile strength is susceptible to defects and is primarily affected by sample volume [79,144]. Since the same gauge length was used for the CF tested, the radius of each CF is the only value that changes the sample volume. With this fact in mind, the Weibull parameters can be utilized to predict the CF strength at different gauge lengths given an identical diameter or the CF strength at different diameters given an identical gauge length [145]. The tensile strength of the radial CF was predicted at a diameter of 9.1 μm, the average CF diameter of the non-radial CF. This was done to ensure an even comparison between the CF regardless of any differences in their average diameters.

Electron Microscopy

SEM was completed using a FEI Quanta 650 field-emission SEM with an acceleration voltage set to 7 kV. The SEM images were all produced in secondary electron mode with an Everhart-Thornley detector. To avoid charging effects, the mesophase pitch precursor fibers were sputter coated with AuPd using a Cressington Sputter Coater. All cross-sectional images were produced by mounting the fibers vertically on an SEM stage and then sectioning using a fresh razor blade to minimize crushing and altering of the microstructures.

All TEM images and electron diffraction measurements were completed using a Themis Z 3.1 microscope operating at 300 kV. The samples were manufactured using a Helios UC G4 Dual Beam Focused Ion Beam-SEM. FIB milling was used to create a longitudinal section of 20 (±2) microns along the fiber axis which was 50-70 nm thick. It was then placed on a copper TEM pronged grid for imaging (**Figure 31**). FIB was chosen as the method to produce the samples as it maintains the structural integrity of the samples with the drawback of possible GA^+ ion implantation, which must be accounted for when analyzing the elemental composition of the section with a method like electron energy loss spectroscopy (EELS) [146]. Fast Fourier Transform (FFT) images were generated using ImageJ with a spectrum overlay for easy reading.

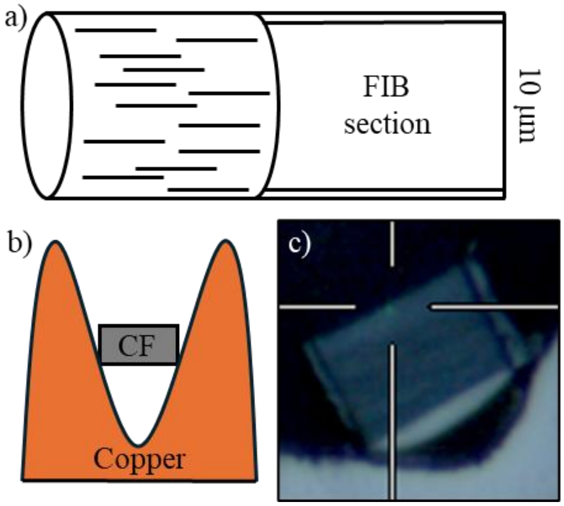

Figure 31. a) Schematic showing the section of the CF cut using FIB and b) the placement of the CF section on a TEM prong grid. c) A 50x image of the TEM sample

Raman Spectroscopy

The CFs were mounted vertically in epoxy and polished according to ASTM standard D4616-95 for cross-section analysis. Raman cross-sectional maps were obtained using a Renishaw 100 confocal Raman microscope with a laser wavelength of 532 nm. A point spectrum was taken from the center of the cross-section, and the maps were created with a 200 nm X–Y step resolution. The depth resolution is estimated to be less than 100 nm [147]. Following previous works, a curve fitting procedure including five bands was utilized to analyze each point spectrum using the Wire software (Renishaw) [6]. These bands were the I band (~1200 cm^{-1}), D band (~1350 cm^{-1}), G band (~1580 cm^{-1}), A band (~1520 cm^{-1}), and D’ band (~1620 cm^{-1}), as displayed in **Figure 32**. Only the D and G bands were used for the generation of the maps and any changes in the ratio of the D and G bandwidths, locations, and relative intensities (I_D/I_G) were investigated.

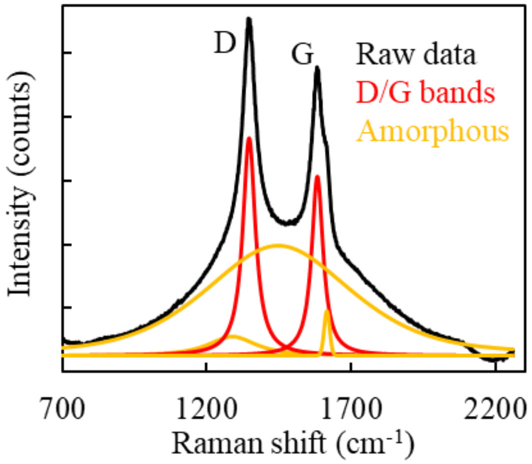

Figure 32. Raman spectra fitting used for the cross-sectional mapping. The D/G bands are shown in red as they are used for analysis, while the other bands are shown in yellow and were not used in any analyses as they stem from amorphous or small crystalline carbons

Using the Tuinstra-Koenig (TK) equation, **(1)**, with laser dependent coefficient, $C(\lambda_L)$, the crystallite size L_a was estimated using the average relative intensity ratio [148,149]. Depending on the wavelength used, $C(\lambda_L)$ can range from 44-120 Å [149,150]. For this study, a constant value of 44 Å was used. This estimation is only valid for crystallites with a $L_a > 2nm$ as the TK equation has shown to fail below this limit [132].

$$\frac{I_D}{I_G} = \frac{C(\lambda_L)}{L_a} \tag{1}$$

A separate method for calculating L_a by using the FWHM of the G band has been shown. Maslova et al. generated Equation **(2)** with a linear fitting of their FWHM values and L_a determined from XRD [151]. This relationship leverages the consistent nature of the FWHM(G) regardless of the wavelength laser used.

$$FWHM(G) = 14 + \frac{430}{L_a} \tag{2}$$

Wide Angle X-Ray Diffraction

WAXD was conducted with a Bruker D8 Venture utilizing Cu-Kα radiation at a wavelength of 0.154 nm. The scans were completed with the beam oriented perpendicular to the fiber axis and the 2D detector plane positioned perpendicular to the beam. The air background was subtracted, and the Bruker APEX4 software was used to integrate the 2D patterns into 1D patterns. Integration was performed along narrow slices along the equatorial and meridional directions, producing equatorial and meridional 1D patterns with a 2θ range of 10–106°. The crystallite sizes (Lc⊥ and La‖) were calculated from the equatorial and meridional patterns, respectively, using Scherrer's Equation **(3)**. Interplanar spacings, d_{002} and d_{10}, were calculated using Bragg's Law (4) [152].

$$L_{c\perp} = \frac{K\lambda}{FWHM_{002}\cos(\theta_{002})} \qquad L_{a\|} = \frac{K\lambda}{FWHM_{10}\cos(\theta_{10})} \tag{3}$$

$$n\lambda = 2d_{002}\sin(\theta_{002}) \qquad n\lambda = 2d_{10}\sin(\theta_{10}) \tag{4}$$

For Equation **(3)** and Equation **(4)**, λ is the wavelength of the x-rays, K is the shape factor, θ is half the profile fit Bragg angle (2θ), and n is the diffraction order. The FWHM of both peaks was found by fitting the 1D trace plots with pseudo-Voigt functions, and K was set as 0.9 for the (002) plane and 1.84 for the (10) plane [153]. It has been shown that the shape factor significantly deviates from these constants for crystallite sizes less than 15 nm, so some error should be expected when calculating $L_{a\|}$and $L_{c\perp}$ [154,155].

The average orientation of the graphite crystallites along the fiber axis was determined using the half width half max along the (002) plane of the azimuthal intensity. The orientation parameter, $\langle cos^2(\emptyset)\rangle$, was calculated using Equation **(5)** and Herman's orientation factor, f_{002}, was calculated using Equation **(6)** [119,156].

$$\langle cos^2(\emptyset)\rangle = \frac{\int_0^{\pi/2} I(\emptyset)\cos^2(\emptyset)\sin(\emptyset)\,d\emptyset}{\int_0^{\pi/2} I(\emptyset)\sin(\emptyset)\,d\emptyset} \tag{5}$$

$$f_{002} = \frac{1}{2}(3\langle\cos^2(\emptyset)\rangle - 1) \tag{6}$$

Small Angle X-ray Scattering

SAXS was performed with a Xenox Xeuss SAXS setup using an Excillum liquid metal jet Ga-source with a wavelength of 0.134 nm. The scans were completed on a single fiber with the x-rays parallel to the fiber axis and an exposure time of 1200 seconds. It should be noted that this is the first time that SAXS data has been obtained with an X-ray beam parallel to the fiber axis to our knowledge. The radial CF provides the optimum configuration for radially symmetric information with the least distortion due to the longer-range structure formation parallel to the fiber axis. A Dectris Pilatus 2D detector was used, and the SAXSutilities2 program was chosen to visualize the diffracted patterns. 1D azimuthal trace plots were generated for the entire phi region (360°) due to the expected radial symmetry.

Using the azimuthal trace plots, the natural log of the intensity multiplied by the wave vector, q, was plotted against q^2 to generate cross-section Guinier plots, which allows for analysis of the radius of the scatterer present in the CF. Many works have previously assigned needle-like pores as being responsible for the scattering present in the small q range ($q < 2\ nm^{-1}$) [157–161]. Recent articles have suggested that the scattering may be due to density fluctuations in the mesoscopic structures present in CF [78]. Regardless of the scattering origin, the method for determining the lengths of these scatters remains the same. The approximate average radius of gyration, R_g, of the scatterers can be determined using Equation **(7)**:

$$(qI) = (Iq)_o(\exp(-\frac{1}{2}q^2{R_g}^2) \quad \textbf{(7)}$$

Where R_g is estimated using the slope of the linear portion of the cross-section Guinier plot. To be valid, the q value must be sufficiently small such that $qR_g \leq 1$, also known as the Guinier region [162]. Depending on the expected shape of the scatter cross-section, the diameter, d, can be calculated. As previously mentioned, the accepted structure is a needle-like shape, which can be thought of as a rod with the long axis parallel to the long axis of the CF. Since these scans were parallel to the fiber's long axis, the expected cross-section would be circular [163]. Therefore, the diameter of the cross-section of the scatter can be determined with Equation **(8)**:

$$\boldsymbol{d = 2\sqrt{5/3}R_g} \quad \textbf{(8)}$$

3. Results and Discussion

Post carbonization, both sets of CF were imaged by SEM to observe the carbon microstructure of fibers extruded with and without a disruption filter. With no flow disruption, a typical radial microstructure with the graphitic planes converging towards the center was created (**Figure 33**a). This uniform alignment of the graphitic sheets can be best observed near the edge of the CF as shown in **Figure 33**b. This radial structure has been identified before and is produced due to shearing forces during extrusion which align the liquid crystal mesogens in the mesophase pitch. Due to the long, cylindrical reservoir, no disruption filter, circular nozzle geometry, and a L/D of 2, a radially uniform structure was expected [83]. The relatively large shearing forces are equal around the entire edge, leading to a focal point in the middle of the fiber.

The second nozzle used in this study consisted of a large, conical reservoir. This geometry significantly dissipates the shear forces effect on the microstructure, given that more volume per surface area is allowed to pass through the reservoir. Paired with a disruption filter at the nozzle entry, any structural developments should be distorted. This was done to create a "random" microstructure, observed and shown in **Figure 33**c. The edge alignment (**Figure 33**d) better highlights this effect. It displays the highest order, but the graphitic planes show no order in the transverse directions. The difference in observed textures shows that a combination of nozzle geometry and disruption filters formed two unique microstructures. From this point, sample 1 CF spun with no disruption filter will be referred to as "radial CF," and sample 2 CF spun with a disruption filter will be referred to as "random CF."

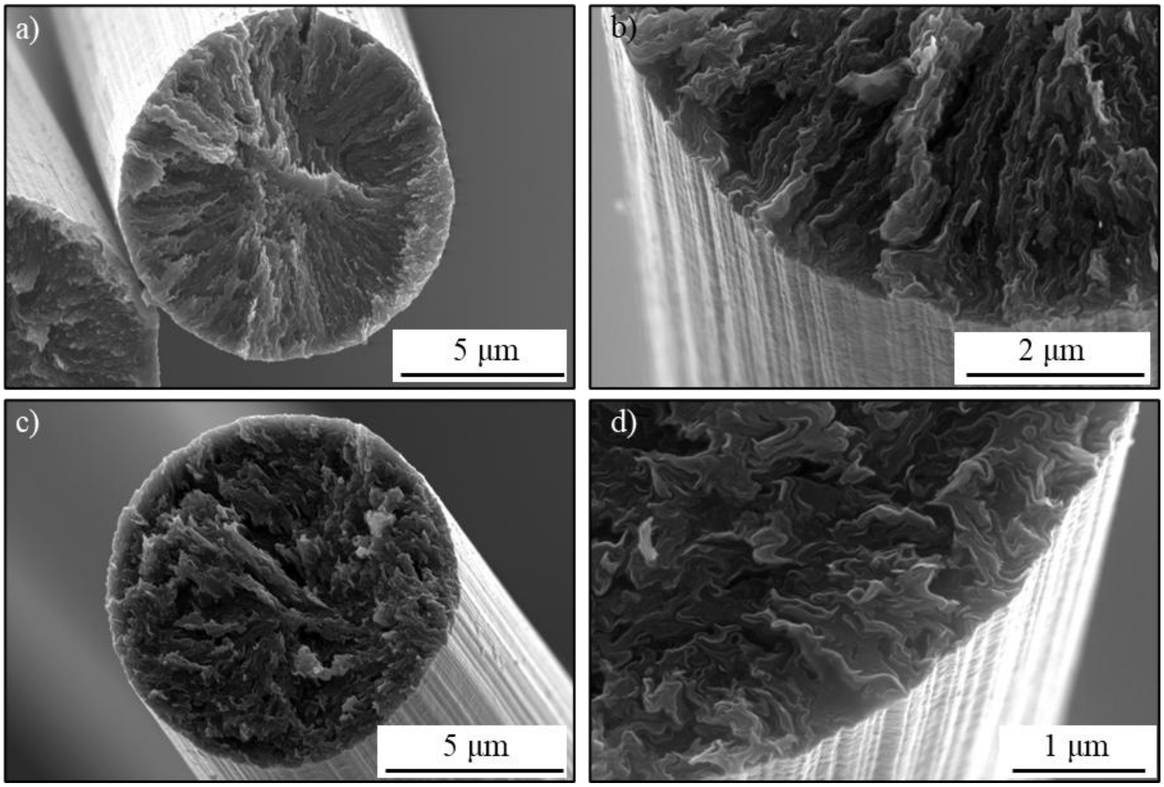

Figure 33. SEM of the radial CF' a) transverse cross-section and b) edge plane alignment. The radially symmetric structure is visible. SEM of the random CF' c) transverse cross-section and d) edge plane alignment where structure at similar length scales can be seen without radial symmetry

Before tensile testing, the diameter of each fiber was measured using an optical microscope with a 50x lens (**Table 9**). The random CF showed a 25.3% (±4.2) decrease in diameter compared to their precursor pitch fibers, while the radial CF' diameter decreased by 21.4% (±2.2) on average. The increased shrinking rate of the random CF was thought to be due to the decrease in transverse orientation, which allowed for more shrinkage in that direction. The average tensile properties and their associated standard deviations, based on a set of 20 filaments, are listed in **Table 9**. The random CF showed superior strength, modulus, and strain at break. This aligns with previous works showing that mesophase-pitch-based CF with a random microstructure is tougher, with a higher strain to failure [83]. This has been attributed to relaxation in the graphitic sheet alignment, which increases strain with a minimal loss in modulus, leading to an overall increase in tensile strength.

Table 9. Diameter measurements and mechanical properties for the radial and random CF

	Diameter (µm)	Tensile strength (GPa)	Tensile modulus (GPa)	Strain at break (%)
Radial	9.98 ± 0.49	1.69 ± 0.56	252.1 ± 34.3	0.68 ± 0.21
Random	9.10 ± 0.87	2.23 ± 0.71	287.5 ± 52.9	0.78 ± 0.21

When comparing the mechanical properties of CF, Weibull statistical analysis has proven to be the most reliable method, as it removes the uncertainties caused by variations in the average fiber diameters. **Figure 34**ac displays the linear fittings of the CF strengths in Weibull coordinates and the equation of the best linear trendline fit. The shape factor, a, is determined from the slope of the line, giving a value of 3.1 (±0.12) for the radial CF and 3.2 (±0.15) for the random CF. A typical shape parameter for commercially available CF ranges from 3-10, with a larger α indicating a homogeneous flaw distribution, smaller defects, and a lower scattering in tensile strength [164]. For a value of α between 3-4, Weibull approximates a normal distribution [165]. The shape parameters for the radial and random CF are at the bottom of the range for commercial CF, but the linear fit is of quality, as shown with both fits having an R^2 value greater than 0.9, and the Weibull predicted probability of failure can be plotted against the experimental results (**Figure 34**bd). The predicted fit is aligned with the experimental results, ensuring the calculated Weibull parameters are accurate.

Weibull analysis was used to predict the strength of the radial CF with the same average diameter as for the random CF. The predicted tensile strength of the radial CF was 1.79 (±0.19) GPa at 9.10 μm compared to the measured strength of 1.69 GPa at 9.98 μm. This is still a 20% decrease in tensile strength compared to the random CF's measured strength. This is significant and proves that the difference in mechanical properties of the two sets of CF is not diameter-dependent and is instead directly related to the different carbon microstructures of the CF.

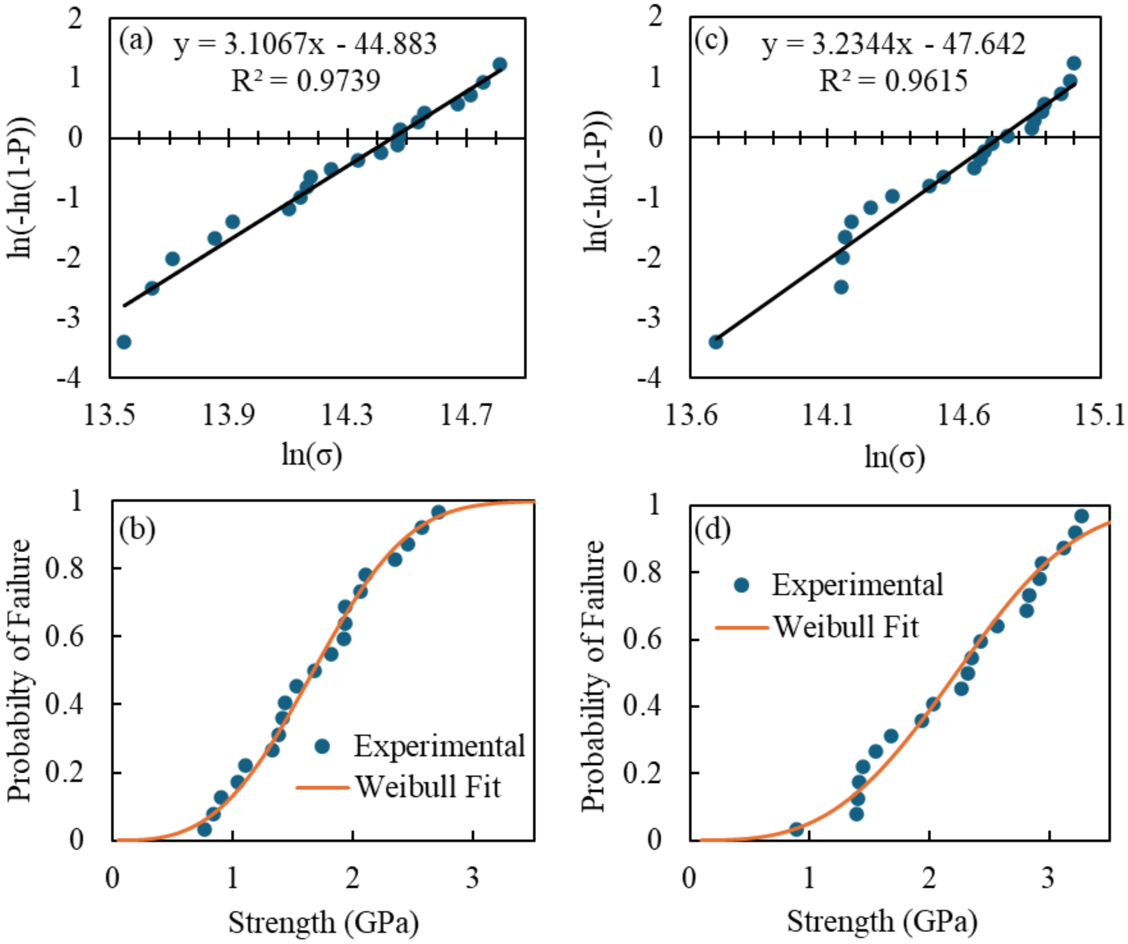

Figure 34. Linear fittings in Weibull coordinates used to calculate shape parameters for the a) radial CF and the c) random CF with the Weibull fit compared to the experimental data for the b) radial CF and the d) random CF

Consequently, these microstructures were characterized to establish structure/property relationships. The Raman maps of the random CF are displayed in **Figure 35**. Raman analysis provides information on the graphitic structure of the CF and can be used to estimate crystal sizes and their orientation parallel to the laser direction [166]. The most common method for analyzing the CF Raman spectra is studying the peak intensity ratio of the D and G bands, I_D/I_G (**Figure 35**a) [131,167,168]. A clear, uniform I_D/I_G was found, concluding that no differences were present between the core and shell of the fiber and that the crystal structure was uniform across the cross-section. The average value of I_D/I_G was found to be 1.26, with a standard deviation of 0.13. Given the long and even oxidation, as previously shown, paired with the slow ramp rate used during carbonization, uniformity with a low standard deviation was the expected result [125].

The ratio of the D and G peak widths (**Figure 35**b) and positions (**Figure 35**c) were also plotted, as previous works have shown that these parameters also provide insight into the CF carbon structure, such as defects and strain dependencies [6,169]. The widths of the two bands tend to have the most significant statistical deviation given the fitting procedure. Therefore, some variation is expected. The average ratio of the peak widths was 1.25, with a standard deviation of 0.34. The deviation in this ratio is roughly 3x that of the intensity ratio; however, the randomness of the peak width ratio throughout the fiber still indicates uniformity in the CF microstructure across its cross-section. The ratio of the peak positions also confirms this, as it is the least affected by the fitting procedure. Here, the ratio of the peak positions was found to be 0.85 on average, with a standard deviation of 0.002. As expected, the deviation of the peak positions is significantly smaller than those found in the peak widths and intensities. All in all, no significant differences in the crystal size and orientation across the CF cross-section were found. This was the same case for the radial CF Raman maps.

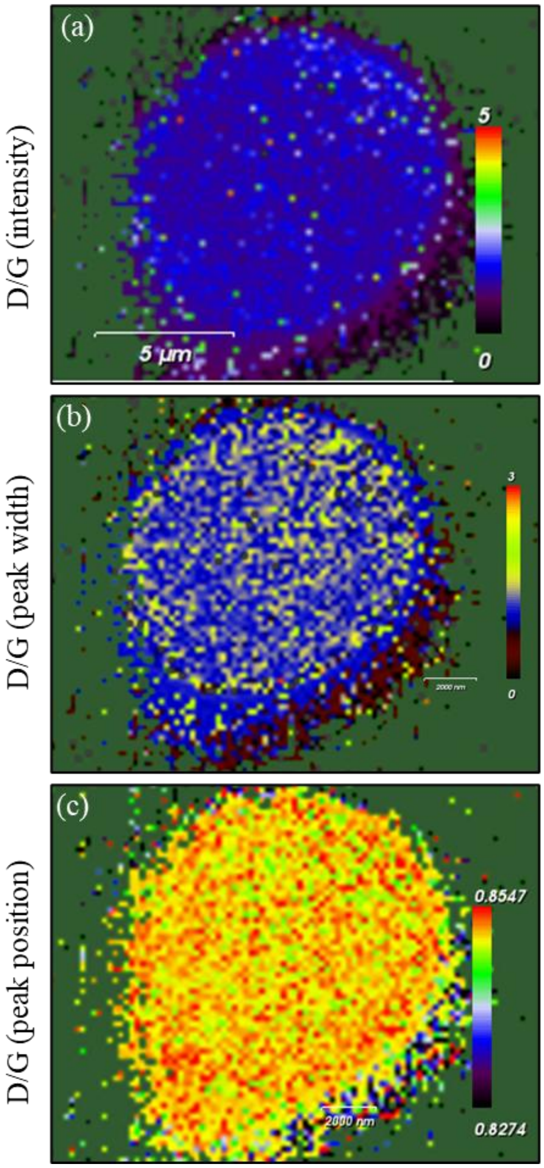

Figure 35. Raman mapping of a random CF cross section showing the ratio of D and G bands: a) intensities, b) peak widths, and c) peak positions

The average I_D/I_G and FWHM(G) for both the radial and random CF were calculated and listed in **Table 10**. Using these values and Equation Error! Reference source not found. and Equation Error! Reference source not found., values for L_a were estimated and listed in **Table 10**. Equation Error! Reference source not found. utilizes the I_D/I_G and estimated L_a to 3.70 nm and 3.49 nm for the radial and random CF, respectively. These values are greater than 2 nm, stating that the TK equation is valid. However, the constant value used in the calculations was for a 514.5 nm laser, which forces an underestimation of the crystallite size since these experiments were run with a 532 nm laser, and the constant value for this wavelength has not yet been determined. The L_a values calculated from Equation Error! Reference source not found. are 10.6 nm and 12.7 nm for the radial and random CF, respectively. These estimated values are much larger, but this method does not rely on a wavelength-dependent constant, leading to a more reliable conclusion. Both results were compared to the calculated values using WAXD.

Table 10. Raman parameters for radial and random CF with calculated La values

	I_D/I_G	L_a (nm) **Error! Reference source not found.**	FWHM(G)	L_a (nm) **Error! Reference source not found.**
Radial	1.19 ± .21	3.70 ± .65	54.4 ± 7.4	10.6 ± 1.4
Random	1.26 ± .13	3.49 ± .36	47.8 ± 6.5	12.7 ± 1.7

WAXD was utilized to estimate the crystallite sizes and their orientation along the fiber axis. The 2-dimensional intensity plots are presented in **Figure 36**ab for the random and radial CF, respectively. Utilizing these plots, the 1-dimensional trace plots in the meridional direction (**Figure 36**c) and equatorial direction (**Figure 36**d) were plotted. The 1-dimensional trace plots were used to find the crystal peaks and the parameters of these peaks. Although powdered samples (40-50 μm) are commonly used for WAXD analysis due to the high reproducibility of results and simplicity in experimental set up [170], collecting WAXD patterns from long, oriented bundles of CF has many advantages. Due to the configuration of the bundles, parameters such as crystallite orientation and crystallite lengths in specific directions can be estimated. This important orientational information is lost when the samples are in powder form. Additionally, the structural characterizations change depending on the breadth of grinding and method utilized due to a breakdown in the crystals over time and an increase in amorphous carbons present [171]. Lastly, the benefit of performing WAXD on an entire CF bundle is that the fibers can be retrieved and mechanically tested post processing, thus developing a better correlation of the effects the crystallographic properties on the CF tensile properties.

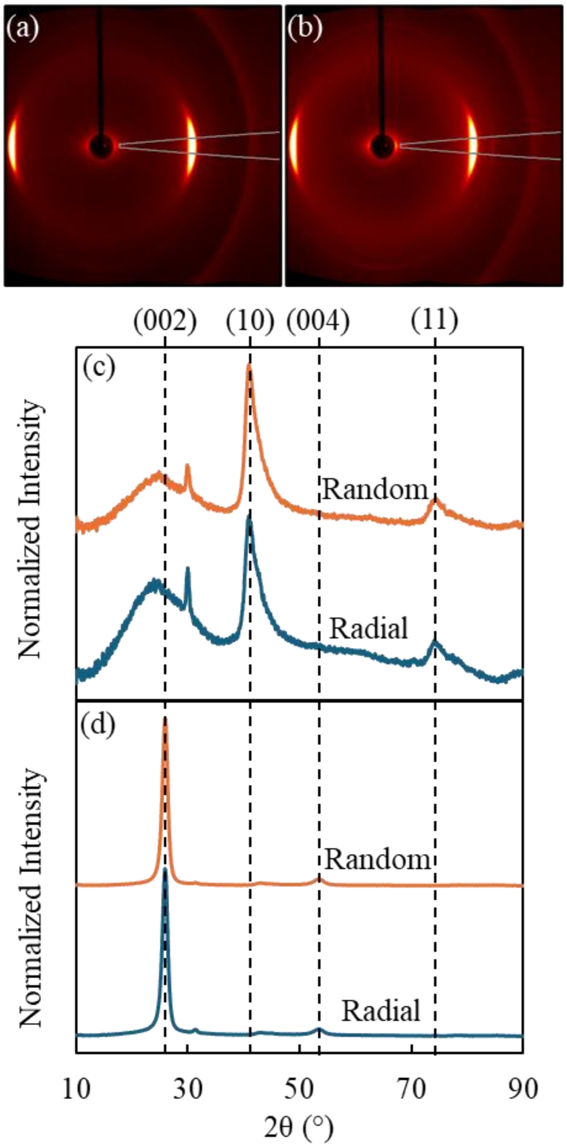

Figure 36. 2-D WAXD plots with equatorial integration region shown for the a) random and b) radial CF. The 1-D trace plots were graphed in the c) meridional and d) equatorial directions. The intensities are normalized to the maximum value for their respective 1D trace plot

Using Scherrer's Equation **(3)** and Bragg's Law **(4)**, the interlayer spacings (d_{hkl}) and the average crystallite sizes ($L_{a\|}$and $L_{c\perp}$) were calculated (**Table 11**). It was not possible to calculate $L_{a\perp}$and $L_{c\|}$ as the (10) intensity in the equatorial plot and the (002) intensity in the meridional plot were not intense enough to fit with any reliable accuracy. Therefore, $L_{a\|}$and $L_{c\perp}$ will be referred to as $L_a$and L_c for the rest of the manuscript. The interlayer spacing in the fiber axis direction (c) and the interatomic distance in the perpendicular direction (a) are identical for the radial and random CF, while the crystallite sizes vary. This equivalence leads to the conclusion that the final HTT determines the interlayer and interatomic distances, not the mesoscopic texture of the fiber.

The radial CF crystallites are slightly thicker in the fiber direction. However, the difference is only 0.8 Å, less than the interlayer distance d_{002} (3.43 Å), making the difference between the samples statistically negligible, indicating that the texture does not significantly impact crystallite stacking. However, the difference between L_a values is 7.5 Å. This is equivalent to 3-4 times the interatomic distance d_{10}. This significant difference shows that the radial and random microstructures influence crystallite growth.

It was also found that the radial and random microstructures affect the orientation of the crystallites. By calculating Herman's orientation factor, f_{002}, using Equation **(5)** and Equation **(6)**, it can be seen that the random CF is slightly more oriented about the fiber axis. This is slightly surprising given that the radial CF is produced through increased shear forces, which should provide more axial alignment. However, crystallites with smaller dimensions in the perpendicular direction may be more prone to misorientation.

Table 11. Crystallite parameters generated from WAXD 1-dimensional trace plots, using Scherrer's Equation and Bragg's Law

	d_{002} (Å)	L_c (nm)	d_{10} (Å)	L_a (nm)	f_{002}
Radial	3.43 ± .01	7.27 ± .41	2.11 ± .01	5.94 ± .20	0.82 ± .01
Random	3.43 ± .01	7.19 ± .40	2.11 ± .01	6.69 ± .24	0.86 ± .01

Due to the high electron density contrast between possible scatters, pores, or crystallite density fluctuations, and all other material phases that can be present in the fibers, the SAXS data is dominated by the presence of such scatters and can be utilized to assess their sizes in the radial and random CF. The SAXS 2-dimensional plots are shown in **Figure 37**ab. While a completely symmetric plot was expected, given the parallel configuration, some asymmetry can be seen. This asymmetry is due to experimental limitations, specifically dealing with the inability to have zero sample tilt. While limited, any sample tilt will be visible in SAXS, especially due to the increased distance between the sample and detector compared to WAXD. Azimuthal integration for the entire breadth of the scatter was completed. The azimuthal data was then utilized to create cross-section Guinier plots, shown in **Figure 37**c, to estimate the radius of gyration, R_g, and diameter of the scatterers, d, for both CF.

The linear fit was generated for the cross-section Guinier plots of the radial and random CF, and the R_g for each was estimated to be 1.5 nm and 1.7 nm, respectively (7). The fit was within the Guinier region, making further analysis possible without the increased error associated with exceeding the Guinier limit. Assuming a circular cross-section of the scatter given the parallel beam orientation with the long axis of the fiber, the diameter of the scatter was estimated using Equation **(8)**. For the radial CF, the estimated average diameter of a scatterer was 3.8 (±0.4) nm, and the random CF average estimated scatter diameter was 4.6 (±0.5) nm. Literature comparison is less direct as these are the first reported values calculated using SAXS in a parallel configuration.

Li et al. studied features of various CF using SAXS in the perpendicular orientation but calculated the diameters for the scatter in the parallel and perpendicular directions [172]. The short axis they calculated should be comparable to the diameters calculated here with a parallel orientation. Li et al. found a perpendicular diameter ranging from 1.9 nm to 6.3 nm using a Debye fitting procedure. The results reported using a parallel configuration fall within that range and are on equivalent length scales to the L_a values estimated using Raman and WAXD. Therefore, the authors find that SAXS completed in the parallel orientation can be used successfully to determine information about the scatters' length scales perpendicular to the fiber axis while removing noise from larger structures along the fiber axis.

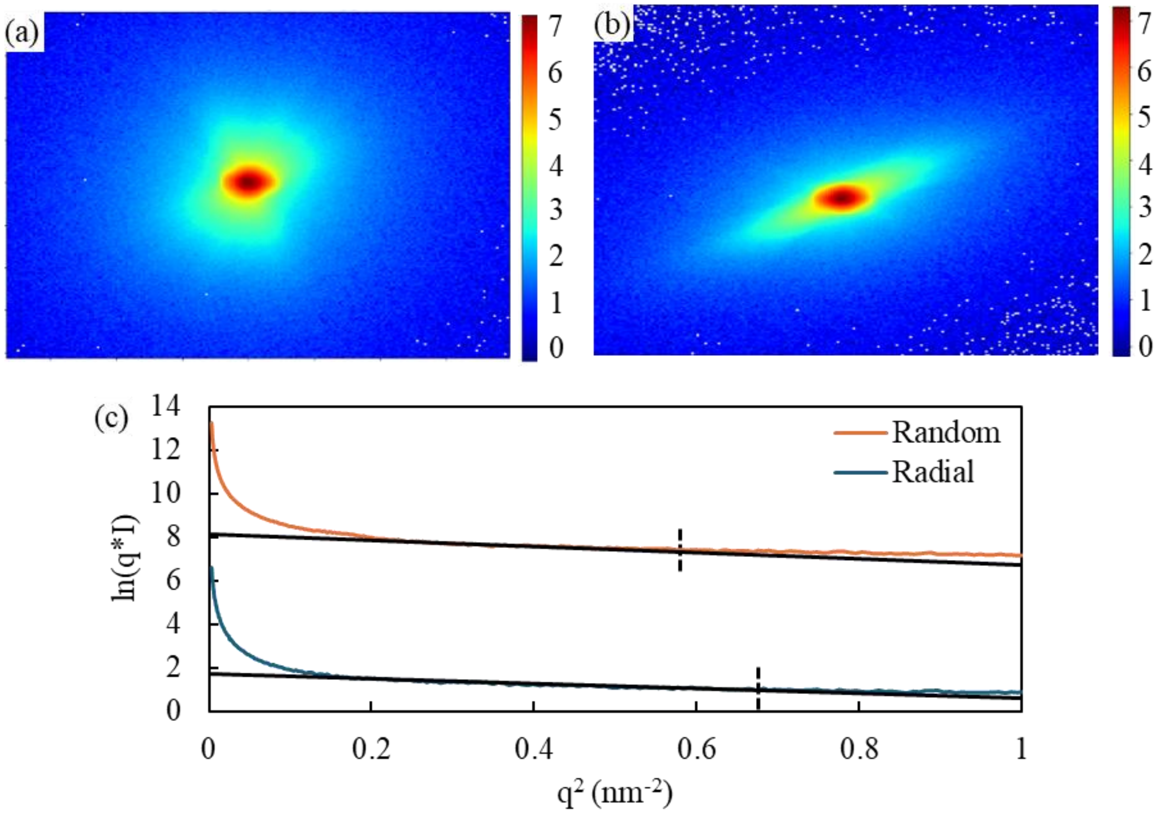

Figure 37. 2-dimensional SAXS plots of the (a) random and (b) radial CF. A 1-dimensional azimuthal trace plot was generated from Φ = 0° to Φ = 360° for both CF and was used to calculate

the (c) cross-section Guinier plot for both. The black lines show the linear fitting, while the vertical dashed lines represent the Guinier limit for the respective scattering plot

In addition to SAXS, TEM is a powerful tool for studying the microstructure of semicrystalline materials, as it enables a direct visual inspection of the microstructural features. TEM images and selected area electron diffraction (SAED) of the longitudinal section of the radial CF (**Figure 38**abc) and the random CF (**Figure 38**def) were completed. **Figure 38**ad shows the standard bright field TEM image of the radial and random CF. Both show the fiber axis oriented left to right and the electron diffraction pattern in the top right. Using this diffraction method, a selected area aperture was used to isolate the diffraction patterns at different fiber positions. **Figure 38**be shows only crystallites with orientation in (002) direction, and **Figure 38**cf shows only crystallites with orientation in (10) direction. When observing the (10) diffraction intensities, small clusters of bright spots scatter throughout both the radial and random CF. This was unexpected and is most likely due to contamination in both samples and a strong crystalline (10) diffraction pattern. More notably, however, the radial CF showed a distinct core when the (002) diffraction intensity was isolated, as displayed in **Figure 38**b. This core-shell structure was not present in the random CF.

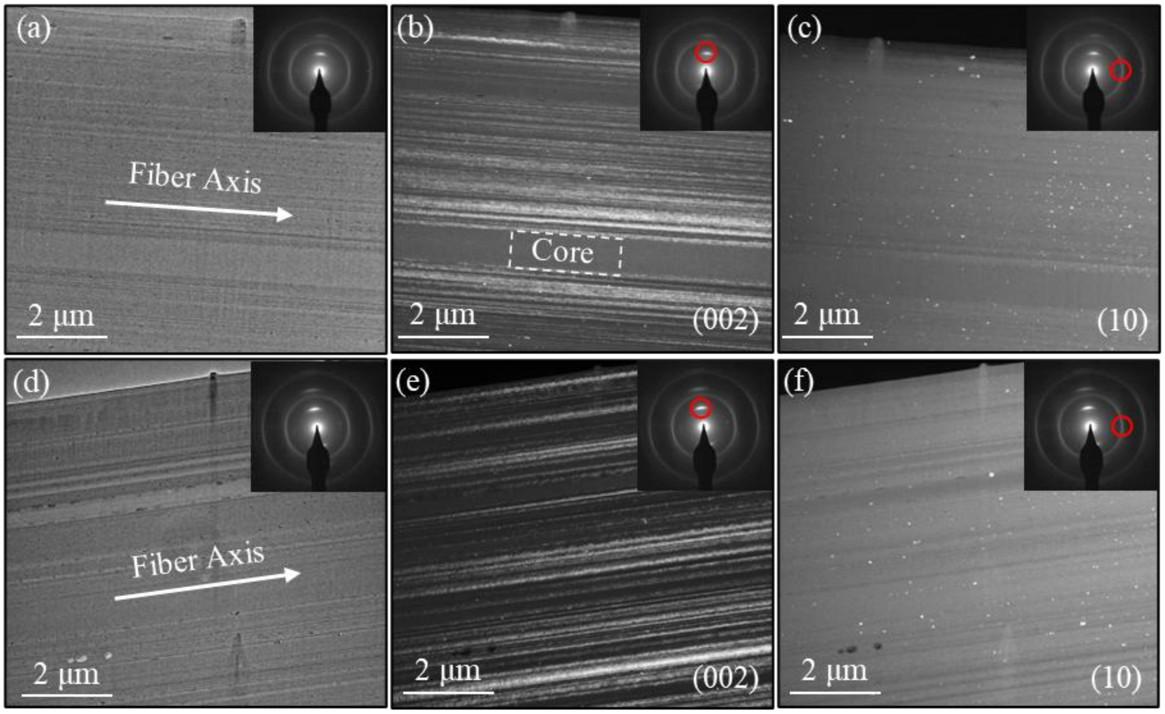

Figure 38. TEM image and SAED of the a) radial CF and the d) random CF. Using a selected area aperture, the (002) plane intensity was isolated and imaged for the b) radial CF and e) random CF, and the (100) plan was isolated and imaged for the c) radial CF and the f) random CF

More detailed TEM images were taken after discovering a core-shell structure in the radial CF sample. The magnification was increased from 3300x to 27kx and focused on the transition core/shell structure (**Figure 39**a). This image showed a clear difference in the crystallite structure depending on location. A further increase in magnification to 230kx allowed for individual analysis of the core and shell regions at the atomic level. **Figure 39**bc shows the TEM images of the radial CF's shell at crystallite length scales. The crystallites show a high orientation with the fiber axis [172]. On the contrary, the crystallites in the core region shown in **Figure 39**de lack orientation and are visually smaller. One reason for this core-shell development lies in the mesostructure of the CF, as a radial pattern forces different growth at the shell as compared to the core. As the graphitic sheets converge in the center, or core, of the CF they have less mobility due to structural constraints. Therefore, the crystallites in the core are unable to grow and expand at the rate as compared to the shell. This congested growth would produce smaller crystallites with less orientation as evidenced in **Table 11**.

To further emphasize the impact of the core-shell structure, FFT images of the HRTEM shown in **Figure 39**bd were produced and presented in **Figure 40**. It should be noted that the FFT images were produced with a horizontal fiber alignment as compared to the vertical alignment used in WAXD, thus creating a similar diffraction pattern but rotated 90°. The FFT of the radial CF shell (**Figure 40**a) presents a standard pattern expected for CF [155]. The (002) plane possesses a clear orientation in the equatorial direction (vertical for this fiber alignment as compared to **Figure 36**a) with a narrow width corresponding to larger crystallites. Meanwhile, the FFT of the core of the radial CF, **Figure 40**b, echoes a pattern similar to that found in unoriented crystalline carbon. The rings are symmetrical around the center, insinuating no preferred alignment of crystallites, and the width of the rings is broader, meaning the crystallites are smaller than those found in the shell. This core region, while it is only 800 nm in diameter, explains the decrease in average L_a and f_{002} as compared to the random CF.

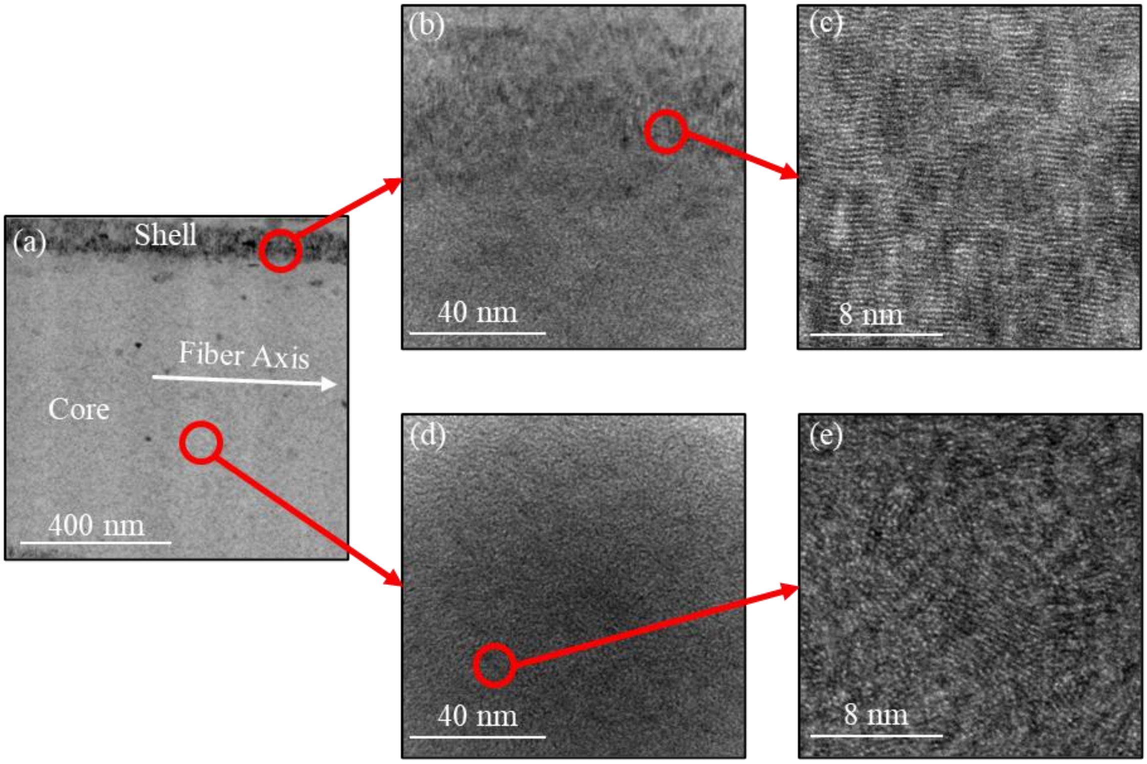

Figure 39. TEM image of the a) core-shell in the radial CF sample. HRTEM images of the shell (b and c) and the core (d and e). The HRTEM of the shell presents well-ordered graphitic crystallites oriented in the fiber axis direction while the core is crystalline, but the crystallites are smaller and unordered

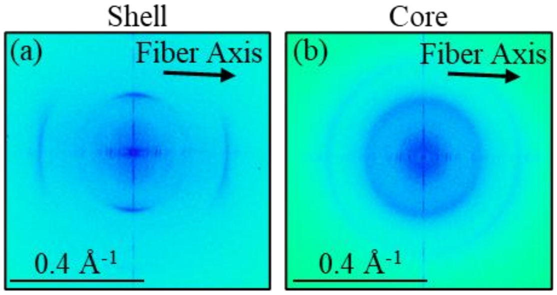

Figure 40. FFT of the HRTEM images of the radial CF's a) shell and b) core. The pattern for the shell shows a clear orientation expected for CF, while the core presents with rings similar to amorphous carbon, demonstrating a lack of order

As seen in **Figure 38**def, the random CF did not have the same core-shell structure and was instead homogeneous in structure across the longitudinal cross-section. Further magnification was also done for this sample to examine if the crystallites were well-ordered, as predicted by WAXD. They are shown in **Figure 41**. The crystallites formed large sheets which are all parallel in the fiber direction, along with some slight waviness to them, as explained by f_{002} not being equal to 1. Overall, the TEM of the random CF sample showed a well-ordered structure, which indeed correlates with their high mechanical performance.

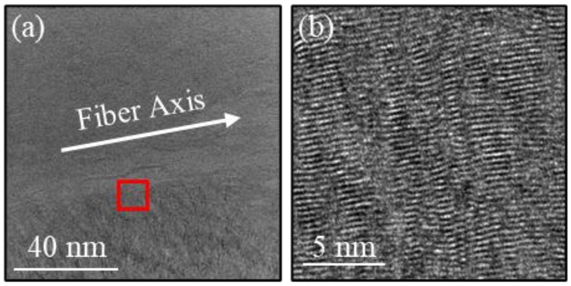

Figure 41. HRTEM of the a) random CF and b) its crystal structure. HRTEM shows that the graphitic crystallites are well-ordered and oriented in the fiber direction

Further examination of the contaminants discovered in **Figure 38**cf was also completed. With the high intensity shown by these contaminants when the (10) plane was isolated, it was known that they were highly crystalline, as shown in **Figure 42**ab, and noncarbon. TEM high-angle annular dark-field (HAADF) was selected and used with a larger viewing area (**Figure 42**c). Using ImageJ, the long and short axes of some of the contaminants, mainly the larger ones, were measured with the long axis found to average 280 (±20) nm and the short axis averaged 55 (±10) nm. HAADF combined with EELS enables elemental analysis of the sample, as shown in **Figure 38**de, using overlays. The presence of sulfur was unsurprising, given that the mesophase pitch feedstock contains sulfur. Typically, the sulfur off-gases during carbonization, but the presence of calcium enabled it to bond and form an ionic salt. Calcium sulfide (CaS) is a compound that crystallizes, explaining the structure observed, and it possesses a melting temperature of 2525 °C, meaning that it cannot be removed at standard carbonization temperatures [173]. The presence of CaS also explains the unknown peaks found at 2θ~32°in the WAXD meridional trace plots [174]. The calcium came from residuals on the extrusion equipment as it was not present in the pitch as delivered. To limit this problem, the CF would need to be produced in an environment that significantly limits the amount of calcium and other non-carbon elements from contaminating the pitch precursor.

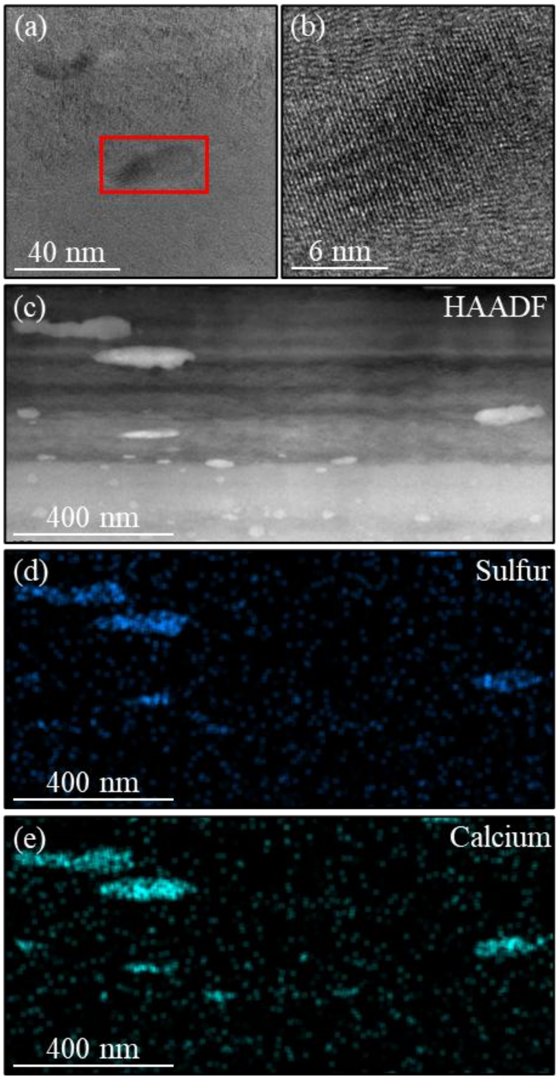

Figure 42. HRTEM of the a) contamination particle and of the b) contamination's crystal structure. Utilizing c) HAADF, elemental mapping was completed, and the overlays of d) Sulfur and e) Calcium show that the particles are made of a mixture of the two elements

Given the prevalence of contaminants, the Griffith's Theory can be applied to understand the increase of strength that may be achievable should the CF be reproduced contaminant-free. Griffith's Theory outlines that as the critical flaw size decreases, the estimated tensile strength of the CF increases [175]:

$$\sigma_f = \sqrt{\frac{EG}{\pi a}} \tag{9}$$

Where σ_f is the tensile strength at fracture, E is the measured modulus from **Table 9**, and γ is the surface energy. For CF, the assumption that no plastic deformation occurs is valid, and the total fraction energy equals double the surface energy [128]. The surface energy of CF can be calculated by equation **(10):**

$$2\gamma_{CF} = 2\gamma_G \frac{\rho_{CF}}{\rho_G} \langle \cos{(\emptyset)} \rangle \tag{10}$$

Where γ_G is the thermodynamic surface energy of graphite crystal (4.8 J/m^2), ρ_{CF} is the density of the CF (assumed to be 1800 kg/m^3), ρ_G is the density of a graphite crystal (2265 kg/m^3), and $\langle \cos{(\emptyset)} \rangle$ is the average cosine of the crystallite orientation previously determined using WAXD and calculating Herman's orientation factor.

Figure 43 shows the plot of the Griffith's Theory predicted tensile strength of the CF against the critical flaw size ranging from 10-500 nm with the average experimental tensile strength for both the random and radial CF shown with solid dots. Using Equation **(9)**, the critical flaw size for both CF can be backed out using the average tensile strength values of 200 nm for the radial CF and 133 nm for the random CF. The critical flaw size direction is perpendicular to the fiber, and therefore, the calculated flaw size for both CF was larger than the measured contaminants in **Figure 42**c, 55 (±10) nm. Given the randomness of these defects' locations and the very limited area probed by TEM, it is coherent to assume larger contaminants exist. If the CF were produced in a way that limited their average critical flaw size to those recorded in the literature (18-66 nm) [176], the tensile strength of both samples would exceed 3 GPa and possibly reach 4 GPa.

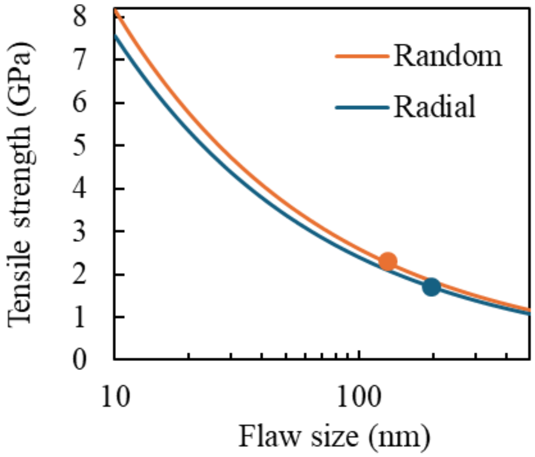

Figure 43. Griffith's theory predicted tensile strength with filled circles representing the experimental strength and dotted lines representing the average defect size according to SAXS

It is important to note that Griffith's Theory does not perfectly represent the strengths that could be reached, as it typically results in overestimating tensile strength [177]. Also, it is unclear what effects the core-shell structure in the radial CF has on the mechanical properties. The Griffith-Irwin relationship is, however, an acceptable method for examining the potential the random CF could have regarding their tensile strength, given that they are uniform in their structure, as evidenced by TEM **(Figure 38**d) and Raman (**Figure 35**).

4. Conclusion

Two types of CF were produced using the same feedstock, mesophase pitch. The first set of CF (sample 1) was produced with a "standard" cylindrical entry nozzle and no disruption filter, resulting in a typical radial microstructure (radial CF). The second set of CF (sample 2) was produced using a conical entry and a disruption filter to decrease the applied shear stress and breakdown of any developed microstructure, which is thus referred to as random CF. Both types of CF were mechanically tested, and it was found that the tensile strength of the radial CF was 1.67 GPa as compared to 2.23 GPa for the random CF. Weibull analysis was performed better to compare the tensile strengths of the two CF given their slightly different diameters, and it was found that the radial samples had a predicted tensile strength of 1.79 GPa when their diameters were scaled down to those of the random CF. Therefore, it was determined that the difference in the tensile strengths was due to differences in the microstructures.

To further examine the effects of the different microstructures, Raman mapping was completed on the cross-section of the random and radial CF and revealed that carbonization resulted in a uniform, crystalline material. WAXD was then used to determine the parameters of the crystallites present in the CF, and the radial and random CF possessed identical interlayer spacing, interatomic spacing, and L_c, but different values for L_a. L_a of the radial CF was found to be smaller, thus showing the influence spinning has on the basal plane size. To the authors' knowledge, the SAXS experiments conducted with the beam parallel to the fiber are reported for the first time. Using an azimuthal integration and cross-section Guinier plots, the average diameter of the scattering cross-sections was calculated and determined to be on the same length scale as L_a, showing the validity of this method. The parallel scan benefits lie in removing noise generated by long-range-oriented effects along the fiber axis, allowing for improved analysis in the transverse direction. Future work examining graphitized fibers with significantly larger crystal length scales could greatly benefit from implementing parallel scans.

TEM showed the presence of a core-shell structure for the radial samples, with the core consisting of smaller and less oriented crystallites. FFT of the core and shell images were generated and showed the orientation present in the shell and lack of preferred ordering in the core, thus confirming the decrease in L_a shown in WAXD. TEM also showed the presence of contaminants identified through EELS as CaS, which were expected to have negatively impacted the tensile strength of the CF, given their size. Griffith's Theory was examined was examined to predict the strength of the CF if the contaminants were removed or decreased in size. If the CF could be produced so that the largest contaminants were the same size as the average critical flaw sizes found in literature, the radial and random CF tensile strengths could reach 3 GPa and above.

Chapter 5: Influence of oxygen uptake on pitch carbon fiber

1. Introduction

In this work, mesophase pitch precursor fibers were oxidized to various weight percentage increases (1 wt%, 3.5 wt%, 5 wt%, 7.5 wt%) at different temperatures (260°C, 280°C, 290°C). A weight increase percentage is usually taken as a metric for bulk fiber stabilization, and, from a simplistic standpoint, can be used as a measure of how much oxygen is present in the fiber. The stabilization procedures were first performed in-situ using a combined DSC and TGA. The TGA measurement was used to determine time required at a specific temperature to achieve a specific oxygen weight percentage increase (1 wt%, 3.5 wt%, 5 wt%, 7.5 wt%). Following this, fiber bundles were stabilized under the same conditions and then carbonized up to 1000°C in a nitrogen atmosphere. The carbonized fiber filaments for each stabilization temperature and time were then tested for tensile performance. Micrographs of the CF filament fracture surfaces were then acquired. Conclusions were drawn regarding oxygen weight uptake percentage, stabilization temperature, stabilization time, fiber microstructure, and mechanical properties.

2. Experimental Methods

2.1. Material Manufacturing

The mesophase pitch used in this study was purchased from MotorCarbon LLC and was used as received, with an approximate mesophase volume fraction of 70% [140]. The pitch was ground and loaded into a pressure-driven batch extruder at room temperature. The pitch was kept in an inert (nitrogen) atmosphere while the extruder climbed to a target temperature of 315 °C. Once the target temperature was reached, the mesophase pitch was extruded to produce precursor fibers using a high pressure and were wound onto a roller. The extruder was equipped with a mesh filter to remove any large particulates remaining in the pitch precursor from the extrudable material to limit defects in the resulting fibers. This method provided precursor fibers with diameters ranging from 18-22 microns.

2.2. Switch-gas experiments

TGA was performed on a TA instruments Q600 SDT thermogravimetric analyzers. Oxygen uptake and carbon yield of the fibers were determined through switch-gas experiments with two steps: (i) an oxidation step and (ii) a carbonization step. An example of the switch-gas experiment is shown in **Figure 44**. The experiment started in an air atmosphere allowing the sample to oxidize. The amount of oxygen uptake was measured during the oxidation phase by the increase in fiber weight over time. Three different oxidation temperatures (260, 280, and 290°C) were used for this study all with a ramp rate of 10°C/min. Each sample was run for different amounts of hold times for each oxidation temperature to achieve different oxygen uptake percentages of 1 wt%, 3.5 wt%, 5 wt%, and 7.5 wt%. The full time from ramp up to cool down for an oxidation run was labelled the stabilization time.

In order to remove any residual free oxygen, the samples were then cooled to room temperature before proceeding with the carbonization step. The gas was switched to nitrogen and the samples were heated to 1000°C with a ramp rate of 10°C/min. Carbon yield was then recorded using the final fiber weight compared with the precursor fiber weight before oxidation.

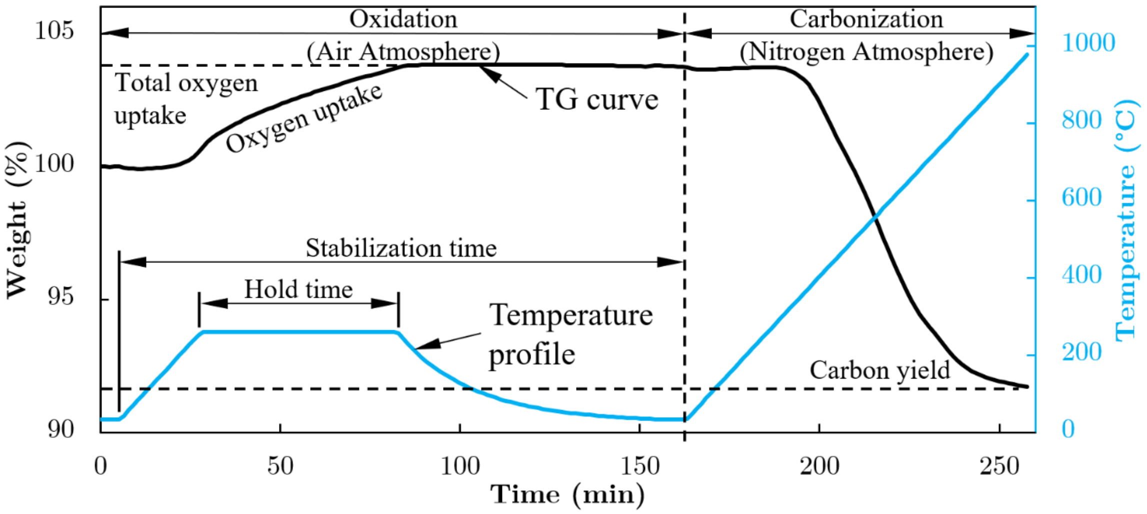

Figure 44. Typical experimental data (260°C oxidation temperature with 55 minute hold) for switch-gas experiments labeled with critical data

2.3. Characterization techniques

Upon completion of the switch-gas experiments, 80 mm length sections of the precursor fibers were cut and rerun with the same oxidation and carbonization procedures in a tube furnace. Similar to the switch-gas experiments, the oxidation was run in the tube furnace with an air environment and the carbonization was run in a Nitrogen environment. The longer length sections allowed for further characterization of the fibers' microstructural properties, the oxygen's penetration into the fiber, and the carbon fibers' mechanical performance.

Characterization of oxidation process

Thermal analysis of the carbonization process was performed by a combined DSC and TGA using a Netzsch STA 449 F1 Jupiter. This instrument was used because it allowed for capturing the DSC of the oxidized material up to the carbonization temperature of 1000°C. This instrument, which includes TGA, also served as an additional check that the longer (80 mm) section of fibers validated TGA results from the switch-gas experiments. The DSC/TGA samples were heated to

1000°C with a heating and cooling rate of 10°C/min with the samples under an inert (argon) atmosphere.

Images of the oxidized fiber cross sections were taken using a FEI Quanta 650 SEM at 5 kV. The oxidized fibers were gold sputtered using a Cressington Sputter Coater to avoid charging during imaging. EDS was used to determine the amount of oxygen and carbon in the cross section (**Figure 45**a). An oxygen profile over the cross-section's diameter is presented in **Figure 45**bc for a precursor and oxidized fiber, respectively. Measurements of oxygen and carbon content were made every 0.05 μm across the diameter and then normalized to the size of the fiber to keep measurements consistent. Composition of the elements was performed with Aztec software with a "QuantLine" scan.

The precursor fiber contained a uniform concentration of oxygen of approximately 2.2 wt% across the fiber diameter. This amount of oxygen was used as a baseline and removed from the oxidized fibers to determine the amount of oxygen taken up by the fiber during stabilization. The oxidized fiber had a non-constant oxygen profile. **Figure 45**c shows an example of the oxygen profile detected by EDS plotted against a normalized diameter. The plots showed a characteristic parabolic shape, and a curve fit was utilized to find the best fit with the data using Equation **(11)**:

$$f(x) = ax^2 + b \tag{11}$$

where a, b are the fitting parameters and x is the normalized diameter. This equation was derived to ensure that the curve was symmetric about the center ($x = 0$) of the normalized diameter and that $\partial f / \partial x$ is zero at the center. Integrating Equation **(11)** over the interval of -0.5 to 0.5 and dividing by the domain distance is used to determine the average of the oxygen profile. This operation results in the average in terms of fitting parameters to be:

$$ox_{avg} = a/12 + b \quad \textbf{(12)}$$

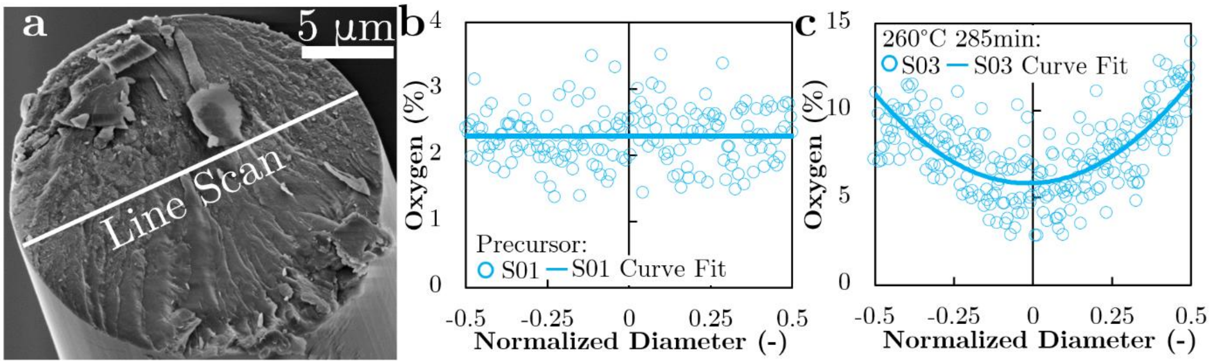

Figure 45. (a) SEM of the oxidized fiber cross section showing the region selected for a line scan and the EDS measurements resulting from the line scan over the normalized diameter of (b) a precursor fiber and (c) an example oxidized fiber ran at 260°C for 285 minutes with precursor fiber oxygen content removed

Characterization of carbonization process

Images of the CF cross sections were also taken using a FEI Quanta 650 SEM. The cross-sectional images came from the fracture surfaces of the CFs following tensile testing. To avoid damaging the surfaces, the post-test single-filament tests were gold sputtered using a Cressington Sputter Coater and then imaged with SEM.

Single-fiber tensile tests were performed using an MTS Nano Bionix UTM nanoscale tensile tester, which has a maximum load capacity of 500 mN and 150 mm of extension. All tests were run according to ASTM standard D3822-014 at a gauge length of 10 mm and a strain rate of 2e-4 s^{-1}. The average strength, modulus, and strain of the CFs were determined by the measured stress-strain curves.

3. Results and Discussion

3.1. Oxidation

TGA of the oxidation portion from the switch-gas experiments revealed the amount of time needed to oxidize the pitch precursor fibers for different amounts of oxygen uptake and the results are presented in **Figure 46**. The weight gained during the oxidation process is primarily attributed to the attachment of oxygen-containing functional groups onto the pitch structure and therefore we attributed any weight gain to this attachment [71]. As expected, there are differences in hold times required to reach a specific amount of oxygen uptake for the different temperatures. To reach an oxygen uptake of 3.5 wt% (**Figure 46**a), the time spent at the specified temperature varies for each chosen oxidation point. However, for higher oxygen uptakes (**Figure 46**bc), the hold time for 280°C and 290°C become indistinguishable. The reason these become indistinguishable may be due to additional reactions reducing weight, such as decarboxylation [89]. However, the weight continually increases. This indicated that these additional reactions occur at a slower rate as compared to the oxidation process.

The 260°C samples, as expected, take longer to produce the same amount of oxygen uptake than higher temperatures. This can be attributed to the diffusion rate's relationship to temperature and the rate of diffusion of oxygen into the fiber being lower for the lower temperature. **Figure 46**d presents the amount of hold time needed to reach certain oxidation percentages. The hold time can be estimated by a parabolic shape and shows the dramatic increase in time needed to reach higher oxygen percentages with the 260°C sample needing slightly more than double (2.19x) the hold time to reach the same 7.5% oxygen percentage as compared to the higher temperature samples. Increasing the hold time has a direct increase in the full stabilization time.

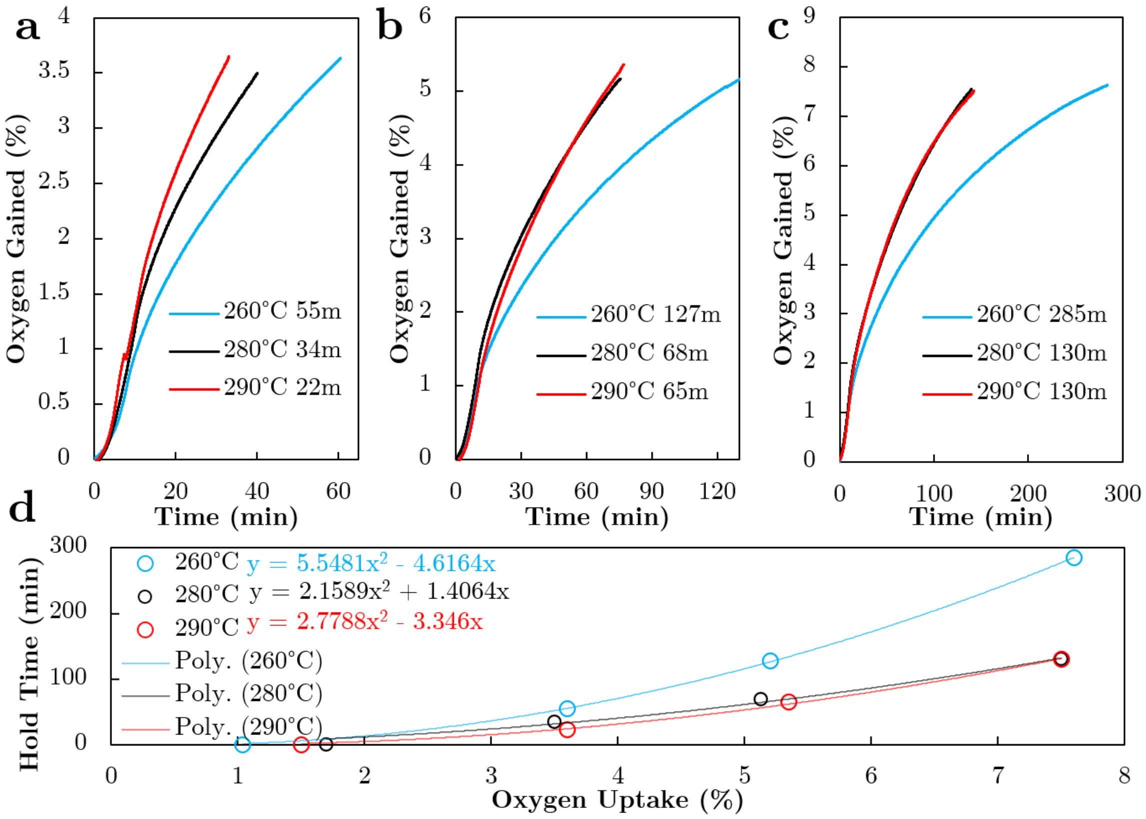

Figure 46. Oxygen uptake weight gained versus time for the (a) 3%, (b) 5%, and (c) 7% uptake percentages. (d) is hold time needed for oxygen uptake percentage at different oxidation temperatures

Figure 47 shows the temperature profiles and the DTG analysis curves. It is clear that different temperatures change the diffusion rate of oxygen uptake with higher temperatures increasing the diffusion rate and lower temperatures decreasing diffusion rate. This trend holds for both the low (~3% oxygen uptake) and medium (~5% oxygen uptake) hold times (**Figure 47**ab). However, as similarly shown in **Figure 46**c, the 290°C oxidation temperature did not differ from the 280°C for the largest oxygen uptake wt%. The DTG curves reveal that the oxidation reaction starts at 150°C and follows a decaying rate with increasing time. Since the rate is not constant, it could mean that the chemical bonding with oxygen slows the rate of diffusion into the center of the fiber.

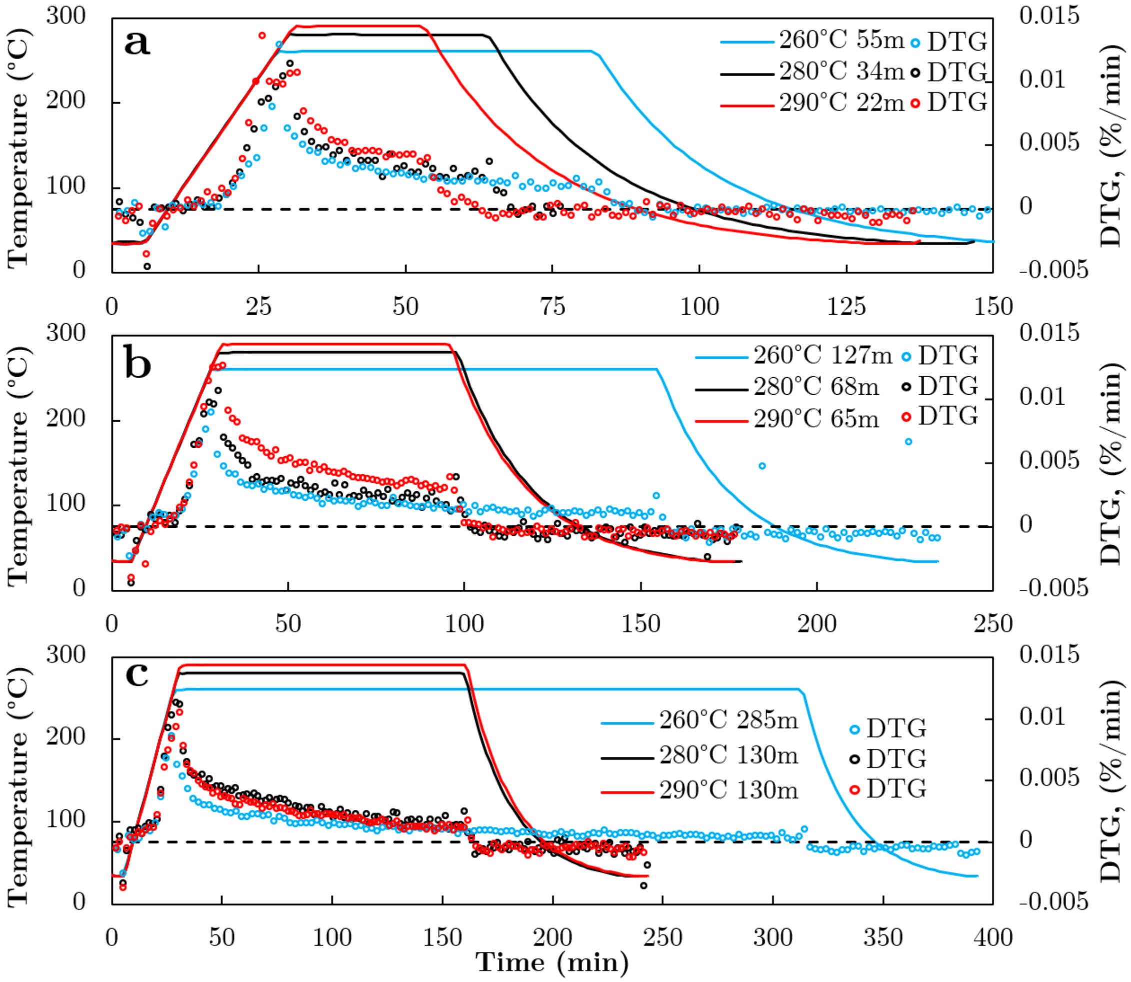

Figure 47. Temperature profile and DTG curve for (a) 3%, (b) 5%, and (c) 7% oxygen uptake

The amount of oxygen absorbed by the fibers during oxidation is shown in **Figure 48**. EDS showed that the amount of oxygen absorbed by the fibers is similar to the amount of weight gained during the TGA experiments for stable oxidation temperatures of 260 °C and 280 °C (**Figure 48**abcd). As the hold times are extended to promote more oxidation, the differences between the 290°C samples compared to the other two temperatures increases. This supports the results seen from **Figure 46** and is indicative of another reaction happening that is removing weight as well as adding oxygen to the fibers. Lim and Yeo note in [89] that excess oxidation causes more unstable O=O bonding rather than stable C-O and C=O bonds. We attribute the 290°C to be causing excessive oxidation rapidly changing the bonds that are being formed. The C-O and C=O bonds are necessary as they limit fusibility and interrupt the compact crystal structure after carbonization. The large variation in **Figure 48**a may be due to the small amount of oxygen penetration and the accuracy of the EDS at this level of oxygen percentage.

The normalized oxygen uptakes are shown in **Figure 48**efgh. The results show that as hold time increases, the variation across the fiber cross section becomes less pronounced and approaches an equilibrium. This indicates that hold time in air is needed to stop fibers from fusing during carbonization. This study suggests at least 2% oxygen uptake is needed at the center of the fiber to stop fibers fusing together. We suspect that longer hold times at similar temperatures allow for further diffusion of oxygen into the fiber structure, however, the parabolic shapes of oxygen profiles could not be avoided at any of the temperatures or hold times tested here. Longer hold times at even lower temperatures could lead to a more homogenous radial oxygen distribution profile in the fiber. This could potentially increase mechanical properties and eliminate the formation of an under-oxidized fiber core as indicated by other work with atmospheric pressure [91].

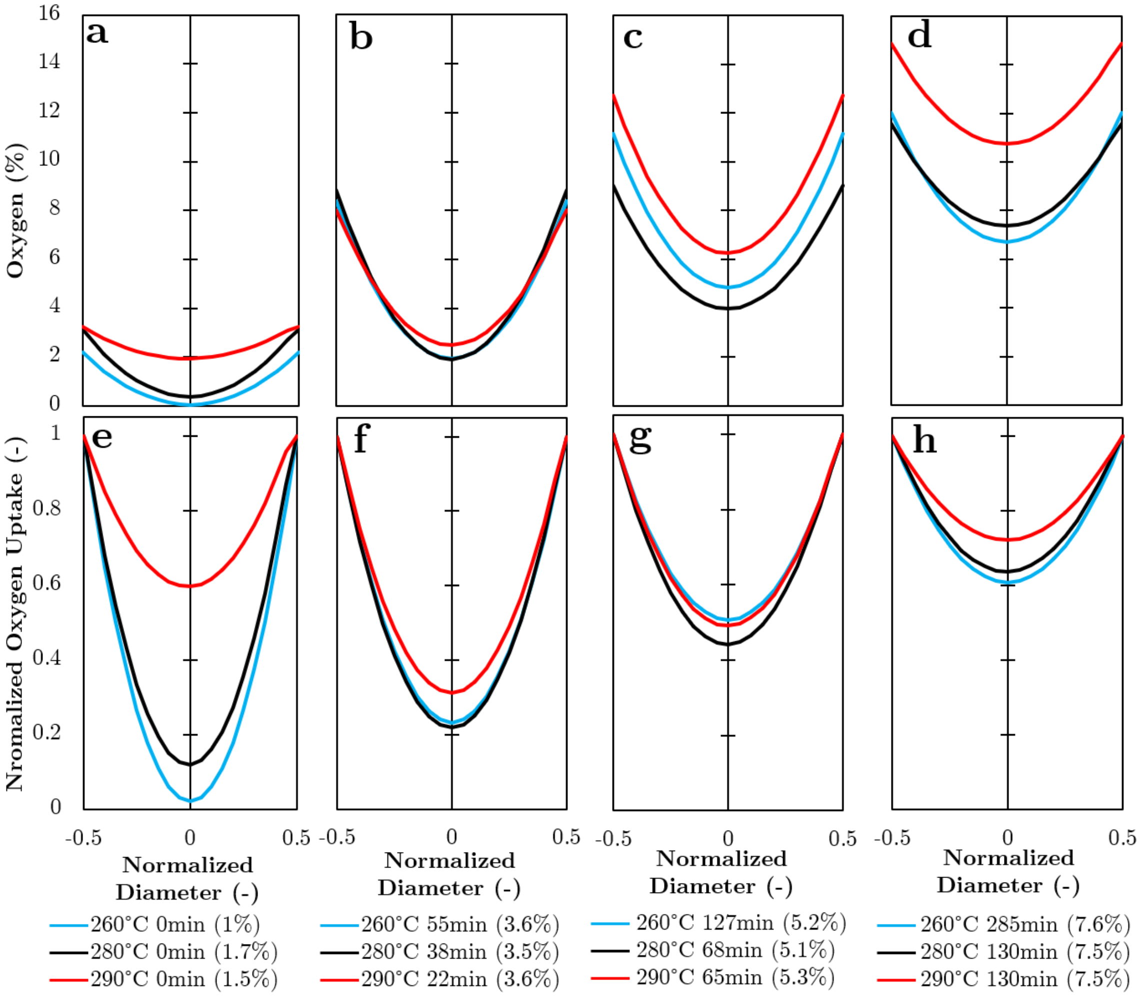

Figure 48. Fitting of oxygen profile from EDS scans grouped by average oxygen uptake where (a) is ~1-2%, (b) is ~3.6%, (c) is ~5.2% and (d) is ~7.5% and the normalized oxygen uptake for (e) is ~1-2%, (f) is ~3.6%, (g) is ~5.2% and(h) is ~7.5%

Table 12 presents the results of the fitting parameters to the EDS oxygen profiles, the oxygen weight at the center (ox_c) & edge (ox_{edge}), the average oxygen weight content from EDS, the average oxidation weight from the TGA experiments, and the percent difference between these oxidation percentages. The difference between the average oxygen percentage from TGA and EDS are compared. Oxidation at low temperatures have relatively smaller differences between the two techniques for the 260°C and 280°C samples than the 290°C samples. The fact that all oxygen percentage from EDS is markedly higher than the TGA results indicates that some of the reaction can be removing weight during the sample while still adhering oxygen to the sample. The weight gain as suggested by previous researchers [90] can be gaseous CO and CO_2 reducing weight in the precursor fiber during oxidation. The discrepancy between 260°C and 290°C suggests that there are competing reactions of oxygen uptake and degradation, which is intensified at higher temperatures.

Table 12. Oxidation fitting parameters by sample with oxidation averages from calculated from fitting parameters and a comparison of the percent difference between EDS calculated oxidation average and TGA weight uptake averages

Sample	Fitting Parameters		ox_{edge} (%)	ox_{avg} (%)	% Oxidation TGA	% Difference
	a	b, ox_c (%)				
260°C 0min	8.62	0.05	2.21	0.77	1.0	-23.0
260°C 55min	25.82	1.12	7.57	3.27	3.6	-9.1
260°C 127min	26.62	3.39	10.1	5.61	5.2	7.9
260°C 285min	22.23	5.45	11.0	7.30	7.6	-4.0
280°C 0min	12.50	0.38	3.50	1.42	1.7	-16.5
280°C 38min	29.04	1.92	9.18	4.34	3.5	24.0
280°C 68min	21.67	4.02	9.44	5.83	5.1	14.3
280°C 130min	18.27	7.37	11.9	8.89	7.5	18.5
290°C 0min	6.73	1.94	3.62	2.50	1.5	66.5
290°C 22min	23.52	2.51	8.38	4.47	3.6	24.0
290°C 65min	27.44	6.25	13.1	8.54	5.3	61.1
290°C 130min	18.01	10.74	15.2	12.24	7.5	63.2

Figure 49 presents the ratio of the oxidation at the edge to the center (ox_{edge}/ox_c) plotted against hold time and oxygen uptake. **Figure 49**a shows the relationship with hold time. The ratio of the oxygen at the edge to the center becomes closer to 1 as hold time increases and the fact that this ratio reduces more slowly with temperature. **Figure 49**b shows the same ratio against oxygen uptake. The ratio follows the same trend with increased oxygen uptake brings the center oxygen

uptake closer to the edge oxygen uptake. With more oxygen uptake these ratios become more consistent.

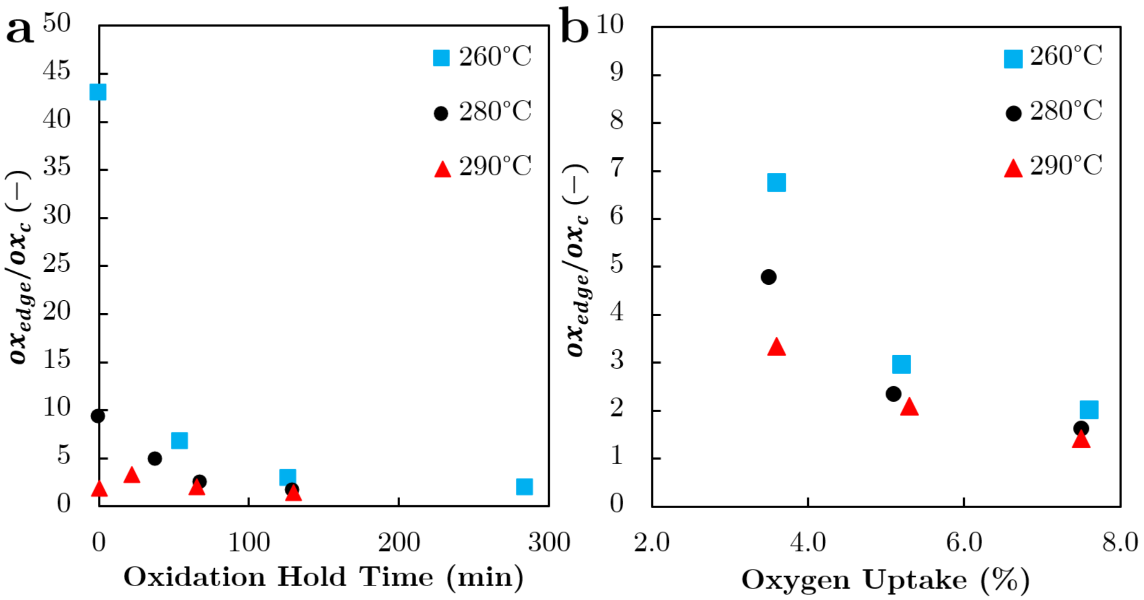

Figure 49. Ratio of oxygen uptake from the edge to the center against (a) hold time and (b) average oxygen uptake

3.2. Carbonization

Figure 50 shows the differential heat flow of the sample during the carbonization process. All samples that were oxidized with a zero-hold time produced similar heat flows. These samples show a crystallization temperature between 300°C and 400°C indicating that the pitch has not been thermally stabilized (**Figure 50**efg). The crystallization reaction temperature changes with increasing oxidation temperature with 260°C starting at 275°C, 280°C starting at 300°C, and 290°C starting at 325°C. Then, approximately around 600°C, the start of a large endothermic reaction begins taking place. This is attributed to melting of the fibers because the fibers were not stabilized enough to maintain their shape leading to fusing. The stabilized fibers with a hold time greater than zero successfully removed the glass transition and the fusing of the sample. The reaction shows a stable heat flow up to the 1000°C carbonization temperature indicating that the transition between a stabilized fiber and fiber that fuses is 1.5% and 3.5% oxygen uptake. As indicated by the oxidized fibers, there is a dramatic improvement in melt stability.

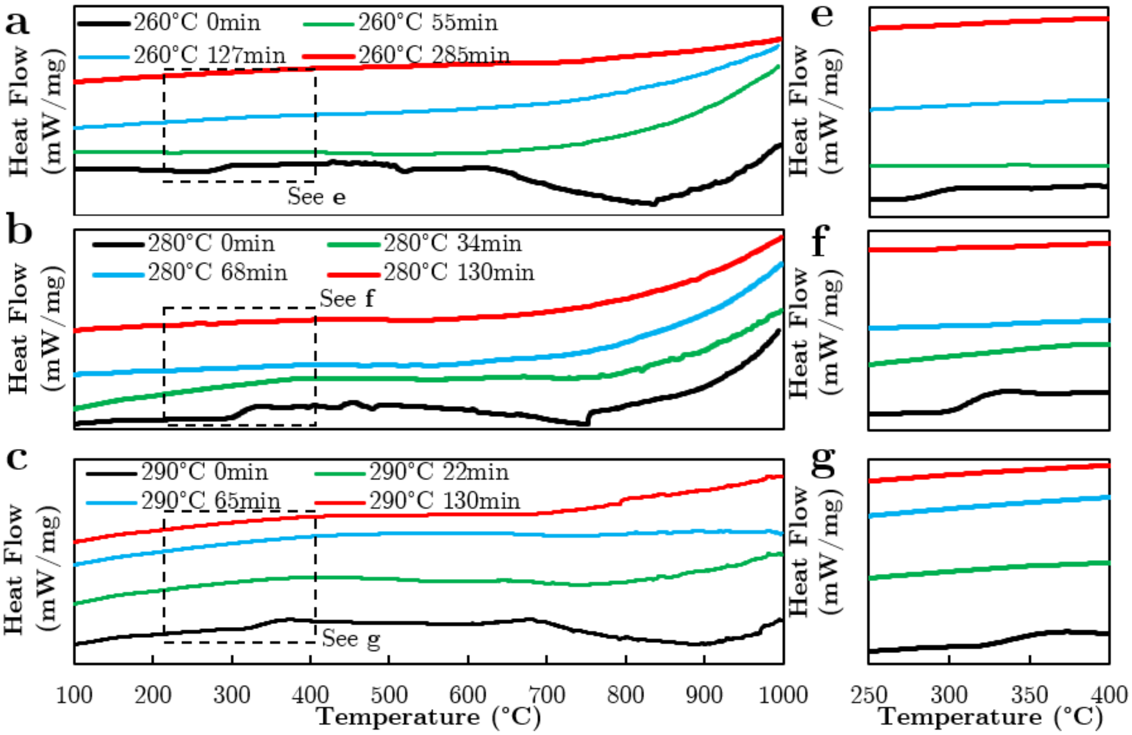

Figure 50. DSC of carbonization process (10°C/min in an argon atmosphere with heat flows shown as Exo up) for the (a) 260°C, (b) 280°C, and (c) 290°C samples. A subset of the DSC shown for the crystallization temperature range of 250°C-400°C for the (d) 260°C, (e) 280°C, and (f) 290°C samples

Figure 51 presents the carbon yield with different oxidation percentages. After normalizing the data to the sample precursor weight, it is clear that increasing oxidation percentages result in a decrease in carbon yields for all temperatures studied here. All samples exhibit similar decreases. However, it is interesting to note that the slopes from the linear trend lines increase in magnitude with temperature. The fiber deteriorates more at higher temperatures with extended oxygen uptake leading to a larger decrease in carbon yield as compared to lower temperatures. It is important to note that while the lowest oxygen uptake produced the highest carbon yield, it also resulted in fused fibers (**Figure 52**ab).

The addition of oxygen uptake did not directly correlate to a reduction in carbon yield. This indicates that not all oxygen introduced into the carbon fiber burnt off at 1000°C. The introduced oxygen is a part of the backbone of the pitch produced carbon fiber.

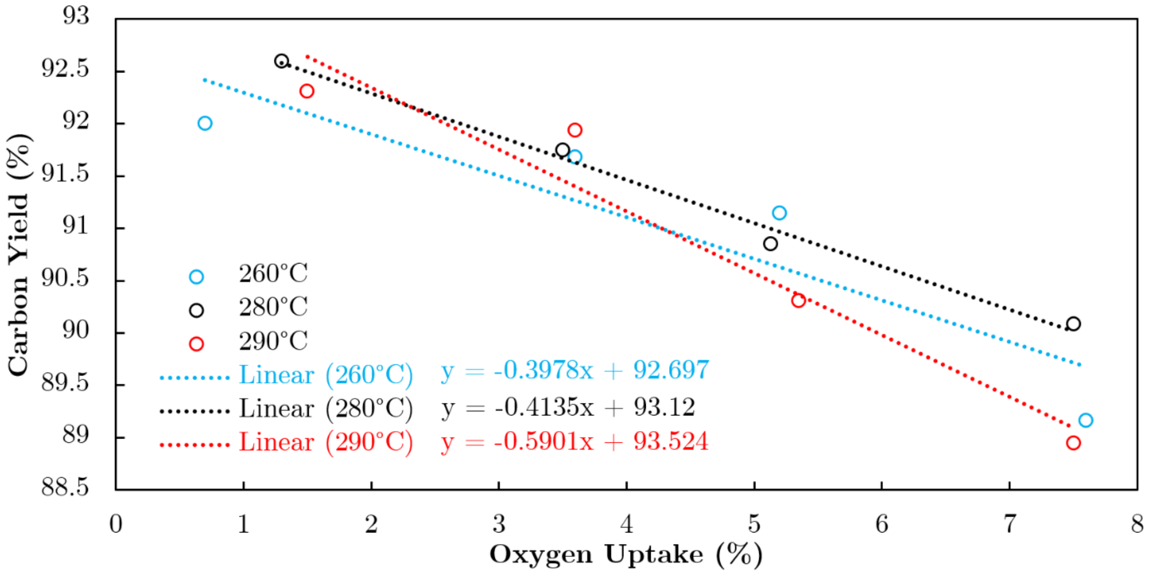

Figure 51. Carbon yield of different oxidation temperature and oxygen uptake percentages

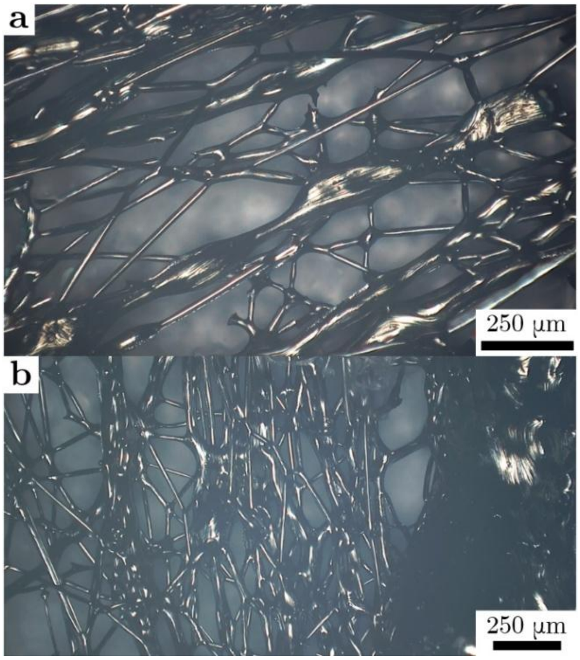

Figure 52. An example of fused carbonized fibers from 280°C no hold samples

Oxidation affects the mechanical properties of the CF. **Figure 53** presents the tensile strength, failure strain, and modulus values based on different oxidation percentages. **Figure 53**a shows different results for all three different oxidation temperatures. The 290°C oxidized fibers decrease tensile strength of the resultant CF with increasing oxidation percentage. The mechanical properties for the carbonized 280°C fibers were consistent regardless of increasing oxygen uptake percentage. The 260°C oxidation temperature showed that there is a higher strength at 5 wt% oxidation and lower. The variability in the 260°C oxidized CF indicates that there is an optimal oxygen uptake for different oxidation temperatures. **Figure 53**b shows the average moduli results for the carbonized fibers. The oxidation temperature revealed decreasing modulus for the 290°C oxidized samples and increasing modulus for 260°C with increasing oxidation time, while the 280°C CFs remained relatively constant. Although 260°C resulted in the highest tensile strength at 5% oxygen uptake, the 260°C samples had the highest standard deviation indicating that the samples are highly variable.

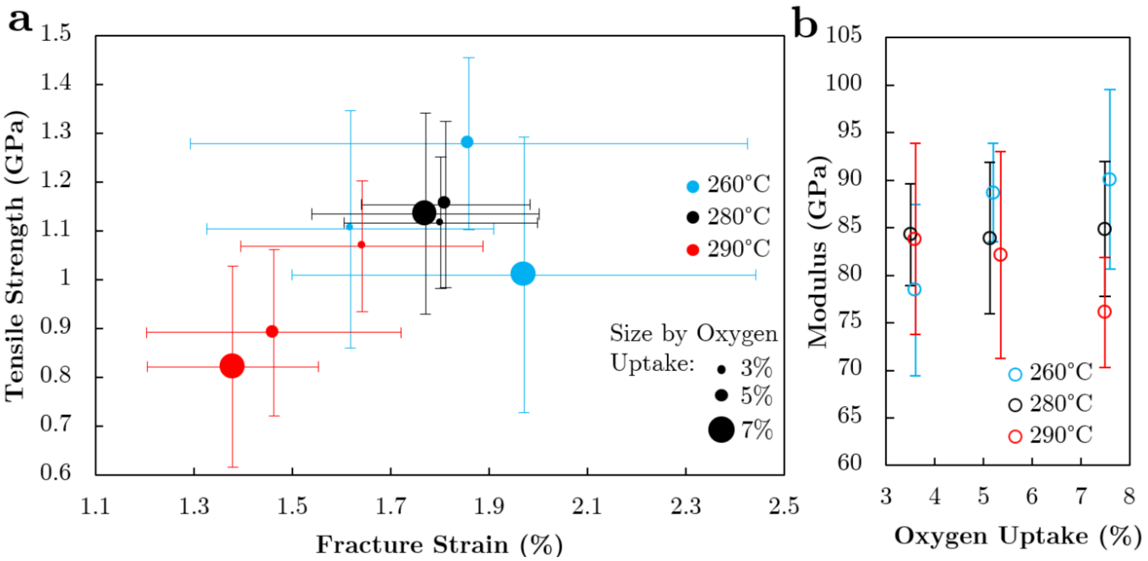

Figure 53. (a) The average of the tensile strength and fracture strain averages based on oxidation percentages and temperature with error bars indicating standard deviation of fracture strain and tensile strength and (b) is the average modulus based on oxygen uptake with error bars indicating standard deviation

Figure 54 presents the SEM images of the carbonized fibers. While typical temperatures of carbonization are 1000°C - 1500°C, 1000°C is a lower carbonization temperature. At 1000°C the microstructure may not be fully developed; however, some trends can be seen. The lower oxidation percentages (**Figure 54**adg) show melted cores due to the low hold times which do not allow oxygen to penetrate the middle of the fibers. The 290°C oxidations (**Figure 54**ghi) all reveal cracks akin to pac-man splits that are likely due to the high oxidation temperature [20]. High oxidation temperatures could lead to over-aggressive thermosetting of the fibers, which yield stress concentrations during the carbonization process. The crack opening starts at the surface and propagates to the center. Therefore, it is concluded that the rapid increase in oxygen diffusion at the surface causes the first crack.

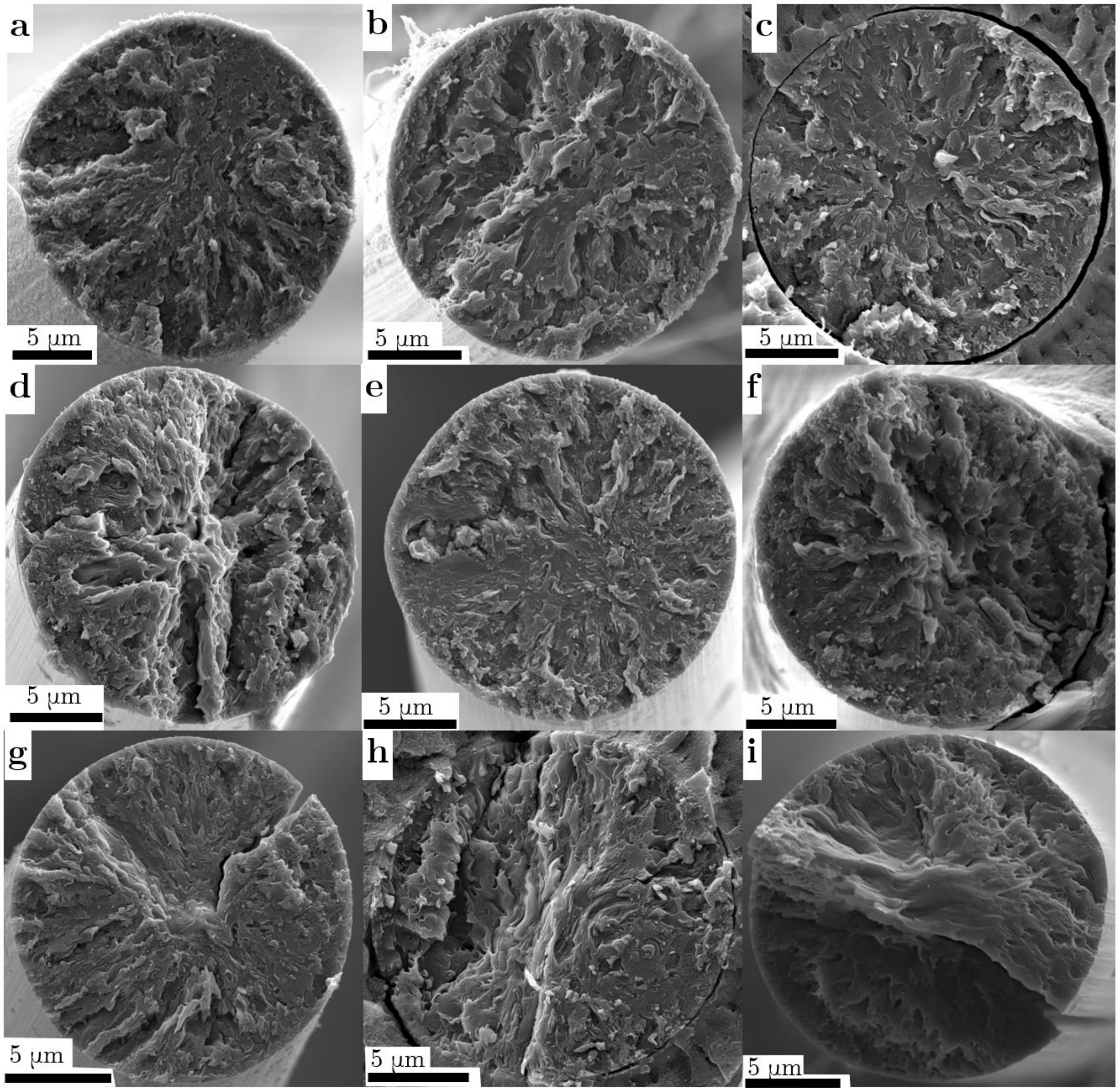

Figure 54. SEM images of carbonized fibers at different oxidation temperatures and oxygen uptake (a) 260°C 3.7%, (b) 260°C 4.6%, (c) 260°C 7.5%, (d) 280°C 3.6%, (e) 280°C 5.2%, (f) 280°C 7.5%, (g) 290°C 3.6%, (h) 290°C 5.4%, and (i) 290°C 7.5%

Oxygen uptake during oxidation has been shown to have a time and temperature dependent effect on the mechanical performance of a CF. The results from this study show that applying oxidation temperatures above 280°C results in deterioration of the microstructure and ensuing mechanical performance with greater effect at longer hold times. In particular, the resulting CFs produced from the 290°C have pac-man splitting like cracking defects in the cross-sections. High oxidation temperatures are potentially providing overly-aggressive oxygen uptake that the thermosetting of the fibers causes stress concentrations. These stress concentrations then build up and during the carbonization process create cracks in the fiber.

The best mechanical performance occurred at 5% oxidation, which is differs from previous reports [1,31,32] that suggest the optimal oxidation percentage is 8%. Therefore, we suspect that the optimal oxidation point is not a universal number, but rather dependent on intrinsic material and processing parameters such as pitch type, diameter of fiber, and spinning conditions, as well as the oxidation cycle in terms of time and temperature.

The consistency of the 280°C mechanical properties shows that the lowest oxidation time may be used without detrimental effects to the mechanical properties. In this regard, a stabilization time of 60 minutes could be used to match properties that had a stabilization time of 156 minutes. This is a large reduction from the 4 hour oxidation previously utilized (as seen in [89]). While treatment at 280°C produced a constant oxygen uptake within this study's test parameters, these tests should be repeated for different fiber types to determine the applicability to a broader set of PAN-CF or MPCF.

4. Conclusion

Mesophase pitch precursor fibers were oxidized to four different oxygen weight percentages at three different temperatures. The TGA measurement was used to determine the time required at a specific temperature to achieve a specific oxygen weight percentage increase and indicated the large effect that temperature has on the diffusion of oxygen into the precursor fiber. The results showed that the lowest oxygen uptake percentage (the no-hold fibers) did not stabilize the fiber enough and resulted in the fibers melting/fusing during carbonization. The highest mechanical strength came from the lowest temperature oxidation of 260°C with a 5% oxygen uptake. Finally, an upper limit of 280°C oxidation temperature is proposed to avoid cracks in the subsequent CFs.

Oxygen uptake as a standalone metric is not sufficient to predict mechanical performance, as time and temperature are important considerations as well. This study compared the pitch CF at relatively similar stabilization states and found for similar oxidation states, the mechanical properties of the resulting CFs are dependent on the stabilization process.

Chapter 6: Tuning microstructure of mesophase pitch carbon fiber by altering the carbonization ramp rate

1. Introduction

This study aims to investigate high ramp rates and the effects this may have on CF microstructure as well as to establish the relationship between ramp rate and CF microstructure. The goal is to inform future efforts in designing the microstructure of the fibers which can be leveraged for specific applications such as EVs, fuel storage, or supercapacitors. Ramp rates were set at 1, 5, 10, 30, and 50 °C/min to 1000 °C from ambient temperature. DSC, TGA, and DTG were utilized to determine the thermal effects of ramp rate on mesophase pitch's microstructure. All fibers were mechanically tested and the results were compared to establish trends between ramp rate and mechanical properties. SEM, Raman spectroscopy, and XRD of the tensile test samples were employed to investigate any microstructure differences resulting from the various ramp rates. Through these investigations, this study aims to tune MPCF microstructure while contributing to ongoing research into the reactions and graphitic growth occurring during carbonization.

2. Experimental Methods

2.1. Materials and Preparation

The mesophase pitch used in this study was purchased from MotorCarbon LLC and used as delivered. According to MotorCarbon, their Meso-C mesophase pitch has a carbon content of 94 to 94.5 wt.%, a coking value in the 89 to 90% range, and an approximate mesophase content of 75%. **Figure 55** shows an optical polarized image of the mesophase pitch that distinguishes the isotropic and anisotropic regions.

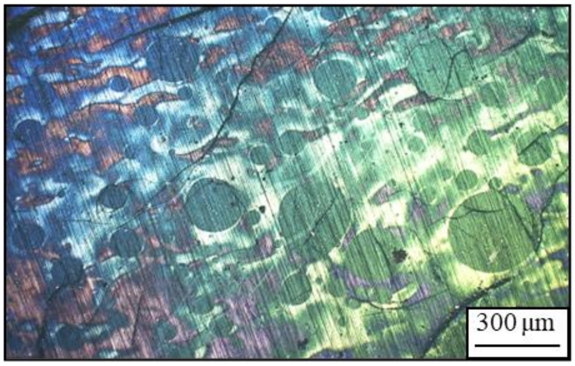

Figure 55. Polarized image of mesophase pitch

The mesophase pitch produces a mosaic-like structure when viewed under polarized light with dark and circular isotropic regions as first described by Brooks and Taylor [37]. By calculating the area of the isotropic circles in **Figure 55**, one can estimate the mesophase region to be around 75% which aligns with the approximation given by MotorCarbon. Following the analysis of the raw mesophase pitch, it was converted into CF through the process outlined in **Figure 1**. The carbonization ramp rate was varied for each sample.

Extrusion was completed using a custom lab-scale batch extruder capable of extruding 20 grams of material per batch. The extruder was flushed with nitrogen after loading the feedstock pitch and positive pressure was maintained inside the melt chamber throughout the entire process to ensure no oxidation took place prior to extrusion. The extruder temperature was set to 310 °C, roughly 50 °C above the material's softening point, and the internal pressure was increased to 200 PSI to extrude the pitch through a custom 100-micron nozzle. The extrudate was cooled over a 60 cm air gap before being taken up on a 15 cm diameter drum at a rate of 700 m/min. The collected fiber was cut from the drum to form a tow of more than 1000 filaments averaging 15 microns in diameter.

The tow was divided into multiple, 7 cm strips of a few hundred filaments for testing. Each section was oxidized at 220 °C for 48 hours. Researchers have shown that successful oxidation can be achieved in as little one hour, but this requires temperatures of 280 °C, which can lead to overoxidation [29, 42]. Therefore, a long duration oxidation was employed to prevent oxidation-induced defects that may obscure the effects of carbonization temperature ramp rate.

2.2. Carbonization

All oxidized fibers were carbonized under an inert environment (argon) at ramp rates of 1, 5, 10, 30, and 50 °C/min from ambient temperature to 1000 °C and were held at this temperature for 30 minutes. This process required the use of two furnaces to accommodate ramp rates ranging from 1 °C/min up to 50 °C/min. A GSL-1500 tube furnace was used for ramp rates of 10 °C/min and less while a Thermolyne 21100 tube furnace was used for all ramp rates greater than 10 °C/min. The temperature profile of each carbonization was recorded to ensure that the target ramp rate was reached and maintained within an acceptable range. Due to oscillations induced by the temperature controllers' responses during heating, the target ramp rate was defined as an average of the ramp rate during heating between 300 and 800 °C, **Figure 56**.

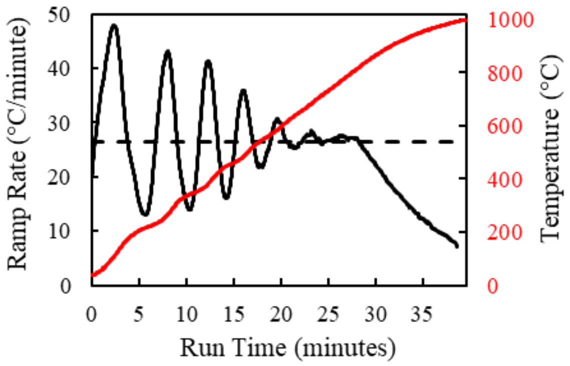

Figure 56. Example of a carbonization thermal history curve showing the furnace temperature (red), the ramp rate (black), and the average ramp rate from 300 to 800 °C (black dashed)

2.3. Characterization Methodology

DSC/TGA/DTG

Thermal analysis of the mesophase pitch powder was performed via DSC and TGA simultaneously using a Netzsch STA 449 F1 Jupiter. The DTG curve was calculated by taking the slope along each data point, and the resulting curve was smoothed using a moving forward average of 20 data points. DSC/TGA was conducted under an inert atmosphere (argon) and the samples were heated to 1000°C from ambient temperature with an initial ramp rate of 10°C/min up to 300°C followed by the sample target ramp rate up to the ultimate carbonization temperature. Samples weighing 10 ± 1 mg were produced from powdered pitch taken from inside the extruder following a spinning trial and oxidized to ensure identical thermal histories between the powder material and the CFs. The resulting DSC curves provided insight into the endothermic and exothermic reactions while the TGA and DTG curves were used to determine the char yield and weight loss regions of the pitch.

Microscopy

Images of the carbon fiber fracture cross sections were taken using an FEI Quanta 650 SEM following single filament tensile testing. The fibers were gold sputtered using a Cressington Sputter Coater to avoid charging during imaging.

Single Filament Tensile Testing

Single-fiber tensile tests were performed using a nanoscale tensile tester (MTS Nano Bionix UTM), which has a maximum load capacity of 500 mN and 150 mm of extension. All tests were performed according to ASTM standard D3822-014 with the gauge length of 10 mm and a strain rate of $2e^{-4}$. The average strength, modulus, and strain of CFs were calculated based on the loaddisplacement curves measured by the machine and the tested fibers' diameter as measured via optical microscopy. An initial diameter measurement was taken using an Olympus BX53 optical microscope with a 50x objective lens and custom image analysis script. This method can lead to slight overestimation of diameters due to edge distortion, so a correction factor was applied based on an average of the fiber diameter of the sample batch. Each batch of CF was mounted vertically and polished according to ASTM standard D4616-95, then imaged using a Hirox scope with a 1000x lens. 100 fibers were randomly selected and measured using ImageJ to get an average diameter. Each tensile sample diameter measurement was then multiplied by a ratio of the average diameter to the sample measured diameter.

Microstructural Characterization

Raman spectroscopy of the CFs were completed using a Renishaw InVia Confocal Raman microscope. Each scan was completed using a 514 nm argon laser in conjunction with a 50x lens. The raw data was baselined and multipeak fit with five Voigt curves which are identified in **Figure 57** [6]. Each peak fit was held at constant center with the intensity and FWHM allowed to vary across samples. The G peak is centered at 1580 cm^{-1} and is associated with E_{2G} symmetry stemming from sp^2 carbon atoms present in the graphitic regions. The D peak is centered at 1350 cm^{-1} and stems from defects such as edges and voids in the graphitic structure [169]. For both of these peaks, the areas were recorded to determine I_D/I_G [166]. Given the inhomogeneity of MPCF often resulting in skin-core structures [178], scans were taken at the surface of the fiber and the center of the cross section using the same polished samples used to calculate the average diameter. Five scans were performed on both the surface and core. The I_D/I_G ratios for each sample were calculated and the averages were then compared resulting in 12 unique data points.

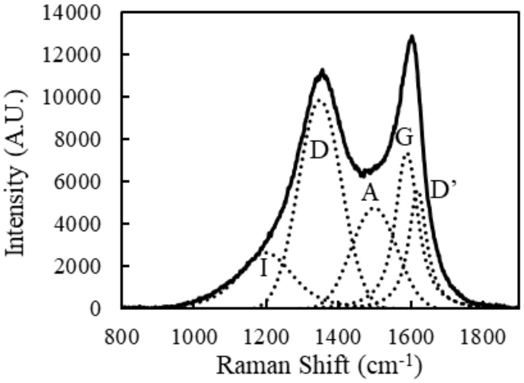

Figure 57. Curve fitting example of the Raman spectra of a CF from this study

XRD was conducted with a Bruker D8 Venture utilizing Cu-Kα radiation at a wavelength of 0.154 nm. Glass capillaries, 1mm in diameter, were used and a baseline scan was completed in air before the capillaries were filled with CF and scanned in the azimuthal direction. Bruker APEX4 software was used to integrate the scans producing a 2θ spread of 10-106°. Crystallite sizes (L_c and L_a) were estimated using Scherrer's Equation Error! Reference source not found. and interplanar spacing (d_{002}) was calculated using Bragg's Law Error! Reference source not found.**)** [56]. For the equations mentioned, λ is the wavelength of the X-rays, k is the shape factor, θ is the center of denoted peak, and n is the diffraction order. For the most consistent results, a standard ruler method was utilized to determine the FWHM of both peaks and the shape factor was set such that "k" is equal to 1 for both L_c and L_a due to the determined value representing an averaged measurement of crystallite sizes [179].

3. Results and Discussion

The DSC curves of the oxidized mesophase pitch powders produced with varying ramp rates are shown in **Figure 58** with an arbitrary offset for clarity. Previous work was completed by Yue et. al. [50] and they showed that mesophase pitch has two DSC features, which can be seen in the

450-600 °C and 600-1100 °C range. Both features were shown to be exothermic in nature regardless of ramp rates while the intensity of the features increased with faster ramp rates. Yue et. al [180] also noted that slower ramp rates, less than 30 °C/min, led to an endothermic shift at higher temperatures and an exothermic process for higher heating rates. It should be noted that these results stem from mesophase pitch which was not first oxidized leading to more intense reactions as compared to the material used in this study. Therefore, both expected features are muted for the two slowest ramp rates, **Figure 58**ab, as they possess the smoothest DSC curves with no distinguishable peaks.

For ramp rates of 10 °C/min and greater (**Figure 58**cde), the expected exothermic reactions can be identified. **Figure 58**c shows an exothermic reaction around 500 °C for the 10 °C/min sample, responsible for crystallization. **Figure 58**d does not show the same exothermic peak at 500 °C, rather, it shows an overall exothermic shift once temperature reaches 300 °C which continues until roughly 800 °C. This was due to some increased crystallization reactions which onset at a lower temperature. The DSC profile produced with a ramp rate of 50 °C/min (**Figure 58**e) is the most active. It contains a similar crystallization onset as the material with a ramp rate of 30 °C/min, but the trend is interrupted as a reaction occurs at 500 °C. This reaction is exothermic in nature and is similar to the reaction shown for 10 °C/min at the same temperature. While these reactions are difficult to identify due to the large range of aromatics and non-carbons in mesophase pitch, a temperature range of 300 to 800 °C can be identified as the most influential thereby indicating bounds for an area of interest.

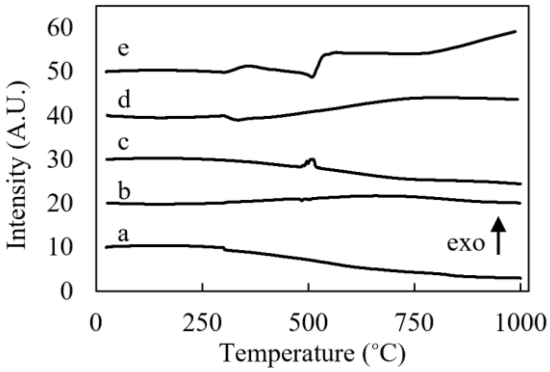

Figure 58. DSC curves of mesophase pitch powder from 25 °C to 1000 °C with varied ramp rates of: (a) 1 °C/min, (b) 5 °C/min, (c) 10 °C/min, (d) 30 °C/min, (e) 50 °C/min

Next, TGA was performed and DTG curves were created to assess the pitch weight loss vs temperature. As shown in **Figure 59**, 300 °C is just before weight loss occurs and weight loss has mostly stabilized by 800 °C. A large weight loss can be seen for 50 °C/min from 800 to 1000 °C but this is attributed to noise induced by the machine in its efforts avoid overshooting while approaching its final temperature. The material was weighed after testing to ensure that weight loss measurements were accurate. Therefore, similar to all the other ramp rates, it is assumed that the material holds steady at 50C/min with only 1-2 wt.% loss from 800 to 1000 °C. The two areas of interest from TGA were weight loss onset and final char yield. As shown in **Figure 59**a, the onset of weight loss is directly tied to the ramp rate with slower ramp rates leading to lower onset temperatures. Slower ramp rates also possess larger final char yields, with the exception of 30 °C/min. While the weight loss onset temperature for 30 °C/min falls between the onset temperatures of 10 and 50 °C/min as expected, a 30 °C/min ramp rate produced the largest char yield compared to all other samples, **Table 13**. Given this unexpected result, the sample was rerun, and an identical result was found.

The DTG curves show at which temperature and what intensity the maximum weight loss occurs at for each ramp rate (**Figure 59**b, **Table 13**). The slowest ramp rate of 1 °C/min has the lowest temperature for maximum weight loss at 439 °C. Similar to weight loss onset temperature, the temperature for maximum weight loss increases as ramp rate increases with the exception of 30 °C/min which had the highest temperature for maximum weight loss. A ramp rate of 30 °C/min also results in a DTG peak with the largest width. This means that carbonization reactions resulting in material loss, or off-gassing, occurred over the largest temperature span for material produced with a 30 °C/min ramp rate. As previously noted, the same material also has the highest char yield. Therefore, the intensity or the amount of off-gassing at any temperature must be small in comparison and this is most clearly seen when comparing to the DTG curve produced with a 50 °C/min ramp rate. A 50 °C/min ramp rate resulted in a maximum weight loss rate of nearly -0.3 %/°C which is roughly three times larger than the maximum weight loss for 30 °C/min. In other words, the material produced with a 50 °C/min ramp rate lost the most weight in the shortest span highlighting the role ramp rate has on mesophase pitch.

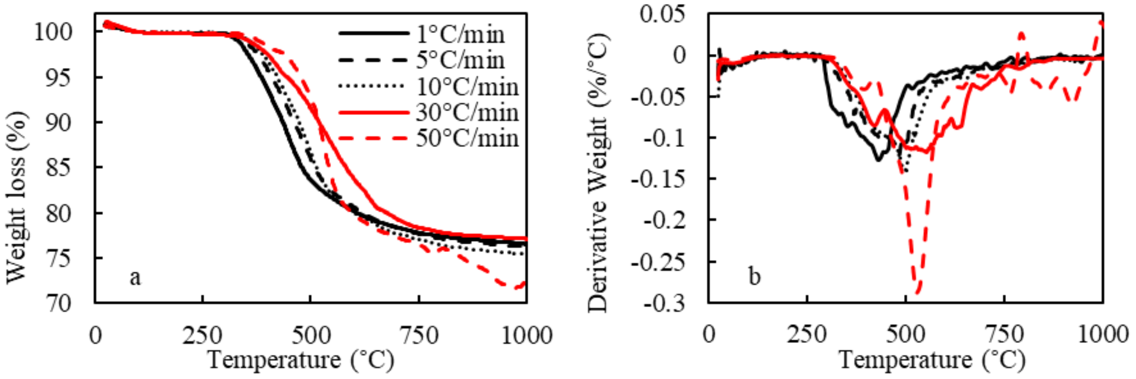

Figure 59. TGA curves of the mesophase pitch powder (a) and the calculated DTG curves (b)

Table 13. List of char yields and the temperature at maximum weight loss for varying ramp rates

Ramp Rate (°C/min)	Char yield at 1000 °C (%)	Temperature of maximum weight loss (°C)
1	75.98	439
5	75.86	483
10	74.82	500
30	76.30	552
50	73.92	527

Following thermal analysis, these carbonization ramp rates were used to make CF for microstructural and mechanical characterization. The carbonization profile for each ramp rate is shown in **Figure 60**. As previously mentioned, the furnace has a difficult time controlling the temperature at higher ramp rates and this creates an oscillation. From the TGA and DTG curves, the most important range for evaluation lies between 300 and 800 °C. Therefore, the average ramp rate in this region was calculated. As expected, the Thermolyne F21100 furnace responsible for two highest ramp rates, **Figure 60**ab, had the largest error between average ramp rate and set point. All CFs produced via the GSL-1500 tube furnace experienced ramp rate oscillation during carbonization as well, but the average ramp rate for the temperature range of interest was much closer to the set point.

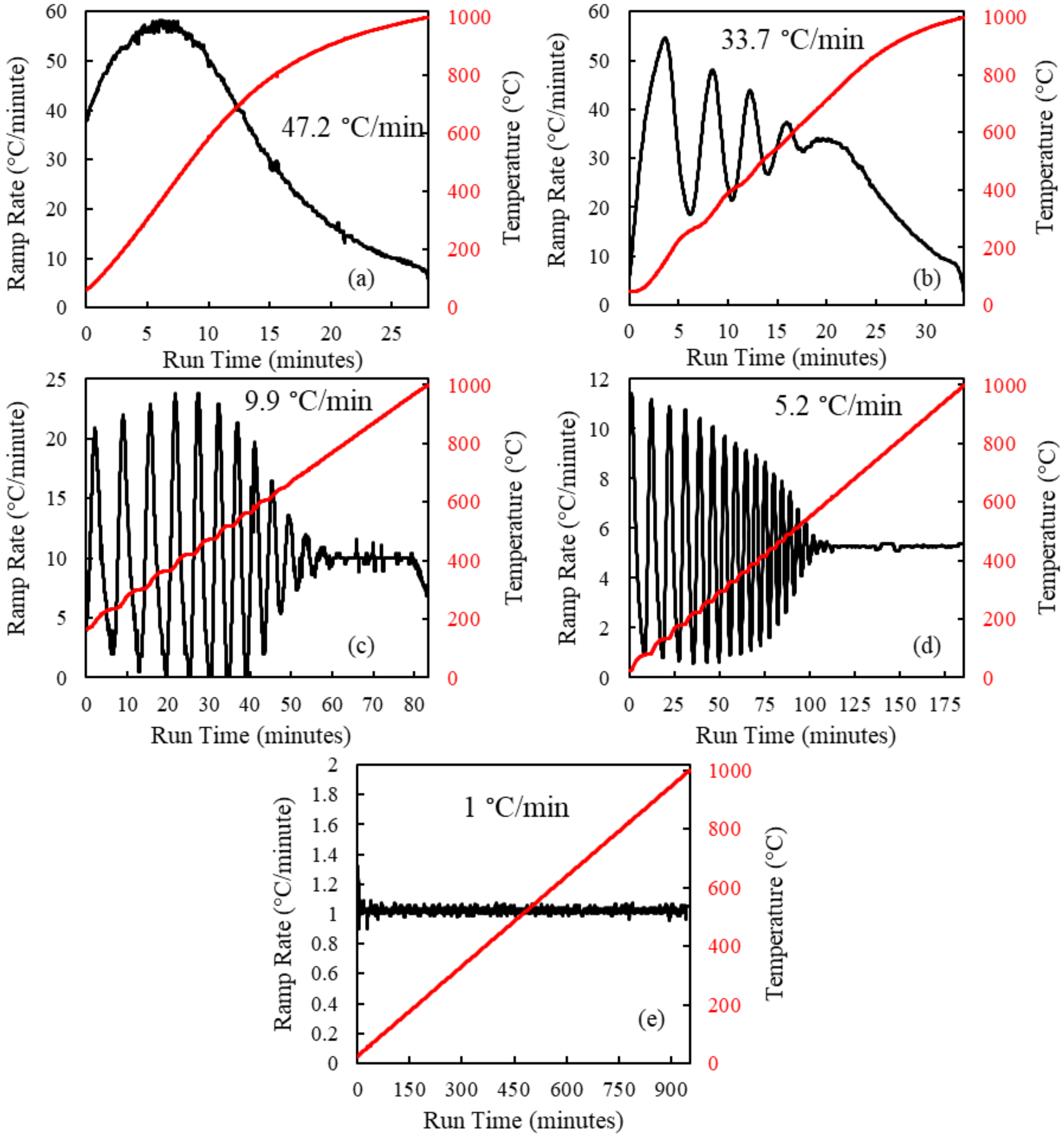

Figure 60. CF thermal history from ramp rates of: (a) 50 °C/min, (b) 30 °C/min, (c) 10 °C/min, (d) 5 °C/min, (e) 1 °C/min. Measured temperature is presented in red with calculated ramp rate presented in black and average ramp rate from 300 to 800 °C is included

Each carbonization run shown in **Figure 60** produced high quality CFs capable of being handled and tensile tested. The results of the single filament tests are listed in **Table 14** and the strength and modulus values presented are corrected using the measured average diameter which is also listed for each ramp rate. The slowest ramp rate, 1 °C/min, and fastest ramp rate, 50 °C/min, had the weakest fibers with both barely reaching an average tensile strength of 1 GPa and an average strain at failure less than 1%. A ramp rate of 47.2 °C/min was found to produce the largest diameter CFs which was assumed to be due to reactions occurring so quickly that the fiber had difficulty creating new bonds thereby inhibiting the axial shrinkage that would typically occur as the graphitic planes shift closer. At slower ramp rates, the graphitic planes should be able to bond and shrink the fiber, but the opposite was observed. At the slowest ramp rate, the diameter of the fibers is nearly identical to the CFs produced from 47.2 °C/min. One possible explanation for the lack of axial shrinkage at such a low ramp rate could stem from the carbonization reactions occurring across a longer period. This would result in a smaller number of bondable carbons being present at any given time and thus limit the amount the graphitic planes can bond.

Table 14. Table of mechanical properties with their standard deviations for CFs produced from varying ramp rates

Ramp Rate (°C/min)	Diameter (µm)	Strength (GPa)	Modulus (GPa)	Strain (%)
1	12.45 ± 1.25	1.02 ± 0.31	132.2 ± 12.3	0.77 ± 0.23
5.2	12.13 ± 0.94	1.46 ± 0.33	132.3 ± 10.3	1.10 ± 0.26
9.9	11.93 ± 0.86	1.57 ± 0.32	148.8 ± 9.6	1.06 ± 0.23
33.7	12.08 ± 0.93	1.64 ± 0.39	145.8 ± 14.3	1.12 ± 0.28
47.2	12.51 ± 0.90	1.17 ± 0.38	120.9 ± 13.1	0.97 ± 0.26

These results align with the findings of Mochida et al. [181], who found an increase in tensile strength and decrease in fiber diameter when carbonizing coal tar MPCF at 10 °C/min as compared to 5 °C/min. They found that their CFs possessed a core-shell structure for both ramp rates and that the CFs carbonized at 10 °C/min had a broader core. This increase in a disordered core, as compared to the more graphitic shell, could explain the increase in tensile strength. Qian et al. found a connection between CF disorder and mechanical strength [131]. High strength PAN-CF were more disordered as compared to high modulus, moderate strength pitch CFs. Therefore, MPCF produced with a disordered core would have a high strength region increasing the tensile strength of the entire fiber. However, as also shown by Mochida [181] and in this study, too fast of a ramp rate during carbonization will lead to defects which will result in a decrease of the CFs' mechanical properties.

Given that both extreme ramp rates showed decreased mechanical properties and increased diameters, MATLAB was used to derive a parabolic fit (13)**Error! Reference source not found.** with the goal of finding a ramp rate capable of producing the strongest CF. The fit was found to be of acceptable quality with an R-square value of 0.9 and is shown in **Figure 61**.

$$\mathrm{F(x)} = -0.001279(\mathrm{x})^2 + 0.06211(\mathrm{x}) + 1.06 \qquad \textbf{(13)}$$

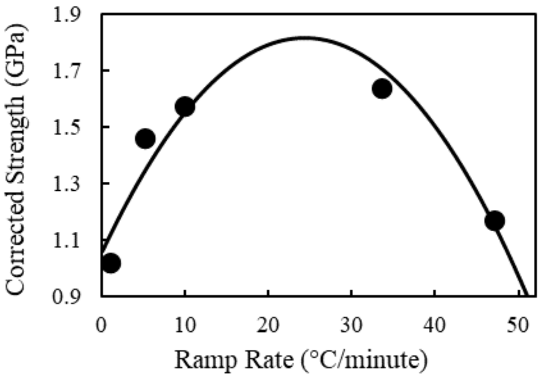

Figure 61. Strength vs ramp rate curve fit with a parabolic function

The parabolic fit also presents a vertex which could signify a ramp rate which would produce a stronger CF. That vertex was determined to occur at a ramp rate of 24.3 °C/min. A new batch of fiber was carbonized in the Thermolyne furnace with the new set ramp rate, **Figure 62**. Once again, the furnace was unable to control the rate perfectly and the average ramp rate for the region of interest was 26.5 °C/min. The CFs produced with this rate were subjected to the same mechanical tests and the result was a stronger fiber with an average ultimate stress of 1.74 GPa as compared to 1.64 GPa for a ramp rate of 33.7 °C/min. The average diameter of the CFs produced with a ramp rate of 26.5 °C/min also yielded the smallest average diameter of 11.67 microns which is a 6.3% reduction compared to the CFs produced with a ramp rate of 1 °C/min. While an increase in strength for a ramp rate of 26.5 °C/min was correctly predicted, it is still unclear as to why this is the case requiring investigation of the sample fibers' microstructure.

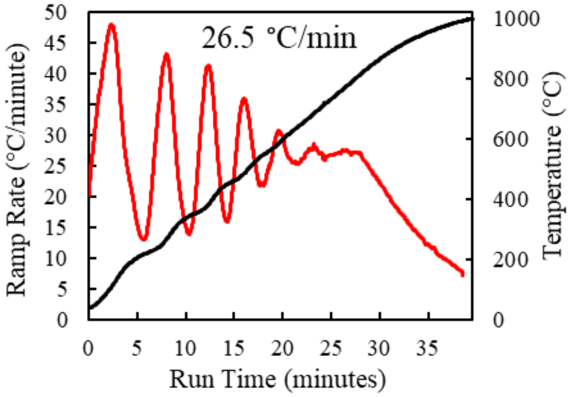

Figure 62. CF thermal history produced with a set ramp rate of 23.3 °C/min

SEM images of the CF cross sections were taken post-fracture and are presented in **Figure 63**. Initial observations concluded that no macroscale defects such as Pac-man splitting were present in any of the CFs regardless of ramp rate. Therefore, the differences between the CFs' mechanical properties must be induced via microstructure changes. All CFs possess a radial microstructure which is most clearly defined near the edge of the fibers. A radial microstructure is expected given the use of a 100-micron circular nozzle with no disruption pack to prohibit this type of crystalline alignment [51]. SEM provided no visual difference in the macro and microstructures between the CFs, so Raman and XRD were used to probe the crystalline microstructure for differences.

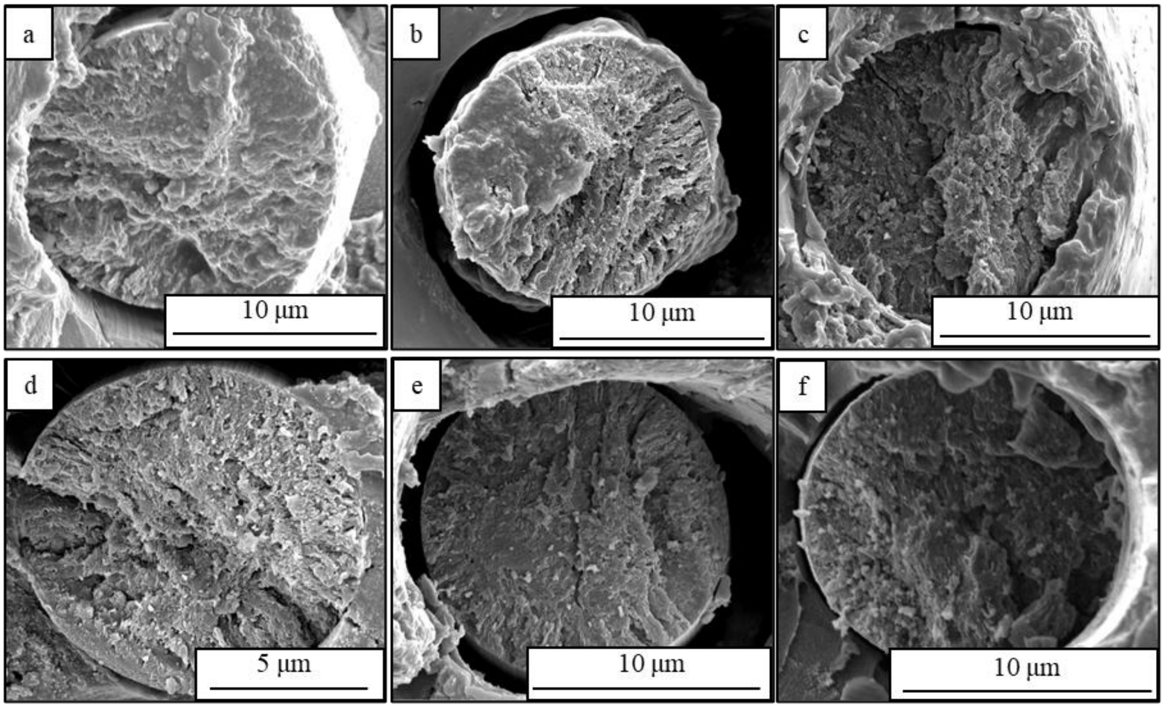

Figure 63. SEM images of tensile fracture surfaces of CF produced via varied ramp rates: (a) 1 °C/min, (b) 5.2 °C/min, (c) 9.9 °C/min, (d) 26.5 °C/min, (e) 33.7 °C/min, (f) 47.2 °C/min

Previous works have investigated the use of Raman spectroscopy to identify microstructural differences in CFs based on precursor material, final carbonization temperature, and thermal history [6]. The most common method for analyzing the results has been the use of I_D/I_G which has shown to range from values of near zero to greater than 4 [169]. Given that the ratio is calculated by dividing the area of the D band by the area of the G band, a lower value is associated with a more graphitic structure. As the number of defects present increases, I_D/I_G increases as the material becomes less graphitic in nature. It should be noted that defects is a term which encompasses edges, voids, sp^3 bonding, and the presence of non-carbon atoms [182]. Therefore, an increase in defects is not directly related to a decrease in mechanical properties but rather a disruption of the pristine graphitic structure. Due to mesophase pitch being an aromatic precursor, its CFs tend to have lower I_D/I_G values when compared to CFs produced from PAN [134].

Researchers have used this difference to study if I_D/I_G can be used to predict tensile strength since the largest values of I_D/I_G stem from higher quality PAN-CF with strengths of 4 GPa and greater [131].

The values of I_D/I_G along the surface and core of the CFs produced from varying ramp rates are shown in **Figure 64**. Regardless of the ramp rate used to carbonize the CFs, the I_D/I_G value is larger for the core of the fibers when compared to the surface. MPCF are known to have slightly less graphitic cores because they experience lower carbonization temperatures than the surface of the fiber. This phenomenon arises from poor oxidation which inhibits conductive heating through the skin of the fiber [33, 53-55]. Often referred to as "skin-core" structure in literature, the differences in experienced temperatures throughout the cross section of the fibers yields a more graphitic outer shell which wraps around a less graphitic core. Therefore, it is expected that I_D/I_G increases when moving from the surface of the fiber to its core.

For ramp rates of 26.5 °C/min and below, the difference between the I_D/I_G values at the core and surface of the fiber is no greater than 7% and the average surface values all fall within one standard deviation of the cores' values. This shows that at lower carbonization ramp rates, the core of the fibers was carbonized to nearly the same degree as the surface of the fiber. However, a ramp rate of 33.7 °C/min led to 15.8% difference between the core and surface's I_D/I_G values. The fastest ramp rate, 47.2 °C/min, created an even larger difference between the core and surface with the surface I_D/I_G average value being 20% less than that of the core. As previously mentioned, Qian et al. found an increase in disorder, the I_D/I_G ratio, corresponded to an increase in tensile strength [131]. Given a core with a higher tensile strength and a graphitic shell with a higher modulus, there would exist an ideal ratio of core to shell to produce the strongest CF. This paper shows that ratio is created using a ramp rate of 26.5 °C/min. With any faster ramp rates, defects are introduced resulting in the decrease of mechanical properties. While Raman spectroscopy analyzes parts of the CF, it is not possible to extract the entire graphitic structure and is best used in conjunction with XRD [132].

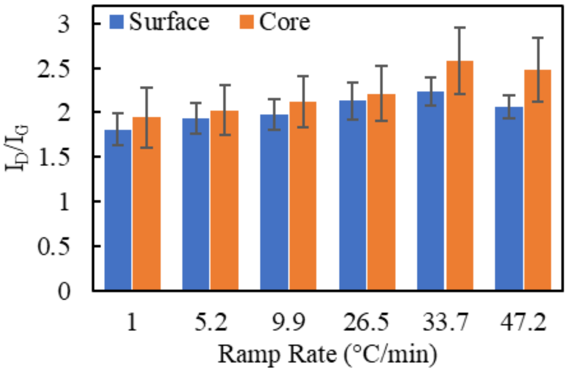

Figure 64. I_D/I_G for surface (blue) and core (orange) scans of CF produced with varying ramp rates with their respective standard deviations

Both the mean interlayer spacing, d_{002}, and L_c were calculated using the (002) peak position and FWHM, while L_a was determined from the (10) peak and all values are presented in **Figure 65**. L_c was found to consistently increase in size with faster ramp rates with the only exception being the fastest ramp rate of 47.2 °C/min which had an estimated L_c equal to that of the L_c produced with a ramp rate of 33.7 °C/min (**Figure 65**a). L_a did not follow a linear path but instead produced a pseudo parabolic shape with the minimum value being a result of the 10 °C/min ramp rate (**Figure 65**b). Given that the two fastest ramp rates had the largest values of both L_c and L_a, it can be concluded that these CFs contain a more graphitic structure as compared to the other CFs produced from slower ramp rates. Of note, d_{002} is not affected by ramp rate in the same manner as crystallite size. Rather, d_{002} holds constant with the largest disparity being .004 nm which came from CFs produced with a ramp rate of 1 and 5.2 °C/min. This shows that d_{002} was influenced by the final heat treatment temperature and not the ramp rate used to achieve 1000 °C (**Figure 65**c).

XRD analysis of the fibers supports the conclusion that the graphitic nature of the CFs increases with an increase in ramp rate with an increase in crystallite size and a decrease in interlayer spacing. By juxtaposing L_c and L_a with the I_D/I_G values calculated using Raman spectroscopy, the increase in I_D/I_G at the surface for an increase in ramp rate was due solely to an increase in defects and not crystallite edges or a decrease in the graphitic structure.

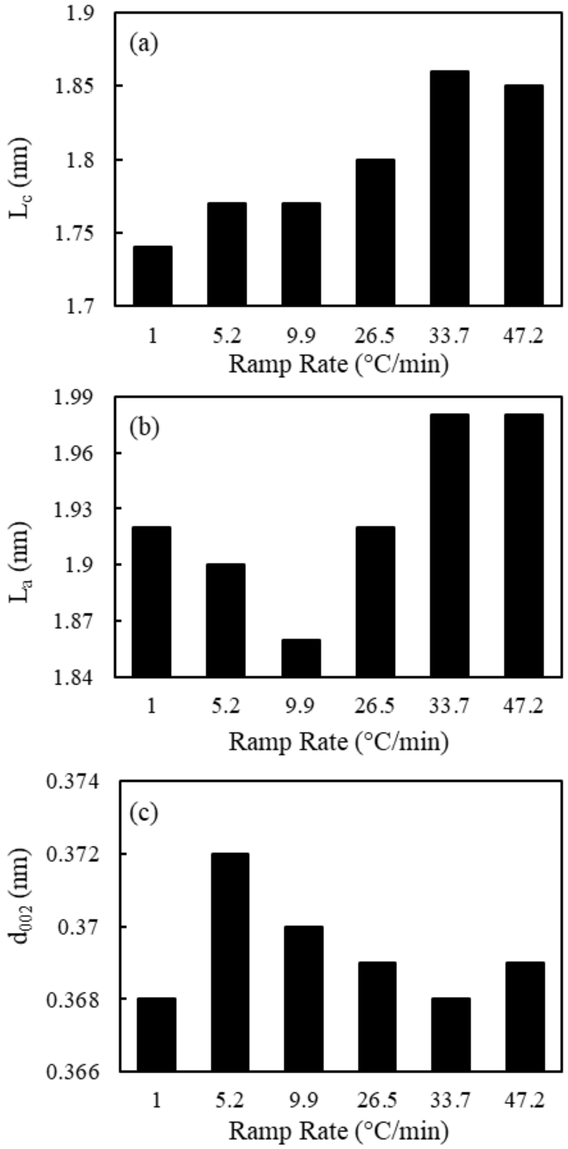

Figure 65. Crystallite parameters: (a) Lc, (b) La, and (c) d002

4. Conclusion

The microstructure and mechanical properties of MPCF was tuned by varying ramp rates ranging from 1 °C/min to 47.2 °C/min with the goal of reducing production cost through reducing cycle time. An optimal ramp rate was found to be 26.5 °C/min producing a CF with the highest strength reaching 1.74 GPa on average. SEM inspections revealed a radial microstructure without

Pac-man splitting or other large defects. Raman spectroscopy found that faster ramp rates lead to a breakdown in the CF's graphitic structure with higher values of I_D/I_G found for faster ramp rates while also leading the creation of skin-core structures. The ratio of skin-core alters the mechanical properties, and the ideal structure was created using a ramp rate of 26.5 °C/min. XRD was used to discover that the largest graphitic crystallite growth occurred for faster ramp rates proving that the increase in the I_D/I_G surface scans was due to increases in graphitic defects, not reductions in the crystallite sizes. Investigations into carbonization and the complicated reactions that occur during thermal treatment are continuing to be explored. This paper highlights that carbonization ramp rate can be used to tune the microstructure of MPCF for different applications.

Chapter 7: Concluding remarks and recommendations

1. Summary

MPCF is a high-performance material that has been used in multiple applications, including aerospace, space satellites, and defense [21–23]. These specialized fibers have tensile strengths as high as 3.7 GPa, with a tensile modulus that can approach 1000 GPa [20]. Meanwhile, their high thermal and electrical conductivity make them highly sought after in fields that require advanced material properties, such as radar absorption and low thermal expansion [185,186]. However, despite their significant uses, MPCF makes up only 10% of the CF market due to high cost, lower tensile strength (compared to PAN-CF), and difficulty in scaling [4].

In order to create more opportunities for MPCF, tailoring its macro-properties through alterations in the microstructure must be understood to produce CF for specific end-use cases. The structure of MPCF is complicated but also easily modified at every step of the CF production process. Mesophase pitch has been shown to be dependent on the feedstock material, mesophase formation, and any additives introduced prior to mesophase conversion or directly before extrusion. The extrusion of the fibers lays the groundwork for the microstructure and cross-sectional texture shape, both of which have a significant impact on CF macro-properties and can be controlled using specialized nozzles and flow disrupters.

Oxygen stabilization is a delicate process. Under-oxidation leads to the formation of a skin-core structure, resulting in depressed tensile properties, while over-oxidation causes fiber deterioration, also leading to lower tensile properties. This highlights the importance of finding the correct balance of temperature and exposure time. Finally, high-temperature heat treatment is what produces CF, as the majority of non-carbon atoms exit the fibers and new carbon-carbon bonds are formed, developing crystallites and the final structure. These complicated reactions depend not only on the final temperature but also on the rate at which they occur, a subject currently under review.

Through this dissertation, I set out to examine each processing step in MPCF production and identify key areas that could be altered or improved in an effort to control the microstructure of the fiber. With this effort, new methods for microstructure alteration were introduced and discussed, and a deeper understanding of the structure-property relationship was developed. This relationship is key for all CF production, not just MPCF, as a deeper understanding of these interactions will allow for the creation of stronger, stiffer, and highly conductive CF in the future. The contributions made to each production step in this dissertation are summarized below.

2. Key contributions and broader impacts

2.1. Precursor

Mesophase pitch, as a precursor material, represents a lower-cost alternative to PAN, but there is still room for cost reduction if CF is to be used in markets such as car manufacturing, as well as an environmental impact that must be considered. In Chapters 2 and 3, the hypothesis that blending polymers with mesophase pitch to spin hybrid precursor fibers could create quality CF at a lower cost and reduced environmental impact was tested by probing the weight percentages of two different polymers: LLDPE (Chapter 2) and PET (Chapter 3). Previous works have attempted the combination of both LLDPE [68,69] and PET [142] to create hybrid precursor fibers, but they failed to spin them at diameters small enough for sufficient stabilization to be completed and did not analyze the structure or the developed CF.

The results in these chapters found that both LLDPE and PET could be combined with mesophase pitch and spun into precursor fibers with diameters less than 30 μm. However, upon further analysis, it was found that the materials did not mix well and instead, the polymers coalesced in the lower molecular weight isotropic pitch regions. The resulting pitch-LLDPE CF tested poorly for all combinations, with the LLDPE volatilizing during carbonization and leaving large voids, which greatly reduced the tensile properties of the CF. This disproved the hypothesis that a pitch-LLDPE combination would inherit the better qualities of both materials. However, the combination of mesophase pitch and 5 wt.% PET resulted in CF with a slightly lower tensile strength but an increased modulus and better crystallinity. These fibers represent the possibility that higher crystalline MPCF could be developed using a waste polymer, which would result in direct cost reduction and a recycling opportunity for PET.

2.2. Extrusion

Extrusion of mesophase pitch-based fibers is the most explored and published area of all the CF production steps, given the number of variables that can be altered and the large impact each one has on the subsequent structure of the fiber. Previous works have shown that changes to the nozzle geometry, reservoir cross-section, extrusion temperature, and the addition of flow disruptors result in the transformation of the CF cross-sectional texture shape from 'radial' to 'onion' and to 'random,' as well as their impact on the CF macro-properties [51,74,82]. However, these publications have lacked explanations of the micro- and mesostructural characteristic differences and their role in the CF tensile properties. In Chapter 4, this gap is addressed through the creation of 'radial' and 'random' textured MPCF, followed by a sweeping analysis of the microstructure for both sets of CF. By completing a full microstructure analysis alongside tensile results, a better understanding of the structure-property relationship of MPCF can be developed and leveraged in future works.

Using WAXD, it was found in Chapter 4 that the random-texture CF possessed higher crystallinity, larger crystallites, and better axial orientation than the radial-texture CF. A deeper probe using TEM and FFT revealed that the radial fibers developed a core-shell structure despite a successful and identical oxidation treatment. The radial profile was created from high shear stress during extrusion, which aligned the graphitic sheets to a single point at the center of the fiber. Therefore, at the center of the fiber, there was less mobility for the crystallites to restructure during carbonization, forcing them to grow slower and in more randomized directions—something not previously published. The random fibers, of similar size and identical treatment, contained no such core-shell structure and had uniform crystallites throughout the entire CF. This difference explains the variation in tensile properties, as the random fibers were found to be mechanically superior. This highlights the importance of developing a better understanding of the microstructure's impact on the macro-scale properties.

2.3. Oxidation

Oxygenated stabilization of mesophase pitch precursor fibers makes high-temperature heat treatment possible. However, oxidation remains a complicated and difficult process, as under-oxidation leads to a core-shell structure, while over-oxidation hampers crystallite growth, and both result in reduced mechanical properties [103,108,125,178]. To combat this conundrum, the work in Chapter 5 highlights two methods for measuring oxygen uptake as a way to determine successful oxidation, something not yet discussed in previous works. By simply measuring the weight increase during oxidation, a higher temperature is able to reach a mark of 10 wt.% oxygen more quickly, which could result in cost reduction, as operating oxidation furnaces is expensive. However, this method may lead to over-oxidation, as it does not account for additional reactions in which carbon is removed via CO, resulting in a fiber with higher oxygen content and mechanically poor properties. Rather, atomic mapping across the fiber's cross-section to account for total oxidation and its location stands as a better method to avoid core-shell formation and prevent co-reactions that lead to a higher-than-desired oxygen level. This method developed a better understanding of the oxidation reactions in mesophase pitch and provided the groundwork for any researchers wishing to study these reactions at different temperatures or with different materials.

2.4. Carbonization

The role of the final heat treatment temperature on MPCF has been well established and evaluated in numerous studies [187]. However, the ramp rate utilized during these temperature treatments has been largely ignored, with some publications neglecting to even record it. Chapter 6 highlights the importance of ramp rates, as carbonization is a multi-reaction process in which atoms are removed and new bonds are formed, resulting in significant shifts in both the microstructure and macro-properties. The only previous work that discussed this focused on ramp rates set below 1 °C/min, which cannot be compared to large-scale runs, as they typically use ramp rates much closer to 50 °C/min due to the high cost of operating these energy-intensive furnaces. By examining ramp rates ranging from 1 to 50 °C/min, it was identified that a rate of approximately 23.3 °C/min should be used to achieve a CF with the highest potential tensile strength while still operating in a manner that ensures cost reduction, and a lower environmental impact compared to rates around 1 °C/min.

3. Recommendations for future work

The result of this dissertation is a roadmap for the production of MPCF and the development of methods at each step to control the microstructure in order to tailor the fiber to the user's desires, whether that be cost reduction, increased strength, or environmental concerns. Each step discussed still presents opportunities for future work, as any change will alter the final structure, and combinations of changes still need to be explored.

3.1. Mesophase pitch-polystyrene

As demonstrated in Chapter 3, if the correct polymer is chosen, blending mesophase pitch with a polymer can result in fibers that possess unique and useful characteristics, while also representing a new recycling alternative for some waste plastics and offering a cost-reduction opportunity. However, the wrong choice of polymer, as illustrated in Chapter 2, will lead to a complete deterioration of mechanical properties. To this end, future work should focus on selecting common polymers with higher char yields and functional groups that can assist with blending with mesophase pitch. For example, polystyrene (PS) is one interesting candidate. PS is a very common plastic that is difficult to recycle and inexpensive [188]. It contains an aromatic hydrocarbon along its backbone, making it an ideal candidate to blend with mesophase pitch [189]. Some groups have shown that PS can be used to increase mesophase production [59], but no one has blended it directly with pitch prior to extrusion in an effort to leverage the polymer's mechanical properties. The addition of polymers has proven to make pitch extrusion simpler by acting as a plasticizer while also altering the microstructure [63]. Therefore, mixing mesophase pitch with PS, a polymer already shown to interact well with mesophase pitch, provides an interesting framework for future blending studies.

3.2. Radial-random texture

Chapter 4 presents a process for creating and analyzing the microstructure of MPCF with different cross-sectional textures. This work discusses only the differences between ‘radial’ and ‘random’ textures, but there are many more, each with unique characteristics. In the immediate future, the combination of a radial-random texture, which possesses a random core but a radial shell, should be examined. Such a structure has been recorded before [83,190]. While some works originally stated that the difference in mesoscopic textures had little effect on the mechanical properties [191], the work presented in Chapter 4 offers a different conclusion. A ‘radial-random’ combination texture could represent an avenue in which the CF has a stiff shell combined with larger crystallites in the core, allowing for a high tensile strength and modulus fiber. If possible, the benefits of both structures could be leveraged, enabling the production of the best MPCF.

3.3. Heat-treatment advancements

High-temperature heat treatment of mesophase pitch to create CF involves multiple reactions that occur at different rates and onset temperatures. The major outcome of Chapter 6 is proof that the ramp rate must be considered when treating CF, as different rates lead to different microstructure growth and orientations. To this end, there are two future efforts that can be undertaken immediately following this work.

Oxidation studies have been completed using a variable rate method in which the rates are modified depending on the temperature zone [192,193]. As shown in Chapter 6, the largest amount of weight loss occurs in the 300–800 °C region. It would be interesting to examine the outcome if one were to slow the rate in this region and then use a higher ramp rate above 800 °C. The idea is that a slow ramp rate in the lower region allows for more noncarbon atoms to be removed from the system before increasing the rate to achieve maximum cost reductions. Conversely, a faster ramp rate in the same region could result in a higher percentage of noncarbon atoms remaining but more cross-bonding between layers, generating a structure similar to PAN-CF and possibly resulting in an increase in tensile strength.

Additionally, it would be of interest to examine whether the increase in tensile strength for a ramp rate of 23.3 °C/min would carry over with increased heat treatment temperatures. Most notably, would the differences in structure from varied ramp rates hold if all the fibers were treated to graphitization levels (> 1800 °C) at the same rates? Given that extrusion studies have shown that the groundwork for the CF structure is laid early in the process [194], one might find that further heat treatment results in an identical graphitized fiber regardless of the rate used to remove the noncarbon atoms in the carbonization region. Alternatively, it is possible that the different growth rates of the crystals at the skin, shell, and core of the CF are set and will continue to grow at different rates during graphitization. Such a difference in crystalline structure throughout a graphitized fiber could provide interesting tensile results, as well as influence electrical and thermal properties, as graphitized fibers are typically used for these applications.

Bibliography

[1] T.A. Edison, Electric lamp, US Patent No. 223.898, 1880. http://www.google.com/patents/US223898.

[2] S.-J. Park, G.-Y. Heo, Carbon Fibers, Springer Science & Business Media, 2015. https://doi.org/10.1007/978-94-017-9478-7.

[3] F. Tanaka, Pioneering the carbon fiber frontier: A half-century of industry leadership and the road ahead, Compos. Part B Eng. 281 (2024) 111515. https://doi.org/10.1016/j.compositesb.2024.111515.

[4] Carbon fiber market size, share & COVID-19 impact analysis, by precursor (PAN and pitch), by tow (large tow and small tow), by application (aviation, aerospace & defense, automotive, wind turbines, sports & leisure, construction, and others), and regional, 2023. https://doi.org/FBI101719.

[5] D. Choi, H.-S. Kil, S. Lee, Fabrication of low-cost carbon fibers using economical precursors and advanced processing technologies, Carbon N. Y. 142 (2019) 610–649. https://doi.org/10.1016/j.carbon.2018.10.028.

[6] Z.E. Brubaker, J.J. Langford, R.J. Kapsimalis, J.L. Niedziela, Quantitative analysis of Raman spectral parameters for carbon fibers: practical considerations and connection to mechanical properties, J. Mater. Sci. 56 (2021) 15087–15121. https://doi.org/10.1007/S10853-021-06225-1.

[7] H.S. Roh, T.Q. Hua, R.K. Ahluwalia, Optimization of carbon fiber usage in Type 4 hydrogen storage tanks for fuel cell automobiles, Int. J. Hydrogen Energy. 38 (2013) 12795–12802. https://doi.org/10.1016/j.ijhydene.2013.07.016.

[8] Carbon Fiber for Lightweight Vehicles : Summary Report, 2013.

[9] B. Shaffer, M. Auffhammer, C. Samaras, Make electric vehicles lighter to maximize climate and safety benefits, Nature. 598 (2021) 254–256. https://doi.org/10.1038/d41586-021-02760-8.

[10] S. Yang, Y. Cheng, X. Xiao, H. Pang, Development and application of carbon fiber in batteries, Chem. Eng. J. 384 (2020) 123294. https://doi.org/10.1016/j.cej.2019.123294.

[11] L. Bao, J. Zang, X. Li, Flexible Zn2SnO4/MnO2 core/shell nanocable-carbon microfiber hybrid composites for high-performance supercapacitor electrodes, Nano Lett. 11 (2011) 1215–1220. https://doi.org/10.1021/nl104205s.

[12] A. Al-lami, P. Hilmer, M. Sinapius, Eco-efficiency assessment of manufacturing carbon fiber reinforced polymers (CFRP) in aerospace industry, Aerosp. Sci. Technol. 79 (2018) 669–678. https://doi.org/10.1016/j.ast.2018.06.020.

[13] S. Lina, D. Zhen, The carbon fiber composite materials application in sports equipment, (2012) 173–176. https://doi.org/10.4028/www.scientific.net/AMR.341-342.173.

[14] S. Nunna, P. Blanchard, D. Buckmaster, S. Davis, M. Naebe, Development of a cost model for the production of carbon fibres, Heliyon. 5 (2019).

https://doi.org/10.1016/j.heliyon.2019.e02698.

[15] M.Z. Özel, K.D. Bartle, Production of mesophase pitch from coal tar and petroleum pitches using supercritical fluid extraction, Turkish J. Chem. 26 (2002).

[16] L.D. De Castro, Anisotropy and mesophase formation towards carbon fibre production from coal tar and petroleum pitches - A review, J. Braz. Chem. Soc. 17 (2006) 1096–1108.

[17] M. Wang, B. Yang, T. Yu, X. Yu, M. Rizwan, X. Yuan, X. Nie, X. Zhou, Research progress in the preparation of mesophase pitch from fluid catalytic cracking slurry, RSC Adv. 13 (2023) 18676–18689. https://doi.org/10.1039/d3ra01726e.

[18] T. Industries, Toray Develops TORAYCA $^{\text{TM}}$ T1200 , the Ultra-High-Strength Carbon Fiber, (2023) 29–32.

[19] A. Sharma, M.M. Amin, M.A. Al Bari, M.M. Hossain, M.N. Siddiquee, Carbon fiber from petroleum pitch: Current advances and potential applications, Energy Nexus. 17 (2025). https://doi.org/10.1016/j.nexus.2024.100355.

[20] M.G. Huson, High-performance pitch-based carbon fibers, Elsevier Ltd, 2017. https://doi.org/10.1016/B978-0-08-100550-7.00003-6.

[21] V. Stergiou, G. Konstantopoulos, Carbon fiber reinforced plastics in space: life cycle assessment towards improved sustainability of space vehicles, J. Compos. Sci. 144 (2022).

[22] J. Jeremy, J. Samuel, R. Ramadoss, K.N. Gunasekaran, K. Logesh, S.J. Patrick, A.A. Munaf, Materials Today : Proceedings Studies on mechanical properties and characterization of carbon fiber reinforced hybrid composite for aero space application, Mater. Today Proc. 47 (2021) 4438–4443. https://doi.org/10.1016/j.matpr.2021.05.304.

[23] B. Sun, C. Xue, W. Shang, M. An, H. Zhao, H. Zhang, The performance characterization of carbon fiber – reinforced plastic for space applications, J. Re. 42 (2023) 844–853. https://doi.org/10.1177/07316844221141367.

[24] Y. Arai, Pitch-based carbon fibers, in: High-Performance Spec. Fibers, Springer, Tokyo, 2016: pp. 343–354. https://doi.org/https://doi.org/10.1007/978-4-431-55203-1_21.

[25] A. Scherschel, T. Harrell, A. Sushchenko, E. Knight, K.R. Brown, X. Li, Tuning microstructure of mesophase pitch carbon fiber by altering the carbonization ramp rate, Adv. Eng. Mater. 2400110 (2024) 1–9. https://doi.org/10.1002/adem.202400110.

[26] J. Liu, X. Chen, D. Liang, Q. Xie, Development of pitch-based carbon fibers: a review, Energy Sources, Part A Recover. Util. Environ. Eff. (2020) 1–21. https://doi.org/10.1080/15567036.2020.1806952.

[27] T. Maeda, S. Ming Zeng, K. Tokumitsu, J. mondori, I. Mochida, Preparation of isotropic pitch precursors for general purpose carbon fibers (GPCF) by air blowing-I. Preparation of spinnable isotropic pitch precursor from coal tar by air blowing, Carbon N. Y. 31 (1993) 407–412. https://doi.org/10.1016/0008-6223(93)90127-V.

[28] T. Peijs, R. Kirschbaum, P.J. Lemstra, Chapter 5: A critical review of carbon fiber and related products from an industrial perspective, in: Adv. Ind. Eng. Polym. Res., Kingfa Scientific and Technological Co. Ltd., 2022: pp. 90–106.

https://doi.org/10.1016/j.aiepr.2022.03.008.

[29] B.-J. Kim, T. Kotegawa, Y. Eom, J. An, I.-P. Hong, O. Kato, K. Nakabayashi, J. Miyawaki, B.C. Kim, I. Mochida, S.-H. Yoon, Enhancing the tensile strength of isotropic pitch-based carbon fibers by improving the stabilization and carbonization properties of precursor pitch, Carbon N. Y. 99 (2016) 649–657. https://doi.org/10.1016/j.carbon.2015.12.082.

[30] J. Zhu, S.W. Park, H.-I. Joh, H.C. Kim, S. Lee, Preparation and characterization of isotropic pitch-based carbon fiber, Carbon Lett. 14 (2013) 94–98. https://doi.org/10.5714/cl.2013.14.2.094.

[31] S. Rani, P. Kumar, K. Kumari, S.R. Dhakate, S. Kumari, Effect of carbonization conditions on microstructural properties of isotropic coal tar pitch-based general-purpose carbon fibers, Diam. Relat. Mater. 140 (2023). https://doi.org/10.1016/j.diamond.2023.110525.

[32] T.H. Lim, M.S. Kim, S.Y. Yeo, E. Jeong, Preparation and evaluation of isotropic and mesophase pitch-based carbon fibers using the pelletizing and continuous spinning process, J. Ind. Text. 48 (2019) 1242–1253. https://doi.org/10.1177/1528083718763774.

[33] V. Patel, Manufacturing and mechanical characterization of low-cost isotropic pitch-based carbon fiber, 2021.

[34] J.D. Craddock, G. Frank, M. Martinelli, J. Lacy, V. Edwards, A. Vego, C. Thompson, R. Andrews, M.C. Weisenberger, Isotropic pitch-derived carbon fiber from waste coal, Carbon N. Y. 216 (2024) 2–5. https://doi.org/10.1016/j.carbon.2023.118590.

[35] L.S. Singer, Carbon fibres from mesophase pitch, Fuel. 60 (1981) 839–847. https://doi.org/10.1016/0016-2361(81)90147-2.

[36] M.T. Mackowsky, Results of coke microscopy with the aid of various research methods, Int. Geol. Rev. 2 (1960) 68–81. https://doi.org/10.1080/00206816009473547.

[37] J.D. Brooks, G.H. Taylor, The formation of graphitizing carbons from the liquid phase, Carbon N. Y. 3 (1965). https://doi.org/10.1016/0008-6223(65)90047-3.

[38] G.W. Gray, Molecular structure and the properties of liquid crystals, J. Am. Chem. Soc. 85 (1963) 494. https://doi.org/10.1177/0261018311403863.

[39] J.R. Kershaw, K.J.T. Black, H.K. Jaeger, R.I. Willing, J. V. Hanna, A comparison of mesophase formation under sparging and vacuum, Carbon N. Y. 33 (1995) 633–643. https://doi.org/10.1016/0008-6223(94)00149-T.

[40] G. Yuan, Z. Xue, Z. Cui, A. Westwood, Z. Dong, Y. Cong, J. Zhang, H. Zhu, X. Li, Constructing the bridge from isotropic to anisotropic pitches for preparing pitch-based carbon fibers with tunable structures and properties, ACS Omega. 5 (2020) 21948–21960. https://doi.org/10.1021/acsomega.0c03226.

[41] F. Derbyshire, R. Andrews, D. Jacques, M. Jagtoyen, G. Kimber, T. Rantell, Synthesis of isotropic carbon fibers and activated carbon fibers from pitch precursors, Fuel. 80 (2001) 345–356. https://doi.org/10.1016/S0016-2361(00)00099-5.

[42] I. Mochida, Y. Korai, C.-H. Ku, F. Watanabe, Y. Sakai, Chemistry of synthesis, structure, preparation and application of aromatic-derived mesophase pitch, Carbon N. Y. 38 (2000)

305–328. https://doi.org/10.1016/S0008-6223(99)00176-1.

[43] Y. Yang, Q. Lin, Y. Huang, D. Guo, Efficient preparation of mesocarbon microbeads by pyrolysis of coal-tar pitch in the presence of rosin, J. Anal. Appl. Pyrolysis. 91 (2011) 310–315. https://doi.org/10.1016/j.jaap.2011.03.005.

[44] J.D. Kim, J.S. Roh, M.S. Kim, Effect of carbonization temperature on crystalline structure and properties of isotropic pitch-based carbon fiber, Carbon Lett. 21 (2017) 51–60. https://doi.org/10.5714/CL.2017.21.051.

[45] J. Guo, X. Li, H. Xu, H. Zhu, B. Li, A. Westwood, Molecular structure control in mesophase pitch via co-carbonization of coal tar pitch and petroleum pitch for production of carbon fibers with both high mechanical properties and thermal conductivity, Energy and Fuels. 34 (2020) 6474–6482. https://doi.org/10.1021/acs.energyfuels.0c00196.

[46] J. Kim, U.S. Im, B. Lee, D.H. Peck, S.H. Yoon, D.H. Jung, Pitch-based carbon fibers from coal tar or petroleum residue under the same processing condition, Carbon Lett. 19 (2016) 72–78. https://doi.org/10.5714/CL.2016.19.072.

[47] G. Yuan, B. Li, X. Li, Z. Dong, W. Hu, A. Westwood, Y. Cong, J. Zhang, Effect of liquid crystalline texture of mesophase pitches on the structure and property of large-diameter carbon fibers, ACS Omega. 4 (2019) 1095–1102. https://doi.org/10.1021/acsomega.8b03189.

[48] A.B. Barnes, F.M. Dauché, N.C. Gallego, C.C. Fain, M.C. Thies, As-spun orientation as an indication of graphitized properties of mesophase-based carbon fiber, Carbon N. Y. 36 (1998) 855–860. https://doi.org/10.1016/S0008-6223(97)00166-8.

[49] I. Mochida, S.-H. Yoon, Y. Korai, Mesoscopic structure and properties of liquid crystalline mesophase pitch and its transformation into carbon fiber, Chem. Rec. 2 (2002) 81–101. https://doi.org/10.1002/tcr.10016.

[50] H. Wu, D. Huang, C. Ye, T. Ouyang, S. Zhu, Z. Fan, G. Ye, X. Wu, K. Shi, F. Han, H. Liu, J. Liu, Engineering microstructure toward split-free mesophase pitch-based carbon fibers, J. Mater. Sci. 57 (2022) 2411–2423. https://doi.org/10.1007/s10853-021-06770-9.

[51] Y. Yao, J. Chen, L. Liu, Y. Dong, A. Liu, Mesophase pitch-based carbon fiber spinning through a filter assembly and the microstructure evolution mechanism, J. Mater. Sci. 49 (2014) 191–198. https://doi.org/10.1007/s10853-013-7692-z.

[52] M. Endo, C. Kim, T. Karaki, T. Tamaki, Y. Nishimura, Structural analysis of the B-doped mesophase pitch-based graphite fibers by Raman spectroscopy, Phys. Rev. B - Condens. Matter Mater. Phys. 58 (1998) 8991–8996. https://doi.org/10.1103/PhysRevB.58.8991.

[53] J. Guo, H. Zhu, H. Xu, A. Westwood, X. Li, Spinnable mesophase pitch prepared via co-carbonization of fluid catalytic cracking decant oil and synthetic naphthalene pitch, Energy and Fuels. 34 (2020) 2566–2573. https://doi.org/10.1021/acs.energyfuels.9b03841.

[54] R.M. Alway-Cooper, D.P. Anderson, A.A. Ogale, Carbon black modification of mesophase pitch-based carbon fibers, Carbon N. Y. 59 (2013) 40–48. https://doi.org/10.1016/j.carbon.2013.02.048.

[55] K. Kanno, J.J. Fernandez, F. Fortin, Y. Korai, I. Mochida, Modifications to carbonization of mesophase pitch by addition of carbon blacks, Carbon N. Y. 35 (1997) 1627–1637. https://doi.org/10.1016/S0008-6223(97)00123-1.

[56] S.M. Lee, S.H. Lee, J.S. Roh, Analysis of activation process of carbon black based on structural parameters obtained by XRD analysis, Crystals. 11 (2021) 1–11. https://doi.org/10.3390/cryst11020153.

[57] A. Owen, Assisted development of mesophase pitch with dispersed graphene and its resulting carbon fibers dispersed graphene and its resulting carbon fibers, University of Kentucky, 2018. https://doi.org/10.13023/etd.2018.454.

[58] X. Zhang, S. Ning, Z. Ma, H. Song, D. Wang, M. Zhang, B. Fan, S. Zhang, X. Yan, The structural properties of chemically derived graphene nanosheets/mesophase pitch-based composite carbon fibers with high conductivities, Carbon N. Y. 156 (2020) 499–505. https://doi.org/10.1016/j.carbon.2019.09.085.

[59] X. Cheng, Q. Zha, X. Li, X. Yang, Modified characteristics of mesophase pitch prepared from coal tar pitch by adding waste polystyrene, Fuel Process. Technol. 89 (2008) 1436–1441. https://doi.org/10.1016/j.fuproc.2008.07.003.

[60] W.M. Qiao, S.H. Yoon, I. Mochida, J.H. Yang, Waste polyvinylchloride derived pitch as a precursor to develop carbon fibers and activated carbon fibers, Waste Manag. 27 (2007) 1884–1890. https://doi.org/10.1016/J.WASMAN.2006.10.002.

[61] I. Mochida, H. Toshima, Y. Korai, T. Naito, Modification of mesophase pitch by blending Part 2: Modification of mesophase pitch fibre precursor with thermoresisting polyphenyleneoxide (PPO), J. Mater. Sci. 23 (1988) 678–686. https://doi.org/10.1007/BF01174705.

[62] I. Mochida, H. Toshima, Y. Korai, T. Matsumoto, Control of molecular orientations in mesophase pitch-based carbon fibre by blending PVC pitch, J. Mater. Sci. 24 (1989) 57–62. https://doi.org/10.1007/BF00660932.

[63] I. Mochida, H. Toshima, Y. Korai, T. Matsumoto, Blending mesophase pitch to improve its properties as a precursor for carbon fibre Part 1: Blending of PVC pitch into coal tar and petroleum-derived mesophase pitches, J. Mater. Sci. 23 (1988) 670–677. https://doi.org/10.1007/BF01174704.

[64] I. Mochida, H. Toshima, Y. Korai, T. Matsumoto, A microscopic study on the oxidative stabilization of a coal-tar-based mesophase pitch and its blends with PVC pitch, J. Mater. Sci. 24 (1989) 2191–2198. https://doi.org/10.1007/BF02385440.

[65] J.H. Kim, Y.J. Choi, S.E. Lee, J.S. Im, K.B. Lee, B.C. Bai, Acceleration of petroleum based mesophase pitch formation by PET (polyethylene terephthalate) additive, J. Ind. Eng. Chem. 93 (2021) 476–481. https://doi.org/10.1016/j.jiec.2020.10.027.

[66] G. Makomaski, Study on the structure of pitch-polymer compositions by fluorescence microscope, Colloid Polym. Sci. 293 (2015) 297–301. https://doi.org/10.1007/S00396-014-3413-7/FIGURES/3.

[67] S.M. Aldosari, M.A. Khan, S. Rahatekar, Manufacturing carbon fibres from pitch and

polyethylene blend precursors: A review, J. Mater. Res. Technol. 9 (2020) 7786–7806. https://doi.org/10.1016/j.jmrt.2020.05.037.

[68] S.M. Aldosari, M.A. Khan, S. Rahatekar, Influence of high-concentration LLDPE on the manufacturing process and morphology of pitch/LLDPE fibres, Crystals. 11 (2021). https://doi.org/10.3390/cryst11091099.

[69] S.M. Aldosari, M.A. Khan, S. Rahatekar, Manufacturing pitch and polyethylene blends-based fibres as potential carbon fibre precursors, Polymers (Basel). 13 (2021). https://doi.org/10.3390/polym13091445.

[70] J.W. Kim, J.S. Lee, Preparation of carbon fibers from linear low density polyethylene, Carbon N. Y. 94 (2015) 524–530. https://doi.org/10.1016/j.carbon.2015.06.074.

[71] G. Yuan, X. Li, X. Xiong, Z. Dong, A. Westwood, B. Li, C. Ye, G. Ma, Z. Cui, Y. Cong, J. Zhang, Y. Li, A comprehensive study on the oxidative stabilization of mesophase pitch-based tape-shaped thick fibers with oxygen, Carbon N. Y. 115 (2017) 59–76. https://doi.org/10.1016/j.carbon.2016.12.040.

[72] E. Frank, L.M. Steudle, D. Ingildeev, J.M. Spörl, M.R. Buchmeiser, Carbon fibers: Precursor systems, processing, structure, and properties, Angew. Chemie - Int. Ed. 53 (2014) 5262–5298. https://doi.org/10.1002/anie.201306129.

[73] A. Sushchenko, A. Scherschel, C. Love-Baker, R. Cordier, T.M. Harrell, K.R. Brown, X. Li, Evaluating consumer 3D printing nozzles as a low cost alternative for mesophase pitch-derived carbon fiber production, Carbon N. Y. 225 (2024). https://doi.org/10.1016/j.carbon.2024.119088.

[74] Z. Jiang, T. Ouyang, X. Yao, Y. Fei, The effect of the spinning conditions on the structure of mesophase pitch-based carbon fibers by Taguchi method, Carbon Lett. 19 (2016) 89–98. https://doi.org/10.5714/CL.2016.19.089.

[75] M. Matsumoto, T. Iwashita, Y. Arai, Effect of spinning conditions on structures of pitch-based carbon fiber, Carbon N. Y. 31 (1993) 715–720. https://doi.org/10.1016/0008-6223(93)90008-X.

[76] V. Bermudez, A.A. Ogale, Adverse effect of mesophase pitch draw-down ratio on carbon fiber strength, Carbon N. Y. 168 (2020) 328–336. https://doi.org/10.1016/j.carbon.2020.06.062.

[77] Z. Yang, L. Zhang, R. Chen, J.H. He, J.H. Cao, M. Song, Nozzle design in a fiber spinning process for a maximal pressure gradient, Therm. Sci. 17 (2013) 1529–1532. https://doi.org/10.2298/TSCI1305529Y.

[78] T. Ishikawa, F. Tanaka, F. Uehara, M. Tane, Mesoscopic structure with high aspect ratio in PAN-based carbon fibers, Carbon N. Y. (2025). https://doi.org/10.1016/j.lrp.2023.102304.

[79] L.S. Singer, High modulus, high strength carbon fibres produced from mesophase pitch, 1978. https://doi.org/10.1016/0010-4361(78)90685-7.

[80] T. Matsumoto, Mesophase pitch and its carbon fibers, Pure Appl. Chem. 57 (1985) 1553–1562. https://doi.org/10.1351/pac198557111553.

[81] D.D. Edie, N.K. Fox, B.C. Barnett, C.C. Fain, Melt-spun non-circular carbon fibers, Carbon N. Y. 24 (1986) 477–482. https://doi.org/10.1016/0008-6223(86)90271-X.

[82] B. Rahman, Flow modeling of synthetic pitch extrusion through spinnerets for continuous fibers, Clemson University, 2018. https://tigerprints.clemson.edu/all_theses (accessed November 2, 2020).

[83] I. Mochida, S.-H. Yoon, N. Takano, F. Fortin, Y. Korai, K. Yokogawa, Microstructure of mesophase pitch-based carbon fiber and its control, Carbon N. Y. 34 (1996) 941–956. https://doi.org/10.1016/0008-6223(95)00172-7.

[84] M.S.A. Rahaman, A.F. Ismail, A. Mustafa, A review of heat treatment on polyacrylonitrile fiber, Polym. Degrad. Stab. 92 (2007) 1421–1432. https://doi.org/10.1016/j.polymdegradstab.2007.03.023.

[85] K.R. Brown, T.M. Harrell, L. Skrzypczak, A. Scherschel, H.F. Wu, X. Li, Carbon fibers derived from commodity polymers: A review, Carbon N. Y. 196 (2022) 422–439. https://doi.org/10.1016/J.CARBON.2022.05.005.

[86] D.D.L. Chung, Chapter 2: Processing of Carbon Fibers, in: Carbon Fiber Compos., 1st ed., Butterworth-Heinemann, Boston, 1994: pp. 13–53. https://doi.org/10.1016/b978-0-08-050073-7.50006-3.

[87] Y.G. Lü, D. Wu, Q.F. Zha, L. Liü, C.L. Yang, Skin-core structure in mesophase pitch-based carbon fibers: Causes and prevention, Carbon N. Y. 36 (1998) 1719–1724. https://doi.org/10.1016/S0008-6223(97)00172-3.

[88] S. Lu, C. Blanco, B. Rand, Large diameter carbon fibres from mesophase pitch, Carbon N. Y. 40 (2002) 2109–2116. https://doi.org/10.1016/S0008-6223(02)00060-X.

[89] T.H. Lim, S.Y. Yeo, Investigation of the degradation of pitch-based carbon fibers properties upon insufficient or excess thermal treatment, Sci. Rep. 7 (2017) 1–12. https://doi.org/10.1038/s41598-017-05192-5.

[90] T. Matsumoto, I. Mochida, A structural study on oxidative stabilization of mesophase pitch fibers derived from coaltar, Carbon N. Y. 30 (1992) 1041–1046. https://doi.org/10.1016/0008-6223(92)90134-I.

[91] H. Shimanoe, S. Ko, Y.-P.P. Jeon, K. Nakabayashi, J. Miyawaki, S.-H.H. Yoon, Shortening stabilization time using pressurized air flow in manufacturing mesophase pitch-based carbon fiber, Polymers (Basel). 11 (2019). https://doi.org/10.3390/polym11121911.

[92] Y. Peng, R. Tan, Y. Liu, J. Yang, Y. Li, J. Li, Z. Fan, K. Shi, Mesophase pitch-based carbon fibers: Accelerated stabilization of pitch fibers under effective plasma irradiation-assisted modification, Materials (Basel). 14 (2021). https://doi.org/10.3390/ma14216382.

[93] B.E. Barton, M.J. Behr, J.T. Patton, E.J. Hukkanen, B.G. Landes, W. Wang, N. Horstman, J.E. Rix, D. Keane, S. Weigand, M. Spalding, C. Derstine, High-modulus low-cost carbon fibers from polyethylene enabled by boron catalyzed graphitization, Small. 13 (2017) 1701926. https://doi.org/10.1002/smll.201701926.

[94] Z. Liu, S. Hanning, Y. Su, M. Bouhrara, T. Gries, Investigation of combined N2- and

KMnO4-pretreatment to reduce stabilization time of polyacrylonitrile-based carbon fibers, J. Appl. Polym. Sci. 140 (2023) 1–13. https://doi.org/10.1002/app.53515.

[95] I. Norberg, Y. Nordström, R. Drougge, G. Gellerstedt, E. Sjöholm, A new method for stabilizing softwood kraft lignin fibers for carbon fiber production, J. Appl. Polym. Sci. 128 (2013) 3824–3830. https://doi.org/10.1002/app.38588.

[96] Z. Xu, Y. Huang, C. Min, L. Chen, L. Chen, Effect of γ-ray radiation on the polyacrylonitrile based carbon fibers, Radiat. Phys. Chem. 79 (2010) 839–843. https://doi.org/10.1016/j.radphyschem.2010.03.002.

[97] A.R. Bunsell, A. Piant, A review of the development of three generations of small diameter silicon carbide fibres, J. Mater. Sci. 41 (2006) 823–839. https://doi.org/10.1007/s10853-006-6566-z.

[98] S.Y. Kim, S. Lee, S. Park, S.M. Jo, H.S. Lee, H.I. Joh, Continuous and rapid stabilization of polyacrylonitrile fiber bundles assisted by atmospheric pressure plasma for fabricating large-tow carbon fibers, Carbon N. Y. 94 (2015) 412–416. https://doi.org/10.1016/j.carbon.2015.07.012.

[99] S.W. Lee, H.Y. Lee, S.Y. Jang, S. Jo, H.S. Lee, W.H. Choe, S. Lee, Efficient preparation of carbon fibers using plasma assisted stabilization, Carbon N. Y. 55 (2013) 361–365. https://doi.org/10.1016/j.carbon.2012.10.062.

[100] S.Y.S.Y. Kim, S.Y.S.Y. Kim, S. Lee, S. Jo, Y.H. Im, H.S. Lee, Microwave plasma carbonization for the fabrication of polyacrylonitrile-based carbon fiber, Polymer (Guildf). 56 (2015) 590–595. https://doi.org/10.1016/j.polymer.2014.11.034.

[101] T. Bonds, Low cost, high volume, carbon fiber precursor for plasma oxidation, 2020.

[102] S. Park, H.S. Kil, D. Choi, S.K. Song, S. Lee, Rapid stabilization of polyacrylonitrile fibers achieved by plasma-assisted thermal treatment on electron-beam irradiated fibers, J. Ind. Eng. Chem. 69 (2019) 449–454. https://doi.org/10.1016/j.jiec.2018.10.008.

[103] L. Sun, M. Li, L. Shang, L. Xiao, Y. Liu, M. Zhang, Y. Ao, The influence of oxygen on skin-core structure of polyacrylonitrile-based precursor fibers, Polymer (Guildf). 197 (2020) 122516. https://doi.org/10.1016/j.polymer.2020.122516.

[104] S.B. Warner, L.H. Peebles, D.R. Uhlmann, Oxidative stabilization of acrylic fibres - Part 1: Oxygen uptake and general model, J. Mater. Sci. 14 (1979) 556–564. https://doi.org/10.1007/BF00772714.

[105] S.B. Warner, D.R. Uhlmann, L.H. Peebles, Oxidative stabilization of acrylic fibres - Part 3: Morphology of polyacrylonitrile, J. Mater. Sci. 14 (1979) 1893–1900. https://doi.org/10.1007/BF00551029.

[106] J. Wang, L. Hu, C. Yang, W. Zhao, Y. Lu, Effects of oxygen content in the atmosphere on thermal oxidative stabilization of polyacrylonitrile fibers, RSC Adv. 6 (2016) 73404–73411. https://doi.org/10.1039/c6ra15308a.

[107] E.A. Morris, R. Sarabia-Riquelme, N. Hochstrasser, J. Burgess, A.E. Oberlink, D.L. Eaton, M.C. Weisenberger, Early development of multifilament polyacrylonitrile-derived

structural hollow carbon fibers from a segmented arc spinneret, Carbon N. Y. 178 (2021) 223–232. https://doi.org/10.1016/j.carbon.2021.03.004.

[108] I. Mochida, S.M. Zeng, Y. Korai, H. Toshima, The introduction of a skin-core structure in mesophase pitch fibers by oxidative stabilization, Carbon N. Y. 28 (1990) 193–198. https://doi.org/10.1016/0008-6223(90)90113-D.

[109] C. Banerjee, V.K. Chandaliya, P.S. Dash, Recent advancement in coal tar pitch-based carbon fiber precursor development and fiber manufacturing process, J. Anal. Appl. Pyrolysis. 158 (2021) 105272. https://doi.org/10.1016/J.JAAP.2021.105272.

[110] I. Karacan, L. Erzurumluoğlu, The effect of carbonization temperature on the structure and properties of carbon fibers prepared from poly(m-phenylene isophthalamide) precursor, Fibers Polym. 16 (2015) 1629–1645. https://doi.org/10.1007/s12221-015-5030-6.

[111] J. Drbohlav, W.T.K. Stevenson, The oxidative stabilization and carbonization of a synthetic mesophase pitch, part II: The carbonization process, Carbon N. Y. 33 (1995) 713–731. https://doi.org/10.1016/0008-6223(95)00012-3.

[112] W. wei Li, H. liang Kang, J. Xu, R. gang Liu, Effects of ultra-high temperature treatment on the microstructure of carbon fibers, Chinese J. Polym. Sci. (English Ed. 35 (2017) 764–772. https://doi.org/10.1007/s10118-017-1922-9.

[113] X. Qin, Y. Lu, H. Xiao, Y. Wen, T. Yu, A comparison of the effect of graphitization on microstructures and properties of polyacrylonitrile and mesophase pitch-based carbon fibers, Carbon N. Y. 50 (2012) 4459–4469. https://doi.org/10.1016/j.carbon.2012.05.024.

[114] S.-S. Tzeng, Structure and Property Relationships in Carbon Fibers, Rensselaer Polytechnic Institute, 1992.

[115] D.J. Johnson, Strucutre-property relationships in carbon fibres, J. Phys. D. Appl. Phys. 20 (1987) 286–291.

[116] D.D. Edie, The effect of processing on the structure and properties of carbon fibers, Carbon N. Y. 36 (1998) 345–362. https://doi.org/10.1016/S0008-6223(97)00185-1.

[117] R.J. Diefendorf, E.W. Tokarsky, The relationship of structure to properties in graphite fibers, Part I, 1971.

[118] J. He, Q. Chen, B. Fan, M. Li, H. Zhu, H. Malik, H. Zhang, Y. Liu, J. Yu, Evolution of microstructure and property during industrial continuous heat treatment of polyacrylonitrile fibers up to 1900 °C, Polym. Degrad. Stab. 234 (2025) 1–8. https://doi.org/10.1016/j.polymdegradstab.2025.111258.

[119] R.Y. Ruan, L.W. Ye, H. Feng, L.H. Xu, Y. Wang, High temperature evolution of the microstructure in the radial direction of PAN-based carbon fibers and its relationship to mechanical properties, New Carbon Mater. 35 (2020) 295–306. https://doi.org/10.1016/S1872-5805(20)60491-7.

[120] S. Park, S.H. Lee, S.M. Lee, G. Lee, D.H. Jung, The effect of heteroatoms and temperature ramping rate on pyrolysis of coal tar pitch for high value of β-resin, Carbon Lett. 34 (2024) 2269–2278. https://doi.org/10.1007/s42823-024-00753-x.

[121] L. Chai, B. Lou, R. Yu, F. Wen, H. Yuan, Z. Li, Z. Zhang, J. Li, D. Liu, Study on structures and properties of isotropic pitches and carbon fibers from co-carbonization of aromatic-rich distillate oil and polyethylene glycol, J. Anal. Appl. Pyrolysis. 158 (2021) 105260. https://doi.org/10.1016/j.jaap.2021.105260.

[122] Y. Cheng, L. Yang, T. Luo, C. Fang, J. Su, J. Hui, Preparation and characterization of mesophase pitch via co-carbonization of waste polyethylene/petroleum pitch, J. Mater. Sci. Technol. 31 (2015) 857–863. https://doi.org/10.1016/j.jmst.2015.07.010.

[123] I. Mochida, S.H. Yoon, Y. Korai, Control of transversal texture in circular mesophase pitch-based carbon fibre using non-circular spinning nozzles, J. Mater. Sci. 28 (1993) 2331–2336. https://doi.org/10.1007/BF01151662.

[124] F. Panerai, T. Cochell, A. Martin, J.D. White, Experimental measurements of the high-temperature oxidation of carbon fibers, Int. J. Heat Mass Transf. 136 (2019) 972–986. https://doi.org/10.1016/j.ijheatmasstransfer.2019.03.018.

[125] S.-M. Zeng, Y. Korai, I. Mochida, T. Hino, H. Toshima, The creation of a skin-core structure in petroleum derived mesophase pitch based carbon fiber, Bull. Chem. Soc. Jpn. 63 (1990) 2083–2088. https://doi.org/10.1246/bcsj.63.2083.

[126] Polyethylene powder, low density, 500 micron, Thermo Scientific TM, 2022.

[127] Humboldt UNniversitat zu Berlin, Investigation of polymers with differential scanning calorimetry, 2009.

[128] Y.Y. Wang, G.P. Wu, R.M. Li, X.L. Li, C.X. Lu, Fracture mechanisms of polyacrylonitrile-based high-strength type carbon fibers, Fibers Polym. 15 (2014) 2541–2543. https://doi.org/10.1007/s12221-014-2541-5.

[129] J.B. Jones, J.B. Barr, R.E. Smith, Analysis of flaws in high-strength carbon fibres from mesophase pitch, J. Mater. Sci. 15 (1980) 2455–2465. https://doi.org/10.1007/BF00550747.

[130] H.G. Chae, B.A. Newcomb, P. V. Gulgunje, Y. Liu, K.K. Gupta, M.G. Kamath, K.M. Lyons, S. Ghoshal, C. Pramanik, L. Giannuzzi, K. Şahin, I. Chasiotis, S. Kumar, High strength and high modulus carbon fibers, Carbon N. Y. 93 (2015) 81–87. https://doi.org/10.1016/j.carbon.2015.05.016.

[131] X. Qian, X. Wang, J. Zhong, J. Zhi, F. Heng, Y. Zhang, S. Song, Effect of fiber microstructure studied by Raman spectroscopy upon the mechanical properties of carbon fibers, J. Raman Spectrosc. 50 (2019) 665–673. https://doi.org/10.1002/jrs.5569.

[132] G.A. Zickler, B. Smarsly, N. Gierlinger, H. Peterlik, O. Paris, A reconsideration of the relationship between the crystallite size La of carbons determined by X-ray diffraction and Raman spectroscopy, Carbon N. Y. 44 (2006) 3239–3246. https://doi.org/10.1016/j.carbon.2006.06.029.

[133] C.L. Angell, I.C. Lewis, Raman spectroscopy of mesophase pitches, Carbon N. Y. 16 (1978) 431–432. https://doi.org/10.1016/0008-6223(78)90088-X.

[134] G. Washer, F. Blum, Raman spectroscopy for the nondestructive testing of carbon fiber, Adv. Mater. Sci. Eng. 2008 (2008) 2–5. https://doi.org/10.1155/2008/693207.

[135] W. Ruland, B. Smarsly, X-ray scattering of non-graphitic carbon: An improved method of evaluation, J. Appl. Crystallogr. 35 (2002) 624–633. https://doi.org/10.1107/S0021889802011007.

[136] W.N. Reynolds, J.V. Sharp, Crystal shear limit to carbon fibre strength, Carbon N. Y. 12 (1974) 103–110. https://doi.org/10.1016/0008-6223(74)90018-9.

[137] Goodfellow, Datasheet for semi crystalline polyethylene terephthalate/PET powder 300 micron max, (n.d.). https://www.goodfellow.com/p/es30-pd-000132/semi-crystalline-polyethylene-terephthalate-pet-powder.

[138] Y. Kong, J.N. Hay, The measurement of the crystallinity of polymers by DSC, Polymer (Guildf). 43 (2002) 3873–3878. https://doi.org/10.1016/S0032-3861(02)00235-5.

[139] Z. Chen, J.N. Hay, M.J. Jenkins, FTIR spectroscopic analysis of poly(ethylene terephthalate) on crystallization, Eur. Polym. J. 48 (2012) 1586–1610. https://doi.org/10.1016/j.eurpolymj.2012.06.006.

[140] A. Scherschel, C. Love-Baker, A. Sushchenko, T. Harrell, K. Brown, X. Li, Compatibility of mesophase pitch and linear low-density polyethylene for low-cost carbon fiber, J. Polym. Res. 30 (2023) 82. https://doi.org/10.1007/s10965-023-03466-3.

[141] S. Venkatachalam, S.G. Nayak, J. V. Labde, P.R. Gharal, K. Rao, A.K. Kelkar, Chapter 4: Degradation and recyclability of poly (ethylene terephthalate), in: Polyester, 2012: pp. 75–98. https://doi.org/10.5772/48612.

[142] J.D. Kim, J.M. Yun, Y.S. Lim, M.S. Kim, Modification of coal-tar-pitch and carbon fiber properties by polymer additives, Korean J. Mater. Res. 26 (2016) 173–181. https://doi.org/10.3740/MRSK.2016.26.4.173.

[143] T.M. Harrell, A. Scherschel, C. Love-Baker, A. Tucker, J.D. Moskowitz, X. Li, Influence of oxygen uptake on pitch carbon fiber, Small. 2303527 (2023) 1–10. https://doi.org/10.1002/smll.202303527.

[144] F. Islam, S. Joannès, S. Bucknell, Y. Leray, A. Bunsell, L. Laiarinandrasana, Investigation of tensile strength and dimensional variation of T700 carbon fibres using an improved experimental setup, J. Reinf. Plast. Compos. 39 (2020) 144–162. https://doi.org/10.1177/0731684419873712.

[145] Y. Nordström, R. Joffe, E. Sjöholm, Mechanical characterization and application of Weibull statistics to the strength of softwood lignin-based carbon fibers, J. Appl. Polym. Sci. 130 (2013) 3689–3697. https://doi.org/10.1002/app.39627.

[146] W. Qing, L. Min, G. Yizhuo, W. Shaokai, Z. Zuoguang, Imaging the interphase of carbon fiber composites using transmission electron microscopy: Preparations by focused ion beam, ion beam etching, and ultramicrotomy, Chinese J. Aeronaut. 28 (2015) 1529–1538. https://doi.org/10.1016/j.cja.2015.05.005.

[147] Z. Li, L. Deng, I.A. Kinloch, R.J. Young, Raman spectroscopy of carbon materials and their composites: graphene, nanotubes and fibres, Prog. Mater. Sci. 135 (2023) 101089. https://doi.org/10.1016/j.pmatsci.2023.101089.

[148] F. Tuinstra, J.L. Koenig, Characterization of Graphite Fiber Surfaces with Raman Spectroscopy, J. Compos. Mater. 4 (1970) 492–499. https://doi.org/10.1177/002199837000400405.

[149] D.S. Knight, W.B. White, Characterization of Diamond Films by Raman Spectroscopy, J. Mater. Res. 4 (1989) 385–393. https://doi.org/10.1557/JMR.1989.0385.

[150] M. Endo, C. Kim, T. Karaki, T. Kasai, M.J. Matthews, S.D.M. Brown, M.S. Dresselhaus, T. Tamaki, Y. Nishimura, Structural characterization of milled mesophase pitch-based carbon fibers, Carbon N. Y. 36 (1998) 1633–1641. https://doi.org/10.1016/S0008-6223(98)00157-2.

[151] O.A. Maslova, M.R. Ammar, G. Guimbretière, J.N. Rouzaud, P. Simon, Determination of crystallite size in polished graphitized carbon by Raman spectroscopy, Phys. Rev. B - Condens. Matter Mater. Phys. 86 (2012). https://doi.org/10.1103/PhysRevB.86.134205.

[152] K.J. Putman, M.R. Rowles, N.A. Marks, C. De Tomas, J.W. Martin, I. Suarez-Martinez, Defining graphenic crystallites in disordered carbon: Moving beyond the platelet model, Carbon N. Y. 209 (2023). https://doi.org/10.1016/j.carbon.2023.03.040.

[153] R. Shokrani Havigh, H. Mahmoudi Chenari, A comprehensive study on the effect of carbonization temperature on the physical and chemical properties of carbon fibers, Sci. Rep. 12 (2022) 1–14. https://doi.org/10.1038/s41598-022-15085-x.

[154] H. Fujimoto, Theoretical X-ray scattering intensity of carbons with turbostratic stacking and AB stacking structures, Carbon N. Y. 41 (2003) 1585–1592. https://doi.org/10.1016/S0008-6223(03)00116-7.

[155] C.A. Love-baker, T.M. Harrell, F. Vautard, J. Klett, X. Li, Analysis of the turbostratic structures in PAN-based carbon fibers with wide-angle x-ray diffraction, Carbon N. Y. 224 (2024) 119037. https://doi.org/10.1016/j.carbon.2024.119037.

[156] Z.W. Wilchinsky, Recent developments in the measurement of orientation in polymers by X-ray diffraction, Adv. X-Ray Anal. 6 (1962) 231–241. https://doi.org/10.1154/s037603080000210x.

[157] A. Gupta, I.R. Harrison, J. Lahijani, Small-angle X-ray scattering in carbon fibers, J. Appl. Crystallogr. 27 (1994) 627–636. https://doi.org/10.1107/S002188989400227X.

[158] K. Fukuyama, Y. Kasahara, N. Kasahara, A. Oya, Small-angle X-ray scattering study of the pore structure of carbon fibers prepared from a polymer blend of phenolic resin and polystyrene, 39 (2001) 287–290. https://doi.org/10.1016/S0008-6223(00)00159-7.

[159] A.F. Thünemann, W. Ruland, Microvoids in polyacrylonitrile fibers: A small-angle X-ray scattering study, Macromolecules. 33 (2000) 1848–1852. https://doi.org/10.1021/ma991427x.

[160] P. Xiao, Y. Gong, D. Li, Z. Li, In-situ SAXS study on pore structure change of PAN-based carbon fiber during graphitization, Microporous Mesoporous Mater. 323 (2021). https://doi.org/10.1016/j.micromeso.2021.111201.

[161] A. Wlochowicz, S. Rabiej, Determination of micropore concentration and size distribution

in carbon fibres by the SAXS method, 190 (1991) 187–200. https://doi.org/10.1002/apmc.1991.051900113.

[162] H. Peterlik, P. Fratzl, K. Kromp, Pore structure of carbon/carbon composites studied by small-angle X-ray scattering, Carbon N. Y. 32 (1994) 939–945. https://doi.org/10.1016/0008-6223(94)90053-1.

[163] M. Kaburagi, Y. Bin, D. Zhu, C. Xu, M. Matsuo, Small angle X-ray scattering from voids within fibers during the stabilization and carbonization stages, Carbon N. Y. 41 (2003) 915–926. https://doi.org/10.1016/S0008-6223(02)00407-4.

[164] R. Harikrishnan, P.M.M.C.S. Upadhyay, Generalized Weibull model-based statistical tensile strength, Arch. Appl. Mech. 88 (2018) 1617–1636. https://doi.org/10.1007/s00419-018-1391-9.

[165] E.G. Stoner, D.D. Edie, S.D. Durham, An end-effect model for the single-filament tensile test, J. Mater. Sci. 29 (1994) 6561–6574. https://doi.org/10.1007/BF00354022.

[166] H. Okuda, R.J. Young, D. Wolverson, F. Tanaka, G. Yamamoto, T. Okabe, Investigating nanostructures in carbon fibres using Raman spectroscopy, Carbon N. Y. 130 (2018) 178–184. https://doi.org/10.1016/j.carbon.2017.12.108.

[167] M.S. Dresselhaus, A. Jorio, M. Hofmann, G. Dresselhaus, R. Saito, Perspectives on carbon nanotubes and graphene Raman spectroscopy, Nano Lett. 10 (2010) 751–758. https://doi.org/10.1021/nl904286r.

[168] L.G. Cançado, A. Jorio, E.H.M. Ferreira, F. Stavale, C.A. Achete, R.B. Capaz, M.V.O. Moutinho, A. Lombardo, T.S. Kulmala, A.C. Ferrari, Quantifying defects in graphene via Raman spectroscopy at different excitation energies, Nano Lett. 11 (2011) 3190–3196. https://doi.org/10.1021/nl201432g.

[169] T. Wu, C. Lu, T. Sun, Y. Li, Study on Raman multi-peak fitting and structure quantitative analysis of PAN-based carbon fibers, J. Mater. Sci. 57 (2022) 15385–15412. https://doi.org/10.1007/s10853-022-07589-8.

[170] D.B. Verbets, I.A. Bubnenkov, E.L. Dzidziguri, V.M. Samoilov, N.N. Stepareva, Sample preparation method for X-ray structure analysis of carbon fiber crystal structural parameters after various heat treatments, Fibre Chem. 52 (2020) 65–70. https://doi.org/10.1007/s10692-020-10153-2.

[171] S.H. Lee, D.S. Kang, S.M. Lee, J.S. Roh, X-ray diffraction analysis of the effect of ball milling time on crystallinity of milled polyacrylonitrile-based carbon fiber, Carbon Lett. 26 (2018) 11–17. https://doi.org/10.5714/CL.2018.26.011.

[172] D. Li, C. Lu, S. Du, G. Wu, Y. Yang, Structural features of various kinds of carbon fibers as determined by small-angle X-ray scattering, (2016). https://doi.org/10.1007/s00339-016-0487-8.

[173] M.W. Brooks, S. Lynn, Recovery of calcium carbonate and hydrogen sulfide from waste calcium sulfide, Ind. Eng. Chem. Res. 36 (1997) 4236–4242. https://doi.org/10.1021/ie970151j.

[174] P.S. Kubiak, A.L. Johnson, P.J. Cameron, G. Kociok-Köhn, Single source precursors for calcium sulfide (CaS) deposition, Eur. J. Inorg. Chem. (2019) 3962–3969. https://doi.org/10.1002/ejic.201900550.

[175] K.R. Brown, C. Love-Baker, T.M. Harrell, X. Li, Effect of tension during sulfonation stabilization for UHMWPE-derived carbon fibers, J. Polym. Res. 2023 3012. 30 (2023) 1–14. https://doi.org/10.1007/S10965-023-03829-W.

[176] X. Zhou, A. Belianinov, A.K. Naskar, Analyzing carbon fiber structures observed by helium ion microscopy and their mechanical properties, Carbon Trends. 4 (2021) 100055. https://doi.org/10.1016/j.cartre.2021.100055.

[177] M.L. Wang, W.F. Bian, The relationship between the mechanical properties and microstructures of carbon fibers, New Carbon Mater. 35 (2020) 42–49. https://doi.org/10.1016/S1872-5805(20)60474-7.

[178] I. Mochida, S.M. Zeng, Y. Korai, T. Hino, H. Toshima, The introduction of a skin-core structure in mesophase pitch fibers through a successive stabilization by oxidation and solvent extraction, Carbon N. Y. 29 (1991) 23–29. https://doi.org/10.1016/0008-6223(91)90090-6.

[179] N. Iwashita, C.R. Park, H. Fujimoto, M. Shiraishi, M. Inagaki, Specification for a standard procedure of X-ray diffraction measurements on carbon materials, Carbon N. Y. 42 (2004) 701–714. https://doi.org/10.1016/j.carbon.2004.02.008.

[180] Z. Yue, C. Liu, A. Vakili, Solvated mesophase pitch-based carbon fibers: thermal-oxidative stabilization of the spun fiber, J. Mater. Sci. 52 (2017) 8176–8187. https://doi.org/10.1007/s10853-017-1024-7.

[181] I. Mochida, S.M. Zeng, Y. Korai, T. Hino, H. Toshima, Structure and properties of mesophase pitch carbon fibre with a skin-core structure carbonized under strain, J. Mater. Sci. 27 (1992) 1960–1968. https://doi.org/10.1007/BF01107225.

[182] A. Eckmann, A. Felten, A. Mishchenko, L. Britnell, R. Krupke, K.S. Novoselov, C. Casiraghi, Probing the nature of defects in graphene by Raman spectroscopy, Nano Lett. 12 (2012) 3925–3930. https://doi.org/10.1021/nl300901a.

[183] Y. Sha, W. Liu, Y. Li, W. Cao, Formation mechanism of skin-core chemical structure within stabilized polyacrylonitrile monofilaments, Nanoscale Res. Lett. 14 (2019). https://doi.org/10.1186/s11671-019-2926-x.

[184] S. Nunna, M. Setty, Formation of skin-core in carbon fibre processing: A defect or an effect?, EXPRESS Polym. Lett. 13 (2019) 146–158. https://doi.org/10.3144/expresspolymlett.2019.14.

[185] F. Ruiz-Perez, S.M. López-Estrada, R. V. Tolentino-Hernández, F. Caballero-Briones, Carbon-based radar absorbing materials: A critical review, J. Sci. Adv. Mater. Devices. 7 (2022). https://doi.org/10.1016/j.jsamd.2022.100454.

[186] F.G. Emmerich, Young's modulus, thermal conductivity, electrical resistivity and coefficient of thermal expansion of mesophase pitch-based carbon fibers, Carbon N. Y. 79 (2014) 274–293. https://doi.org/10.1016/j.carbon.2014.07.068.

[187] C. Li, G. Xian, Influence of elevated temperature treatment on the microstructures and mechanical properties of carbon fibers in argon environment, J. Mater. Eng. Perform. 28 (2019) 7804–7815. https://doi.org/10.1007/S11665-019-04480-7/METRICS.

[188] C. Gutiérrez, J.F. Rodríguez, I. Gracia, A. de Lucas, M.T. García, Reduction of the carbon footprint through polystyrene recycling: Economical evaluation, Process Saf. Environ. Prot. 101 (2016) 144–151. https://doi.org/10.1016/j.psep.2015.12.004.

[189] K. Siangchaew, M. Libera, The influence of fast secondary electrons on the aromatic structure of polystyrene, Philos. Mag. A Phys. Condens. Matter, Struct. Defects Mech. Prop. 80 (2000) 1001–1016. https://doi.org/10.1080/01418610008212095.

[190] S. Otani, A. Oya, Progress of pitch-based carbon fiber in Japan, in: ACS Symp. Ser., ACS, 1986: pp. 323–334. https://doi.org/10.1021/bk-1986-0303.ch022.

[191] S.H. Hong, Y. Korai, I. Mochida, Mesoscopic texture at the skin area of mesophase pitch-based carbon fiber, Carbon N. Y. 38 (2000) 805–815. https://doi.org/10.1016/S0008-6223(99)00175-X.

[192] J.I. Hayashi, M. Nakashima, K. Kusakabe, S. Morooka, S. Mitsuda, Rapid stabilization of pitch fiber precursor by multi-step thermal oxidation, Carbon N. Y. 33 (1995) 1567–1571. https://doi.org/10.1016/0008-6223(95)00118-W.

[193] Y. Liu, Y. Liu, L. Shang, Y. Ao, Study on the structural evolution of polyacrylonitrile fibers in stepwise heat treatment process and its relationship with properties, J. Appl. Polym. Sci. 139 (2021).

[194] D.D. Edie, M.G. Dunham, Melt spinning pitch-based carbon fibers, Carbon N. Y. 27 (1989) 647–655. https://doi.org/10.1016/0008-6223(89)90198-X.